

Oil Dispersant System for Fixed Wing Aerial Platform

by

© Nathan Brazil

A Thesis submitted to the

School of Graduate Studies

in partial fulfillment of the requirements for the degree of

Master of Engineering, Mechanical

Faculty of Engineering

Memorial University of Newfoundland

January 2015

St. John's

Newfoundland

ABSTRACT

The global energy demand has led to increased oil production across the world, leading to an increase in the number of offshore oil platforms and oil tanker traffic. Further, this demand has pushed the industry to develop in increasingly remote areas and harsh environments. Newfoundland, which operates the largest offshore oil platform in the world, has a strong safety record, but limited disaster response capabilities. The Newfoundland ecosystem is particularly sensitive to the effects of an oil spill, with its diverse marine life, rugged coastline, and harsh climate. Further, these harsh conditions reduce the effectiveness of standard containment and recovery options for oil spills used elsewhere. The author seeks to address the issue by designing a deployable oil dispersant system for fixed wing aircraft. Oil dispersants sprayed onto the surface of an oil slick remain one of the most effective methods for mitigating the effects of an oil spill. The primary focus of this thesis is the preliminary engineering design of the system, which includes the use of theoretical and computational stress analysis techniques, aerodynamics, and rigid body dynamics considering the motion of the system. The thesis concludes with the preliminary system design of a deployable oil dispersant system that is adaptable to multiple aircraft platforms.

ACKNOWLEDGEMENTS

The author gratefully acknowledges Research & Development Corporation (RDC) in Newfoundland for its funding support of this project. The guidance and support provided by Provincial Aerospace throughout the project is also gratefully appreciated. The technical guidance of Jake Trainor, Rob Northcote, and Cory Russell from Provincial Aerospace regarding practical aspects of this research was instrumental and is much appreciated. The author would also like to acknowledge Dr. Geoff Rideout for his guidance regarding system dynamics. His continuous advice and helpful discussions during the dynamic model development was a key to its success. Finally, the author would like to acknowledge both of his supervisors, Dr. Shawn Kenny and Dr. Samer Nakhla for their continued guidance, technical support, and overall for being excellent teachers and mentors. Appreciation for their constant support through every aspect of this project cannot be understated.

Table of Contents

Oil Dispersant System for Fixed Wing Aerial Platform.....	1
1. Introduction.....	1
1.1. Industry Overview	2
1.2. Oil Dispersants	3
2. Literature Review	10
2.1. Oil Dispersal Systems	11
2.1.1. Patents	11
2.1.2. Existing Designs	17
2.2. Simplified Models	21
2.2.1. Aerodynamic Loads	22
2.2.2. Structural Characteristics	23
2.3. Detailed Design	25
2.3.1. Optimization	25
2.3.2. Computational Aerodynamic Analysis	31
2.3.3. Aeroelastic Analysis	32
2.3.4. Dynamics	35
2.4. Conclusion.....	35
3. Preliminary Design	37
3.1. Conceptual Design	37
3.2. Parameter Identification	43
3.3. Design Geometry.....	48
3.4. Stress Analysis	52
3.5. Wind Loads	72
3.6. Material Selection	75
3.7. Conclusion.....	83
4. Detailed Static Analysis.....	85
4.1. Wind Loads	85

4.2.	Advanced Static Analysis.....	96
4.3.	Conclusion.....	113
5.	Dynamics	114
5.1.	Dynamics System Description	115
5.2.	20-Sim	117
5.3.	Simplified Model.....	120
5.4.	Realistic Simulation	126
5.4.1.	Bond Graph.....	127
5.4.2.	20-Sim Model	145
5.4.3.	System Analysis.....	147
5.5.	Conclusion.....	154
6.	Conclusions	155
6.1.	Preliminary Design Overview	155
6.2.	Overview of Detailed Analysis	158
6.3.	Future Work	160
6.4.	Concluding Remarks	161
	References.....	162
	Appendix.....	167

List of Tables

Table 3-1 - Parameters and Influencing Factors	46
Table 3-2 - Material Properties	77
Table 3-3 - Analysis Results – Material Selection.....	80
Table 3-4 - Preliminary Design Summary	83
Table 4-1 - Computational Fluid Dynamics Properties	87
Table 5-1 - Bond Graph Equivalencies.....	128
Table 5-2 - CNC Machine Parameters.....	142
Table 5-3 - Bond Graph Parameters	145
Table 6-1 - Defined System Parameters	157

List of Figures

Figure 1-1 - Dispersant Timeline	4
Figure 1-2 - Dispersant Application from Smaller Vessel.....	6
Figure 1-3 - Spray System for Bell 212 Helicopter	7
Figure 1-4 - Aerial Oil Dispersant Spraying.....	7
Figure 2-1 - Spray Boom Cross-section.....	12
Figure 2-2 - Spray Boom Attached to Wing.....	13
Figure 2-3 - Spray Boom Airfoil Shape.....	14
Figure 2-4 - Edge Flap Nozzle Design.....	15
Figure 2-5 - Deployable Spray Boom.....	16
Figure 2-6 - Aerial Dispersion System	16
Figure 2-7 - Jettisonable Helicopter Spray Boom	17
Figure 2-8 - C-130 Spray Boom Truss Design	18
Figure 2-9 - C-130 Retractable Spray Boom (ADDS System).....	19
Figure 2-10 - DC-4 with Wing Mounted Spray Boom.....	20
Figure 2-11 - Airfoil Shape Spray Boom.....	21
Figure 2-12 - Dornier 728-100 Optimized Door Support Arm.....	26
Figure 2-13 - Structural Optimization Problems	27
Figure 2-14 - Topology Optimization with Complex Boundary Conditions.....	29
Figure 2-15 - Evolutionary Design Process	30
Figure 2-16 - Airflow around a Truss	31

Figure 2-17 - I-STARs Multidisciplinary Analysis System.....	33
Figure 2-18 - Multidisciplinary Analysis - Fluid Structure Interaction	34
Figure 3-1 - C-130 Side Retractable Boom	40
Figure 3-2 – Internal Retractable Boom	40
Figure 3-3 - Dash 8 - Pressurized Cabin.....	41
Figure 3-4 - Fully Stowed and Fully Deployed Oil Dispersant System	42
Figure 3-5 - Deployable Oil Dispersant System Components.....	44
Figure 3-6 - Parameter Identification.....	47
Figure 3-7 - Dash 8 Mounting Locations.....	50
Figure 3-8 - Right Angle of Fully Deployed Boom.....	51
Figure 3-9 - Wind Load on Main Boom	53
Figure 3-10 - Wind Load - Distributed Load.....	54
Figure 3-11 – Maximum Stress Conditions Resulting from Inertial Loads.....	57
Figure 3-12 - Vertical Loading Scenario - Lumped Mass of Actuating Truss	59
Figure 3-13 - Main Boom under Inertial Loading	60
Figure 3-14 - Unit Force Method - Remove Redundant Force.....	62
Figure 3-15 - Unit Force Method – Deflection due to Unit Force.....	64
Figure 3-16 - Simplified Inertia Loading with Corresponding Shear and Moment Diagrams	69
Figure 3-17 - Maximum Stress Conditions Resulting from Wind Load.....	70
Figure 3-18 - Representation of Critical Stress Points.....	72
Figure 3-19 - Drag Coefficient of a Cylinder	73

Figure 3-20 - Parametric Design Process.....	79
Figure 4-1 - CFD Simulation - 16 Elements.....	87
Figure 4-2 - Pressure Map Across Main Boom due to Wind Load	88
Figure 4-3 - Node Selection for Pressure Output Data	90
Figure 4-4 - CFD Simulation - 8 Elements.....	91
Figure 4-5 – CFD Simulation - 32-Elements	92
Figure 4-6 - CFD Simulation - 64 elements.....	93
Figure 4-7 - Mesh Density Study.....	93
Figure 4-8 - CFD Simulation, Angled Flow - 16 Elements.....	94
Figure 4-9 - CFD Simulation, Angled Flow - 32 Elements.....	95
Figure 4-10 - Basic Wireframe Model with Force Fa	98
Figure 4-11 – Basic Wireframe Simulation Result – Stress Contour.....	98
Figure 4-12 - Basic Wireframe Model Including Vertical Truss.....	99
Figure 4-13 - Wireframe with Vertical Support - Stress Contour.....	100
Figure 4-14 - Wireframe Model with Aerodynamic Load - Stress Contour.....	101
Figure 4-15 - Full Wireframe Model of Oil Dispersant System.....	102
Figure 4-16 - Full Wireframe Model - Stress Contour	103
Figure 4-17 - Main Boom Shell Model Mesh.....	104
Figure 4-18 - Local Buckling of the Main Boom at Vertical Support Truss - Unscaled.....	105
Figure 4-19 - Unscaled Deformation of Boom	106
Figure 4-20 - Scaled to Show Deformation	106
Figure 4-21 - Vertical Support Truss Force on Main Boom.....	107

Figure 4-22 - Distributed Wind Load Applied to Shell Model.....	109
Figure 4-23 - Wind Load Applied to Main Boom, Stress Contour	109
Figure 4-24 - Unscaled Deformation - Full Loading Scenario	110
Figure 4-25 - Spray Nozzle Holes.....	111
Figure 4-26 - Dispersant Boom with Large Nozzle Holes.....	112
Figure 5-1 - Fully Stowed Position.....	115
Figure 5-2 - Fully Deployed Position	115
Figure 5-3 - System Loading Description.....	116
Figure 5-4 - 20-Sim Graphical Interface.....	118
Figure 5-5 - 3D Mechanics Toolbox.....	119
Figure 5-6 - 3D Mechanics CAD Model	120
Figure 5-7 - 3D CAD Model in 20-Sim Graphical Interface	121
Figure 5-8 - Opposite Angles.....	122
Figure 5-9 - Aerodynamic Force Input	123
Figure 5-10 - Control Loop with Boom Model.....	124
Figure 5-11 – Lead screw Benchmark Analysis	125
Figure 5-12 - Force on Actuator due to Aerodynamic Load.....	126
Figure 5-13 - Resistance Element	129
Figure 5-14 - Inertia Element.....	130
Figure 5-15 - Capacitance Element.....	131
Figure 5-16 - Effort Source and Flow Source Elements.....	131
Figure 5-17 - Transformer Lever Analogy	132

Figure 5-18 - Transformer Element	132
Figure 5-19 - Gyration Element.....	133
Figure 5-20 - Springs in Series	134
Figure 5-21 - Springs in Parallel.....	135
Figure 5-22 - Circuit Diagram	136
Figure 5-23 - Developing the Bond Graph	136
Figure 5-24 - Bond Graph Solution of Circuit Diagram.....	137
Figure 5-26 - Basic DC Motor Circuit.....	138
Figure 5-25 - DC Motor Example.....	138
Figure 5-27 - DC Motor Spinning a Shaft	139
Figure 5-28 - A Typical Lead Screw	140
Figure 5-30 - CNC Machine Bond Graph Model	141
Figure 5-29 - CNC Machine Subcomponents.....	141
Figure 5-31 - Bond Graph Model of Lead Screw	143
Figure 5-32 - Bond Graph Model with Parasitic Element	146
Figure 5-33 – Deployable Oil Dispersant Dynamics Model.....	147
Figure 5-34 - Force Overshoot.....	148
Figure 5-35 - Effects of Changing Motor Parameters	149
Figure 5-36 - Dynamic Joint Forces	150
Figure 5-37 - System Voltage Input.....	151
Figure 5-38 - System Current Draw.....	152
Figure 5-39 - Decreasing the Current Draw	153

Figure 6-1 - Preliminary Design Summary.....156

List of Symbols, Nomenclature or Abbreviations

d_o – Main Boom Outer Diameter

d_i – Main Boom Inner Diameter

t – Main Boom Thickness

m_1 – Mass of Boom

m_2 – Mass of Support

E – Elastic Modulus of Main Boom

I – 2nd Moment of Area of Main Boom

A_a – Vertical Truss Cross-section Area

E_a – Elastic Modulus of Vertical Truss

θ – Angle between Boom and Fuselage

β – Angle between Boom and Vertical Support Truss

L_1 – Length of Main Boom

L_2 – Length of Actuating Truss

L_c – Distance from Base of Boom to Vertical Truss Connection

D_T – Diameter of Vertical Truss

F_s – Actuating Truss Reaction Force

F_a – Actuating Truss Reaction Force

R_e – Reynolds Number

ρ_a – Air Density

U – Air Speed

μ – Dynamic Viscosity

Q – Volumetric Flow Rate

q – Aerodynamic Line Load

C_d – Coefficient of Drag

F_d – Drag Force

ν – Kinematic Viscosity

A_f – Frontal Area of Main Boom

σ_{yield} – Yield Stress

σ_{allow} – Allowable Stress

ρ – Material Density

P_{avg} – Average Pressure on Main Boom

L_{arc} – Arc Length of Pressure Segment

1. Introduction

Global demand for energy continues to grow, driving the offshore oil industry to source oil from increasingly remote and harsh environments. This increasing demand has led to rapid growth in the industry, which has seen an increase in the number of offshore oil rigs and greater oil tanker traffic. As the industry eyes the vast arctic reserves of oil, it is vital that the risk of an oil spill at sea is considered, and the proper equipment is available to handle such a disaster. Recent events, such as the Deep Water Horizon in 2010 sit heavily on the conscious of the public [1]. Meanwhile the industry capability still remains at a minimum in many vital areas, with long response times. Globally, oil spill response has been handled in several ways with varying levels of success. The Newfoundland oil industry has emergency response plans that include the participation of several agencies such as the West Coast Marine Response Corporation (WCMRC), Eastern Canada Response Corporation (ECRC), and the Canadian Coast Guard [2]. However, the response capacity is limited in Newfoundland, and on a national level. There is demand in the local industry and in the global industry for new and improved methods of mitigating the effects of oil spills. It is the focus and intention of this thesis to address potential options in terms of providing the design of a novel oil dispersant system. To this end, a comprehensive design approach is developed using an array of simple and complex engineering techniques.

1.1. Industry Overview

There is much local demand for improvements to oil spill response capabilities. There are currently three major offshore oil and gas production operations in Newfoundland. The Hibernia oil platform, Terra Nova Floating Production Storage and Offloading vessel (FPSO), and White Rose FPSO all operate in the Grand Banks of Newfoundland. The Hibernia, a gravity base structure, is currently the largest offshore oil platform in the world. Another major gravity base structure is in development, named the Hebron, and is expected to begin oil production in 2017.

The current oil spill prevention regulations for the Newfoundland offshore industry are world class, with much of its regulatory body modelled after the successful Norwegian petroleum safety authority. The industry is heavily regulated, ensuring that environmental and work safety remains a top priority. The safety record of the local oil and gas industry remains one of the best in the world. However, the oil and gas industry in Newfoundland faces one of the most challenging environments, characterized by frequently intense sea states, consistently high winds, and sea ice. In the case of an oil spill, the response can be very complicated, or even impossible, due to weather challenges. These unique conditions demand a specialized, effective and fast response.

The Environmental Oil Spill Risk Assessment issued in 2007 outlines the probability and impact of an oil spill off the coast of Newfoundland [3]. Considerable risk comes from oil tankers and other ships passing through the Cabot Strait. The current Transport Canada

response time standard is 82 hours, which is approximately double the Norwegian response time.

Currently, there are several methods used in oil spill response. The primary methods used are mechanical recovery, spraying of chemical dispersants, and in-situ burning. Mechanical recovery methods include the use of floating booms or barriers, absorbing materials and skimming. Mechanical recovery methods are carried out using smaller ships, and are an effective method for dealing with smaller oil spills. In-situ burning is simply the burning of the surface oil slick, making use of fire resistant booms to contain and concentrate the oil. The Review of Offshore Oil-spill Prevention and Remediation Requirements and Practices in Newfoundland and Labrador in 2010 examined the effect of the local harsh environment conditions, and the unique difficulties that arise when considering a response to a major oil spill [2]. It was determined that the weather conditions present off the coast of Newfoundland would severely limit mechanical recovery of an oil spill, with the fraction of time that a mechanical recovery operation could be carried out being as low as 10% in the winter. The use of dispersants is not as dependant on ideal weather conditions, hence it was the recommended method for future use.

1.2. Oil Dispersants

The use of chemicals such as dispersants is one of the most effective methods to date for mitigating the effects of an oil spill. Oil dispersants such as COREXIT have been used extensively in disasters such as the Deep Water Horizon oil spill in 2010 [1].

Oil dispersants are sprayed on top of the oil slick, and work by reducing the surface tension that prevents the oil from mixing with the water. The surface oil slick begins to break down into smaller droplets, which are then mixed into the water column by wave action. The droplets of oil sinking into the water column allows for better mixing, and provides a greater surface area exposing it to more bacteria, which act to biodegrade the oil [4]. Figure 1-1 shows the timeline of an oil slick following the application of oil dispersant.

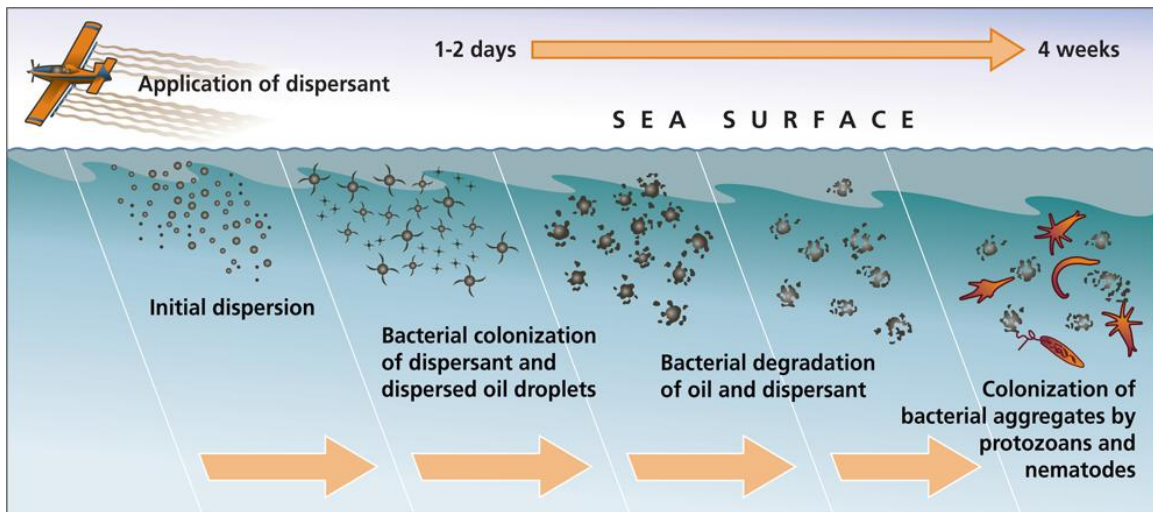


Figure 1-1 - Dispersant Timeline [5]

The primary advantage of oil dispersants is preventing the spread of the surface oil slick, which moves significantly faster than an oil water mixture. Also, the added exposure to bacteria in the water column leads to a more rapid biodegrading of the oil. In a location such as Newfoundland, it is vital that the oil slick does not reach the shoreline, which would be uniquely difficult to access for cleaning. Also, the oil platforms vicinity to the

Gulf Stream current creates a heightened risk as the spread would be more rapid once it entered the fast moving current.

Many methods exist to deploy the oil dispersant chemical, each varying in cost, response time, and overall spray area. The three primary methods of oil dispersant deployment are ships, helicopters, and fixed wing aircraft. Each method has its merits, and can be compared using performance variables such as payload capacity, transit speed, manoeuvrability, cost, and range [6].

Ships carry the largest payload ranging from 20 to 100 tonnes of dispersant, meaning that the ship can remain at the site of the spill for a long period. It is a relatively inexpensive option compared with the fixed-wing and helicopter options. It is limited by its speed, where transit times may take well over a day depending on how remote the oil spill is and how far the port of operations is based. It also must reduce speeds during spraying, meaning that the overall response time and area covered are significant limitations on the ship option.



Figure 1-2 - Dispersant Application from Smaller Vessel [7]

The helicopter option is perhaps the most limited option. It can only carry a small payload, usually around 1 tonne. It must refuel frequently, so a heliport must be nearby. It is relatively slow, and is more expensive. The major advantage to a helicopter is its manoeuvrability, which is ideal for small patchy oil spills.



Figure 1-3 - Spray System for Bell 212 Helicopter [8]

The fixed-wing aircraft option has the fastest response, longest range, and can cover the largest area in the shortest time. Much of the time in the air is spent maneuvering as the aircraft must turn back and realign itself downwind from the spill after every pass.



Figure 1-4 - Aerial Oil Dispersant Spraying [9]

Current capabilities within the province to tackle a major oil spill lie with WCMRC, ECRC, and the Canadian Coast Guard. All of these agencies rely on the use of smaller ships for the deployment of oil containing booms, near shore protection, and shoreline cleaning equipment. Deployment times vary based on oil spill size, ranging from 6 hours

for an oil spill of 150 tonnes, to 72 hours for an oil spill of 10,000 tonnes. The offshore oil-spill review ends with several recommendations relating to studying and implementing the use of oil dispersants.

A solution brought forward by this work is the potential of using a fixed-wing aircraft for the purpose of deploying the oil dispersant. The Oil Spill Response Joint Industry Project outlines the future industry needs in the area of aerial dispersant application [10]. It is claimed that the current C-130 platforms commonly used with the Aerial Dispersant Delivery System (ADDS) are becoming outdated, and will soon need to be replaced with a new design. This highlights the need for new ideas and new options within the industry, laying the foundation for the focus of this thesis.

The scope of the present study includes a literature review on relevant designs and patents, the preliminary engineering design synthesis of an oil dispersant system, and the subsequent use of theoretical and computational engineering methods to determine the design parameters of the system. The objectives of this research are to design an oil dispersant system for fixed wing aircraft that is more efficient than existing designs, as well as present a theoretical and computational design process. Chapter 2 considers existing designs, and research related to the industry. Chapter 3 presents the preliminary design and analytical analysis. Chapter 4 seeks to validate and improve the accuracy of the analytical analysis through the use of advanced engineering techniques such as Computational Fluid Dynamics and Finite Element Analysis. Chapter 5 considers the

linear actuator driven motion of the system, and employs the bond graph technique for the realistic dynamic simulation of the system.

2. Literature Review

The aircraft industry faces some of the most difficult challenges in engineering, as new aircraft designs push the limits of engineering and manufacturing capabilities. As the commercial aerospace industry continues to grow, there is an ever increasing demand for faster, safer, and cheaper aircraft design. This has led to intense research in many areas relating to aircraft design, including aerodynamics, structural design, noise emissions, propulsion, flight control, manufacturing and maintenance techniques, and cost engineering [11]. Current research reflects this multi-discipline nature of the aerospace industry.

The primary focus of research today is in computational analysis, dynamic simulation and materials modeling. There is an ongoing effort to reduce model uncertainty, and improve simulation fidelity through creating new simulation methods and refining existing ones. As computer technology rapidly improves, computationally intensive tools such as finite element analysis (FEA) and computational fluid dynamics (CFD) have become more accessible to smaller design companies. No longer are CFD and FEA tools reserved for conceptual design in multi-million dollar projects from Boeing and Airbus. Complex design problems can now be modeled with much higher accuracy and speed, improving safety, and optimizing the design in terms of weight and cost.

This literature review provides the design scope of a fixed wing oil dispersant platform. An overview of existing oil dispersal system designs will provide a basis for understanding of existing or currently available designs. Following this, analytical

approaches for various aspects, such as aerodynamic loads, simplified structural analysis, and other methods of analysis will be investigated. Finally, the theoretical approach for this type of structural design is covered, reviewing the current state of research in areas such as computational fluid dynamics, aero-structural analysis, and design optimization.

2.1. Oil Dispersal Systems

A key step in the engineering design process involves looking at existing designs on similar platforms, and how the design problem was approached by others. This approach often provides a solution, and can provide initial guidance for a new design. The chemical spray boom has been used on many different vehicles, from helicopters to hand-operated carts. Consisting of a pipe, spray nozzles, reservoir for spray substance, and often additional structure and avionics, the design of spray booms vary greatly, even for an individual vehicle type.

From these existing designs, several advantages can be gained from studying them. Various locations on the aircraft have different advantages and disadvantages. Component sizing and studies on drag effects of different configurations can give an initial starting point for the design. Methodology identification can be gained from how others solved complex structural and aerodynamic problems.

2.1.1. Patents

First, a review of relevant patents will give a glimpse into existing designs. Patent [12] presents a wing-mounted spray boom apparatus and its components. It provides a unique

way of adjusting the spray boom in midflight, for ideal spray coverage. It is attached to the trailing edge of the aircraft wing, with many nozzles spaced along the boom. The pipe is surrounded by an elongated housing to reduce drag and vortex shedding. The chemical is supplied from a reservoir within the aircraft. The advantage of this method is the minimized drag, and spray control. The disadvantage is the added complexity of a fairing, which is more vulnerable to dynamic instabilities due to aerodynamic forces as compared to a simple pipe.

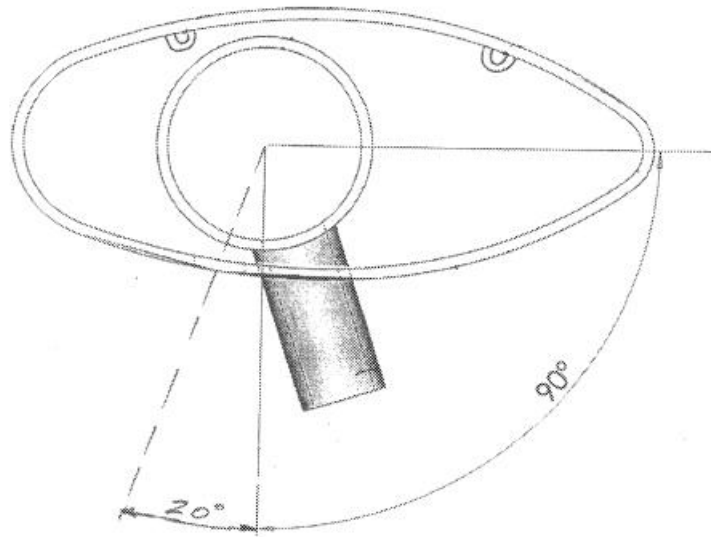


Figure 2-1 - Spray Boom Cross-section [12]

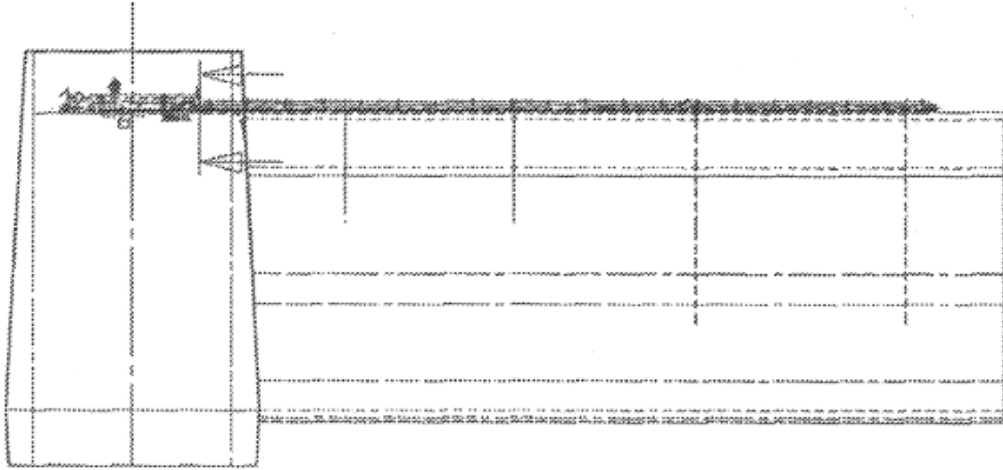


Figure 2-2 - Spray Boom Attached to Wing [12]

Patent [13] introduces the design of dispersant systems that assists in the generation of lift for the aircraft. The spray boom has the shape of an airfoil, with external holes for spraying the liquid. The dispersant method of a series of holes on the trailing edge is unique, but there are likely complications from adding a second lifting surface. This cambered airfoil shape would likely create a significant amount of drag, and would change the response behaviour of the aircraft during flight.

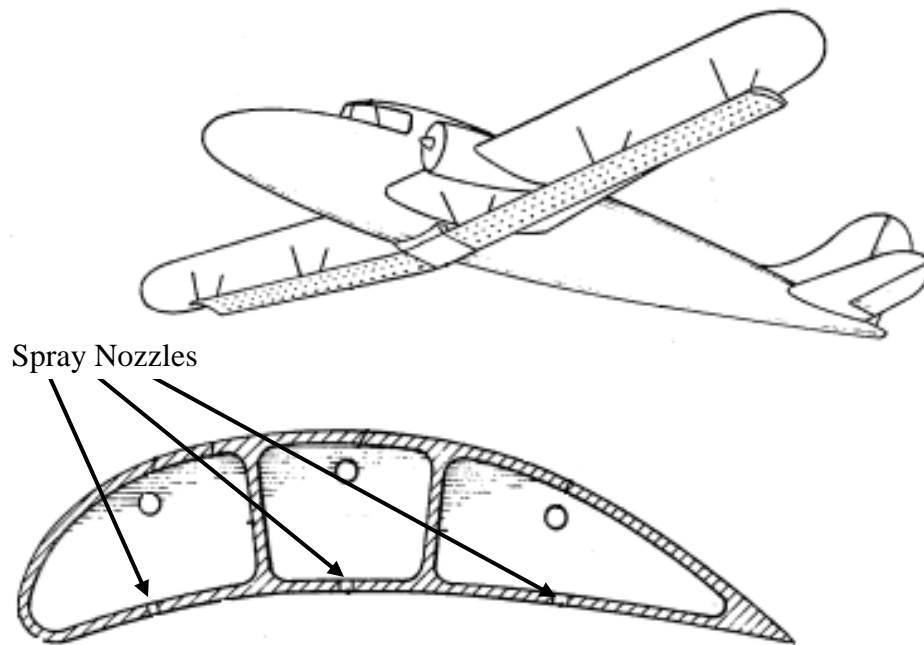


Figure 2-3 - Spray Boom Airfoil Shape [13]

Patent [14] has a set of nozzles at the base of a series of flaps. The flap segments deflect in opposite directions such that turbulent flow creates ideal spray conditions. The unique aspect of this design is that it specifically makes use of turbulence created to spread the dispersant. It also raises the idea that the entire system can be embedded within the aircraft wing.

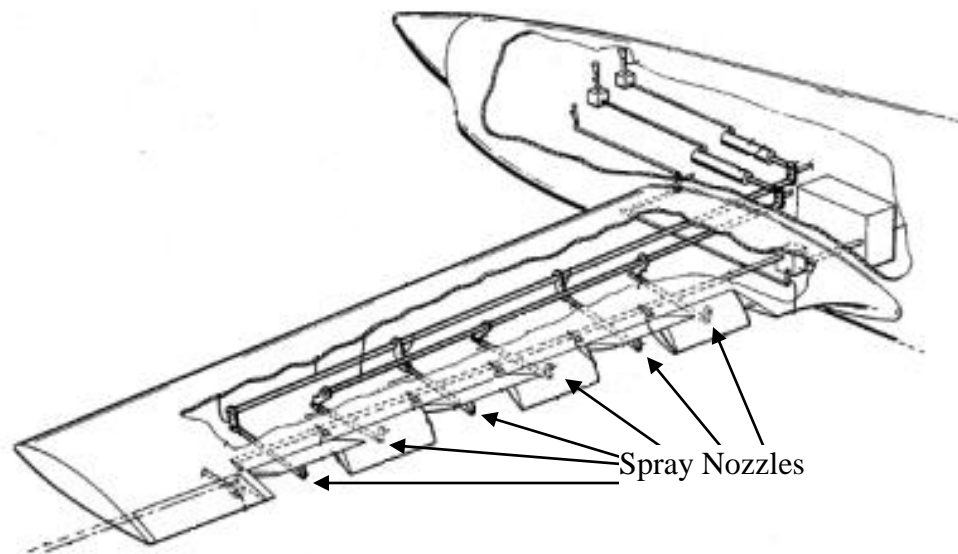


Figure 2-4 - Edge Flap Nozzle Design [14]

Patent [15] has a unique self-contained spray boom design that can deploy during flight. It is designed for aircraft that have aft cargo doors. The concept of a deployable system may still be useful for aircraft with no aft cargo door. The idea of a mechanism to deploy and stow the system is to reduce drag, but also to prevent damage to the system. This method increases safety during landing and take-off, as there will not be interference from the mechanism.

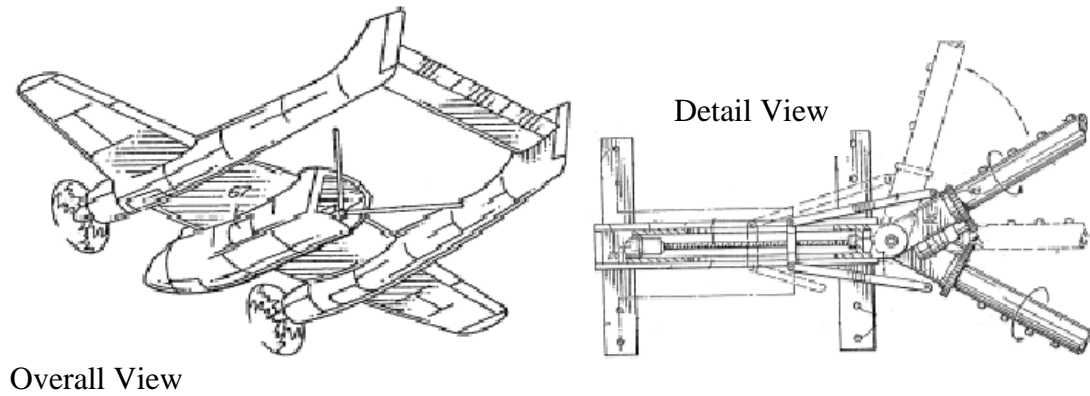


Figure 2-5 - Deployable Spray Boom [15]

Patent [16] shows an aircraft with no rear cargo door, but has a deployable dispersant system. It is designed in modular components, ideal for aircraft with cargo loading and unloading systems. The design focuses mainly on the internal modular aspect, but is designed to spray from a boom extending from the aircraft cabin.

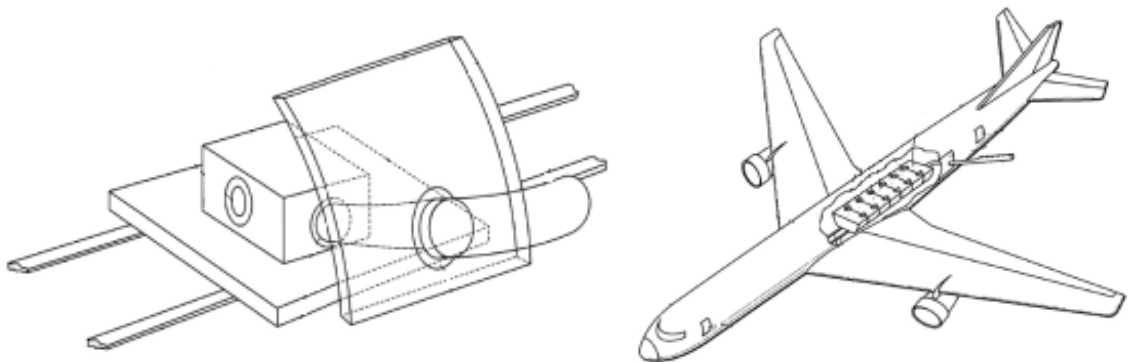


Figure 2-6 - Aerial Dispersion System [16]

Patent [17] is a truss shaped spraying apparatus with the capability of being released from the aircraft. This allows the pilot to jettison the system should it accidentally come in

contact with another object, improving safety. This particular design is for use on a helicopter, but is different from what is seen on spray booms for fixed wing aircraft today. Also, it has a jettisonable feature where the entire system can be dropped from the aircraft in the event of an emergency.

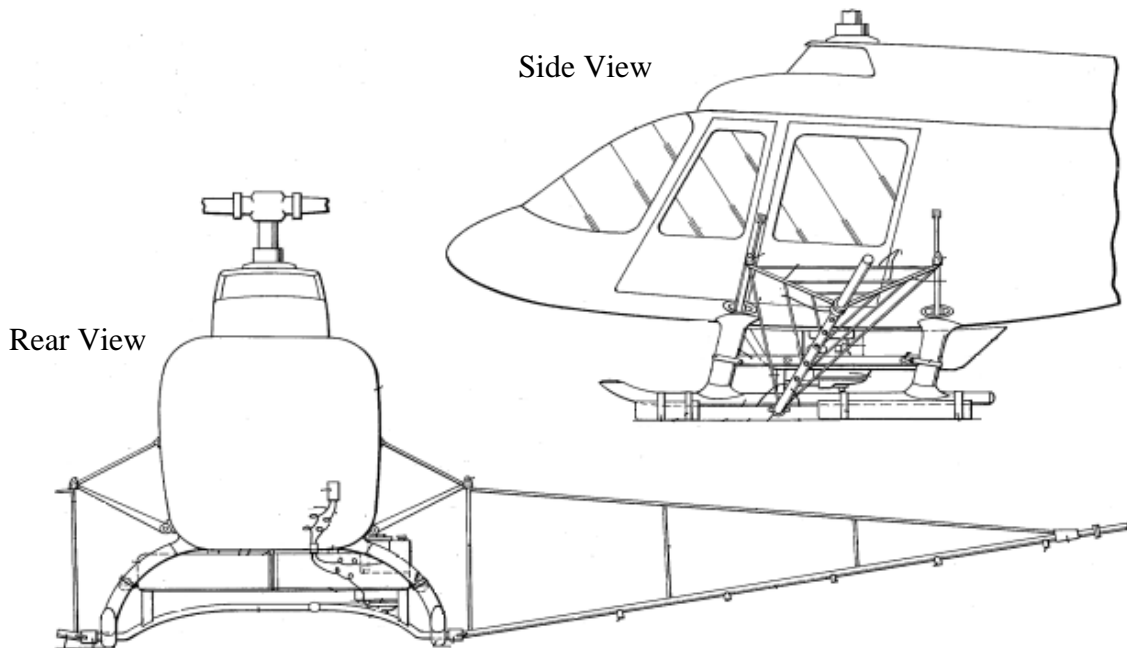


Figure 2-7 - Jettisonable Helicopter Spray Boom [17]

2.1.2. Existing Designs

Currently, there are several different aircraft types used for delivering chemical spray for various applications. The recent major oil spill in the Gulf of Mexico saw a large deployment of oil spill fighting aircraft. These existing designs can provide guidance for what works well, and can possibly be applied to the Dash 8 aircraft type.

There are two primary types of spray booms for fixed wing aircraft. Existing designs show that the spray boom can either be located on the wing, or extending from the rear fuselage. The C-130 aircraft shown in Figure 2-8 is an example of an existing spray boom design located further aft, with supporting structure. A truss structure is used to support the weight of the spray boom, and is attached near the forward end of the empennage. Because of its permanent external structure, there may be safety concerns with take-off and landing performance, as it may strike the ground or affect the flight performance at low speeds.



Figure 2-8 - C-130 Spray Boom Truss Design [18]

Figure 2-9 below shows the Airborne Dispersant Delivery System (ADDS) used during the Deep Water Horizon accident. It has a retractable boom, which partially retracts into the fuselage to reduce the drag created by the system. It does not have supporting structure, as seen in the previous example, but it does not extend as far from body of the aircraft. It is a similar system to the deployable dispersion system [16]. The partial

retraction reduces the drag generated by the system, improving the range and efficiency of the C-130.



Figure 2-9 - C-130 Retractable Spray Boom (ADDS System) [19]

Figure 2-10 is a modified DC-4 aircraft from Florida Air Transport, with an oil dispersant boom attached to the upper surface of the wings. This design is similar to what is seen in patents [12-14]. It is not retractable in flight, with a chemical reservoir located in the cabin of the aircraft. It is located directly on the wing surface, which may affect the airflow over the main lifting surface. Further, the structure may provide more locations for ice to begin forming, which would not be ideal for colder climates.



Figure 2-10 - DC-4 with Wing Mounted Spray Boom [20]

The ADDS system shown previously consists of a simple cylinder with spray nozzles attached. However, a foil shaped fairing surrounding the spray boom can greatly reduce the aerodynamic drag on the system [21]. Wickens investigates the aerodynamic drag of a spray boom design, and then compares that with a new foil shaped spray boom. The drag reduction is significant, from 5990N to 2970N of aerodynamic drag. Several other performance indicators show major improvements. The two boom types are shown in Figure 2-11.

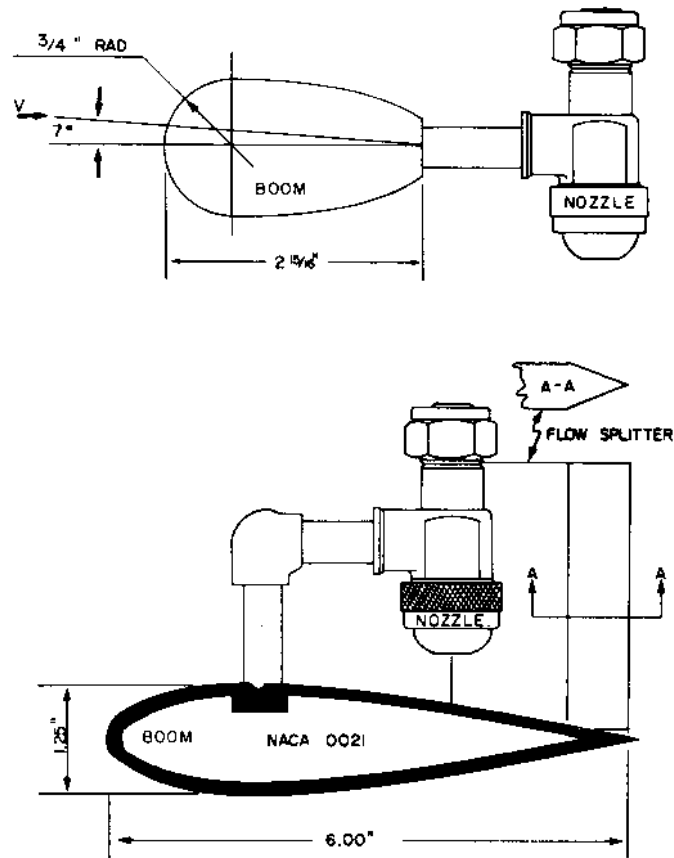


Figure 2-11 - Airfoil Shape Spray Boom [21]

The results of this investigation strongly suggest that a streamline boom shape is worth considering for any oil dispersal boom design.

2.2. Simplified Models

The primary stages of design are the initial conceptual design, followed by a preliminary design, and finished with a detailed or optimal design. Most engineering conceptual design studies begin by looking at a simplified comparable system to the design problem. Analytical approaches allow for preliminary design, providing a rough idea of the

solution. In many cases, the analytical approach can provide enough accuracy to solve the problem. However, even when the analytical approach does not provide the accuracy required, it could provide a basis for other approaches, giving a rough idea of what the expected value will be. This section provides a brief outline of current research in this area, and how it provides a benchmark for more complicated analysis.

2.2.1. Aerodynamic Loads

Analytical methods for determining the flow characteristics and aerodynamic loads on an object can quickly become complicated. The design scenario considered in this thesis can help narrow down relevant research in this vast field. Assuming a subsonic flight regime leads to validity of adopting an incompressible flow assumption.

Anderson [22] provides in-depth detail about of analytical methods used for aerodynamic analysis. With the stated assumptions, potential flow theory can be considered for determining pressure and aerodynamic loads around an object. Further methods such as the Joukowsky airfoil method can be used within potential flow theory to simulate the flow around a foil shape. This classical method can be used for complex flows and shapes. A problem arises with D'Alembert's paradox when calculating the drag load on a body. D'Alembert discovered a contradiction in the potential flow theory that suffers zero drag for a body in a constant velocity flow, which cannot be true. It was eventually discovered that the exclusion of the effects of viscosity has been determined to be the cause of this issue.

Another method for calculating the drag and lift on an object is to refer to empirical data gathered through wind tunnel measurements. Experiments have been conducted on standard shapes, including many different airfoil shapes. Various non-dimensional values are available for each shape, such as coefficient of drag, coefficient of lift, and coefficient of pressure. This method is efficient, and the preferred method if the data is available.

2.2.2. Structural Characteristics

Fundamental structural analysis methods are well developed. Mechanics of materials theories provide a thorough understanding of how materials behave under loading. Current research in this area focuses primarily on its use in the design process, as a benchmark for more complicated models.

Classical methods within mechanics of materials can be used in simplified engineering problems. It can be effective for many structural analysis applications, but as complexity increases, there is more need for more complex solution methods such as finite element analysis. Simplified analysis techniques provide a benchmark for the advanced engineering techniques, with a high degree of confidence in the solution. These analytical techniques can also be used for conceptual and preliminary design stages. Any standard mechanics of materials reference will suffice for the methods required for this thesis. Reference [23] is a suggested reference for analytical techniques in mechanics of materials.

Recent research in the area of analytical methods for structural analysis has been limited. An important stage in the design process is an initial simplified analytical model of the system, before moving into more complicated methods. Moore [24] outlines a new method of design optimization in order to reduce design cycle time and cost, that also improve optimization performance. It is broken down into several levels of analysis, the first level being a highly idealized and low fidelity conventional analysis. This stage uses simple analytical equations to provide an approximate loading. From here, optimization is carried out on increasing levels of model fidelity.

Boni [25, 26] presents an analytical method capable of defining fuselage sections of a transport aircraft. Finite element analysis is used in order to validate the results of the analytical approach. Analytical methods are used to calculate the shear flow in the fuselage skin under the floor loading and pressure loading of an aircraft. The typical shear flow equation fails when it is applied to a circumferential structure. The load coefficient method was demonstrated to be a reliable in representing how load is transferred to the aircraft fuselage. This method provides a way to calculate loads exerted on the fuselage from an external structure. It is also noted that some of the limitations of the analytical method, such as complex geometry, can be overcome through the use of FEA that can account for complex geometry, boundary conditions and interfaces, more realistic loading conditions, and local effects, closer to the aircraft frame such as joints and connections.

These analytical methods may be used to provide a general view of the loading interaction between system components, and the maximum overall stresses required for

system design. These results can be used in the initial design, as well as provide an initial optimization step. Further, these results can be used to benchmark the advanced engineering techniques such as FEA and CFD.

2.3. Detailed Design

Current research in the aerospace industry primarily focuses on computational analysis. It spans many different disciplines, including aerodynamics, structural mechanics, composites, and multi-disciplinary design methods.

2.3.1. Optimization

After an initial design has been created, it will meet most of its primary design requirements. It is often desired that the design be further refined from this point for cost, weight, and safety considerations. Weight optimization is a particularly strict design requirement on aircraft, and is considered at every design stage. This section will look at the design optimization process.

Within structural optimization, there are five main areas of research [27]. Guo and Cheng provide an excellent review of these primary areas of research, including several practical design examples. These areas include multi-scale optimization, multi-physics optimization, uncertainty based optimization, topology optimization, and the integration of optimization methods into analysis software. Figure 2-12 shows the integrated structural optimization steps of a door support arm on a Fairchild Dornier 728-100 aircraft. The initial design is followed by a finite element model, then an optimized

design, and the final result. This shows a practical and useful application of design optimization.

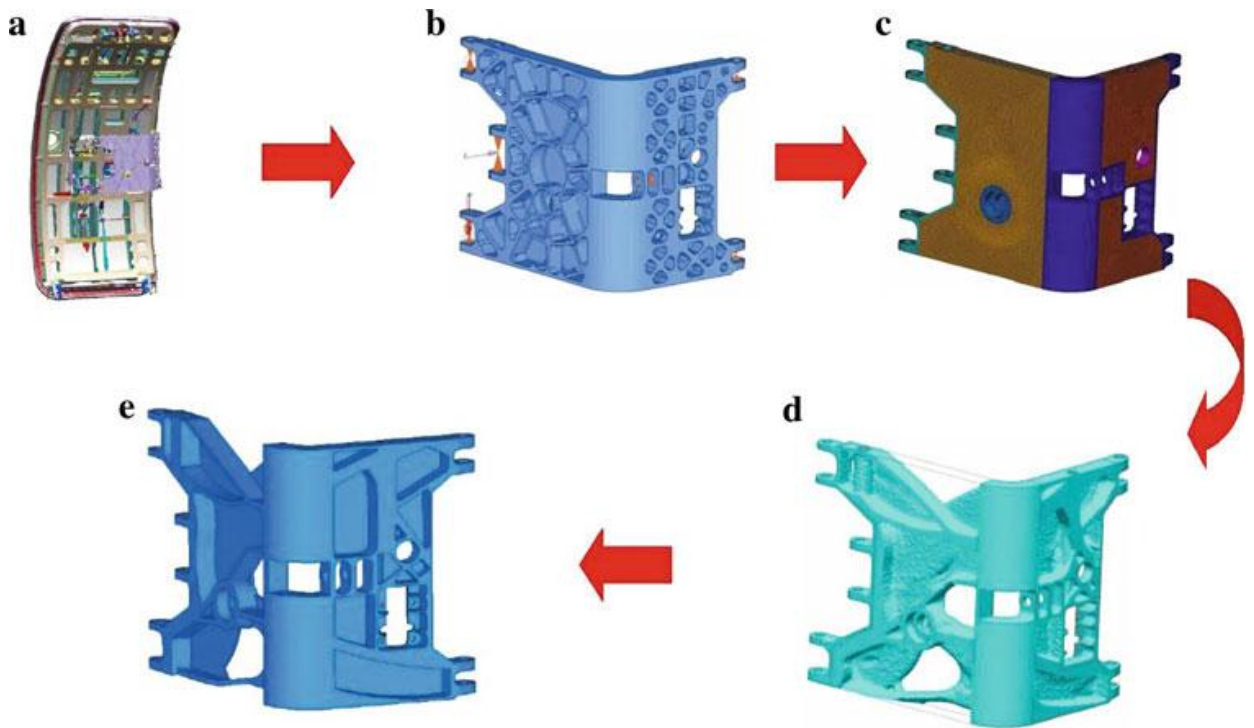


Figure 2-12 - Dornier 728-100 Optimized Door Support Arm [27]

Figure 2-12 provides an excellent example of topology optimization in a complex load setting. Colson [28] outlines four fundamental types of structural optimization including size, shape, topology and material, which is illustrated in Figure 2-13.

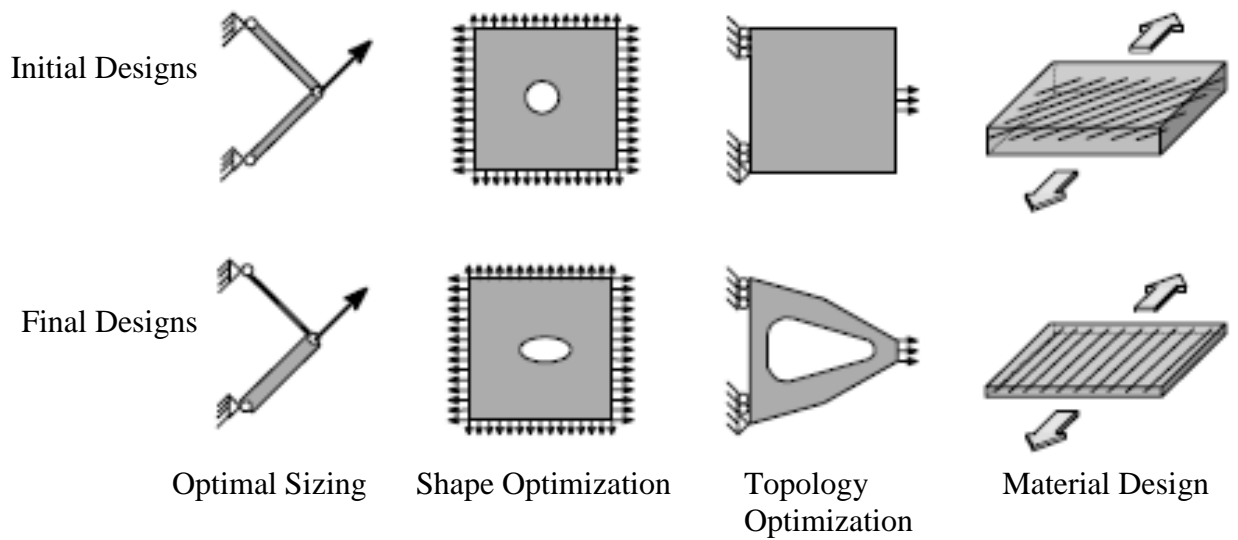
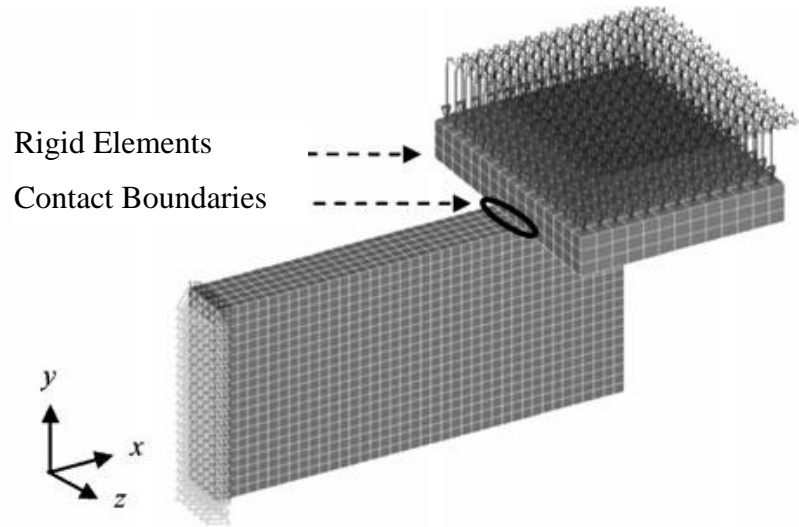


Figure 2-13 - Structural Optimization Problems [28]

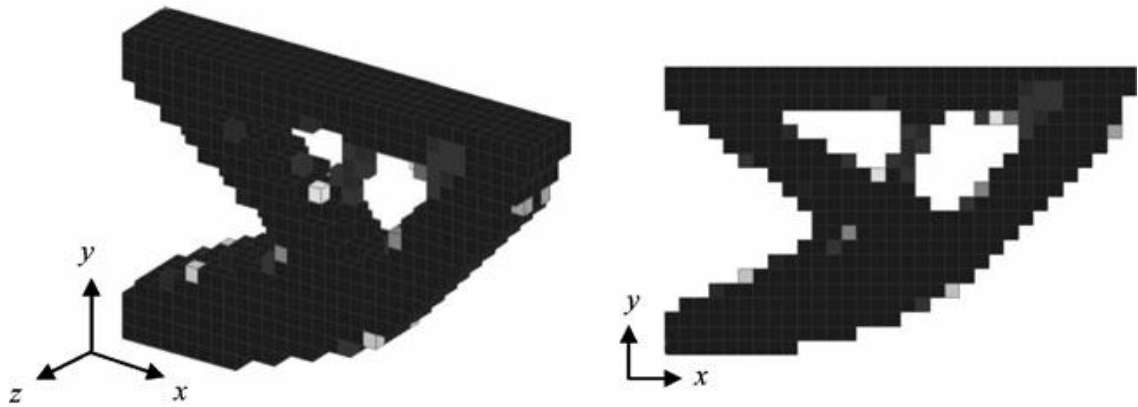
The first type is optimal sizing of system components. This involves optimizing the thickness and sizing of each component in the system. The example given in this case is the optimizing of truss member cross-sections based on the load each member carries. A larger stress means the thickness of the cross-section needs to be increased. The second optimization technique involves optimizing the shape. The shape of a cut will alter the stresses in the part. A shape with sharp corners will have concentrated stress, and rounding them off to avoid that issue can be considered shape optimization. The third optimization technique is topology optimization. Topology optimization seeks to reduce the weight within the system by removing as much material as is possible. The fourth optimization technique is material design optimization. Material design considers the ply angle and general construction of a composite material such that it is optimized for its particular loading conditions. The paper concludes that gradient-based methods are ideal,

and surrogate-based optimization methods are best suited for larger models. The paper and its references can be referred to for further information on these topics.

A common issue with real world design problems is the complicated nature of the boundary conditions, dynamic response, and multi-body components. Reference [29] provides a brief overview of structural optimization for nonlinear static analysis. There are many different areas covered in this paper, but it does provide several examples of topology structural optimization. Figure 2-14 a) presents an example of a boundary nonlinearity problem on a three dimensional part. These complex boundary conditions are difficult to include in the optimization process. The design optimization process described in the paper lead to the optimized results shown in Figure 2-14 b). The report concludes that the described design process using equivalent static loads (ESL) can be effectively used for nonlinear optimization problems.



(a) FE Model and Loading Conditions



(b) Results of Topology Optimization

Figure 2-14 - Topology Optimization with Complex Boundary Conditions [29]

Design optimization can be implemented in several ways, and at several stages of the design process. Taylor [30] demonstrates the evolutionary design process by following the structural design process of an aircraft wing. Both the technical and organizational design process reveals the importance of integrating design tasks and multidiscipline

communication. Figure 2-15 shows the general design process taken. Three stages of increasing design fidelity of an aircraft wing provide a balance between computational analysis and input from the multidiscipline team of engineers.

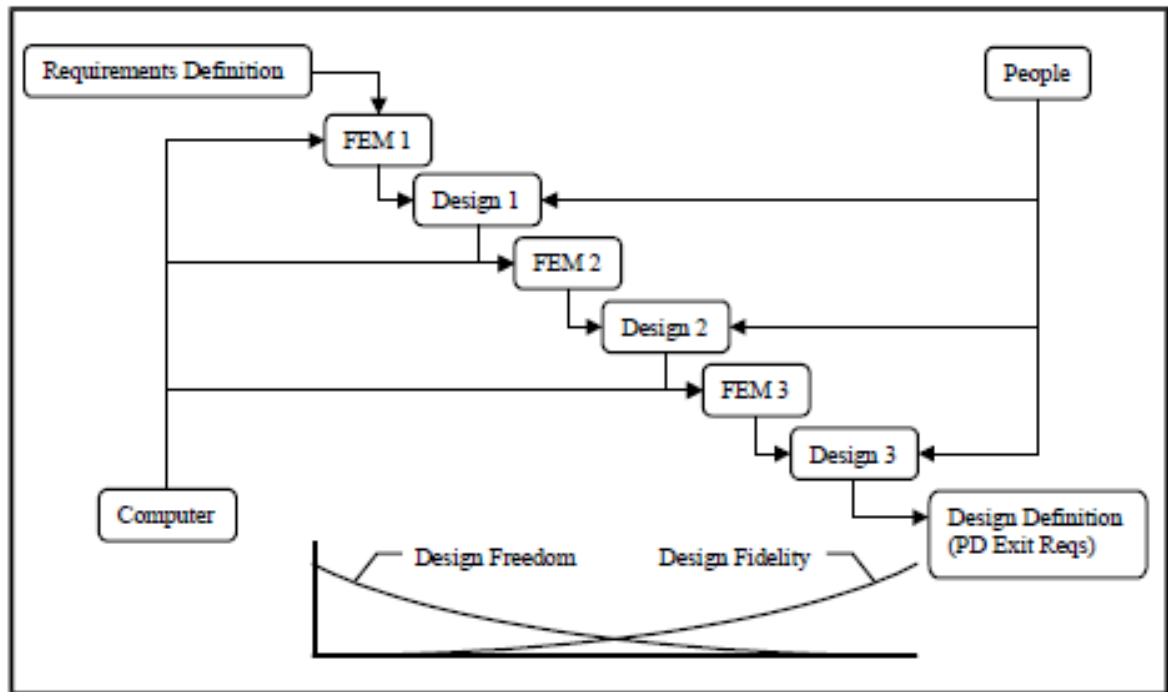


Figure 2-15 - Evolutionary Design Process [30]

This is an excellent model for integrating the benefits of computational analysis and optimization into the organizational engineering process that would exist in a smaller engineering design firm.

As seen earlier, Moore [24] also provides a very detailed aircraft structure design optimization using finite element analysis.

2.3.2. Computational Aerodynamic Analysis

Computational fluid dynamics remains one of the most complicated simulation tools in engineering. Current research in this field covers a wide area, from turbulent flow modelling, to supersonic flow. This thesis puts focus on the area of simple aerodynamic load calculations, due to the simplified geometry of the structure. Further detailed discussion on the history of CFD, applications, and higher order methods are presented in several studies [31, 32].

Nakayama [33] provides an in-depth flow analysis around a similar truss structure that was seen on the C-130. Drag coefficient and vortex shedding characteristics were determined with acceptable accuracy. Figure 2-16 shows the complex wake produced by the truss structure.

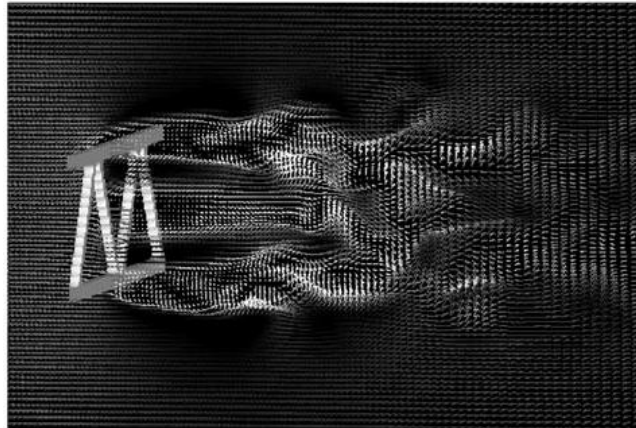


Figure 2-16 - Airflow around a Truss [33]

Many aerodynamics problems require more than simply calculating the aerodynamic loads. They also seek the understanding of the structural response. Coupling aerodynamic

simulation and structural simulation is of particular interest with several studies examining the issue of fluid-structure interaction in simulation that is focused on aeroelastic applications [34].

Computational fluid dynamics is a helpful tool in determining the expected aerodynamic loads in flight. In many cases, it is the only way of getting realistic loads short of carrying out physical tests. However, for simple geometry and in cases where incompressible flow is assumed, CFD may only provide a small increase in accuracy over analytical methods.

2.3.3. Aeroelastic Analysis

Fluid-structure interaction brings up a major issue that is the focus of much research in engineering. Multi-disciplinary analysis brings different fields of engineering together to solve complex problems. This brings up many technical and organizational issues. Its complex nature often leads to a sacrifice of quality and accuracy when each disciplinary problem is dealt with individually, rather than a coupled solution. This has been a highly researched area in the last decade, especially in the areas of design optimization, and aeroelastic analysis.

Current multidisciplinary analysis methods use a range of computational tools that combine to solve the complex interaction between aerodynamic forces, structural mechanics, dynamics, and electromechanical control. The I-STARS multidisciplinary analysis system shown in Figure 2-17 gives an overview of the multidisciplinary analysis concept and procedure for aircraft [35].

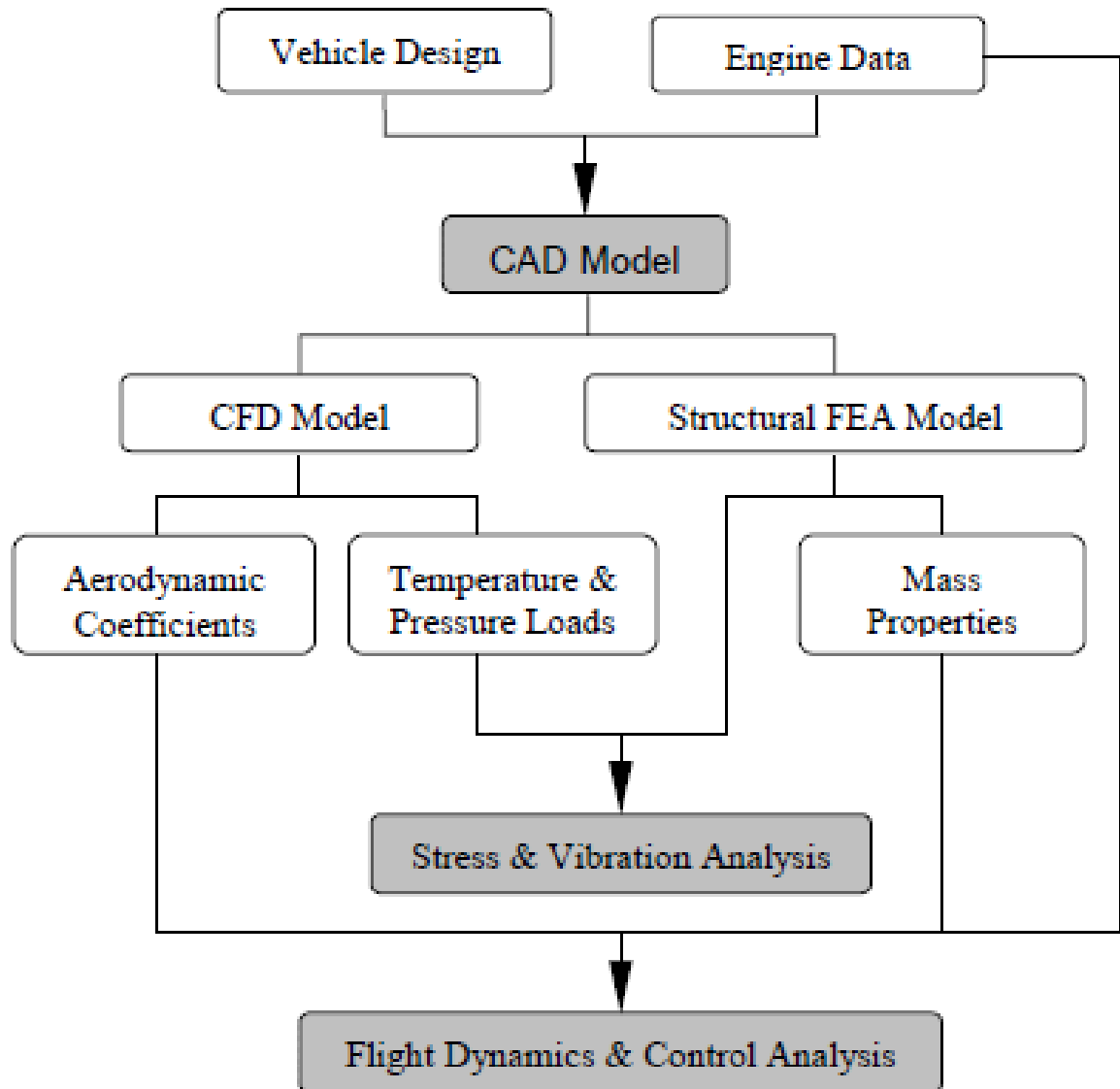


Figure 2-17 - I-STARS Multidisciplinary Analysis System [35]

I-STARS is the primary multidisciplinary FEA software and was developed by NASA Dryden Flight Research Center. It carries out multidisciplinary analysis by estimating

aerodynamic forces, and interpolating those forces onto FEA models. Several other programs are briefly outlined, and the report concludes with an efficient procedure and software interface for the design, modeling and analysis for aircraft configurations. Once a CAD model is created, FEA and CFD can be carried out, as seen in Figure 2-18. This research article provides an excellent insight into a practical example for using multidisciplinary analysis, and provides a roadmap of the design process.

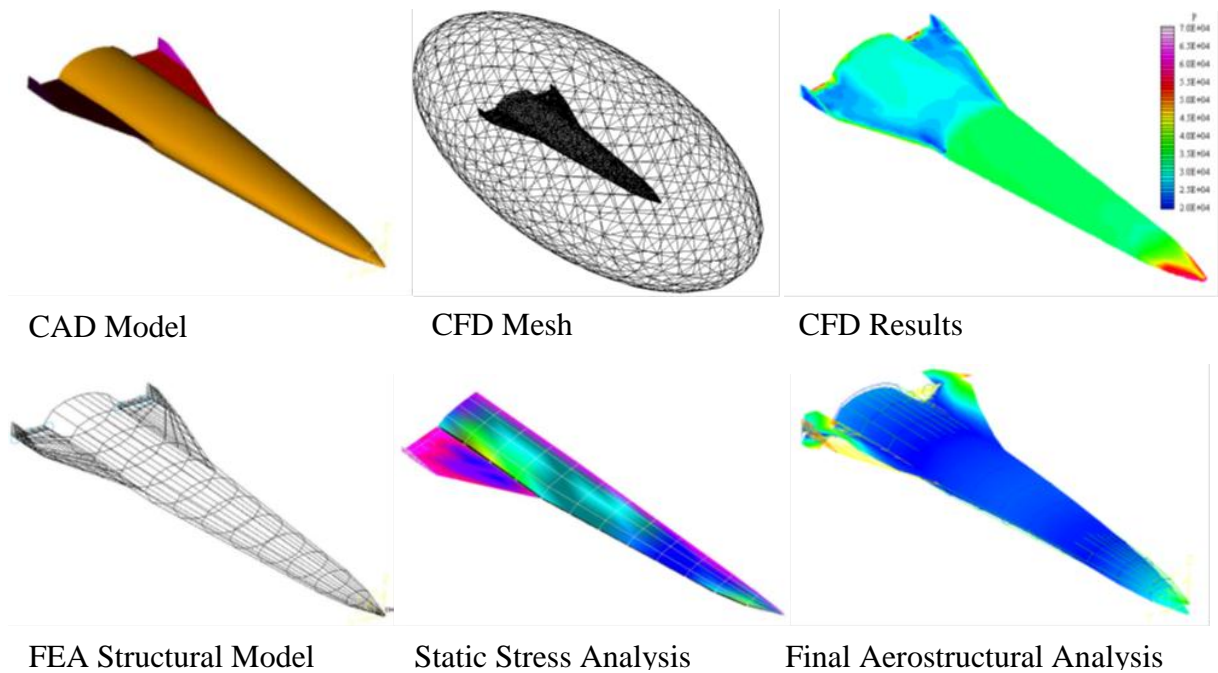


Figure 2-18 - Multidisciplinary Analysis - Fluid Structure Interaction [35]

Incorporating design optimization into multidisciplinary analysis is a particularly complicated problem, but can have major benefits. Sobieszczanski-Sobieski and Haftka [36] give a review of multidisciplinary design optimization within the aerospace industry. Three overall methods for multidisciplinary design optimization are outlined. The first

method takes careful note of important parameters from several disciplines, and manipulates them simultaneously, for an efficient design. This method is similar to the parametric design method, except it includes parameters from several disciplines, and intertwines the influencing factors for each parameter. The second method uses simple analysis tools, which are used in the conceptual design stage. The third method faces the organizational and computational challenges directly, through decomposition methods, global sensitivity and approximation methods. The paper concludes that multidisciplinary optimization has gone beyond its structural optimization roots. Uncertainty based design optimization was discussed previously, and is also considered in this setting. Uncertainty based design optimization provides a way to deal with competing objectives and variables involved with multidisciplinary design [37].

2.3.4. Dynamics

Vibration analysis is important as it may lead to dangerous conditions, which can be difficult to predict, as simulation techniques are complicated. Consider the boom structure dynamic analysis presented by Gomathinayagam et al. [38] where the vibration modes are calculated for an oil rig boom structure. An in-depth literature review in Table 2 provides many more sources for dynamic analysis.

2.4. Conclusion

This chapter provides a general overview of research in the aerospace industry. Particular focus was put on topics related to the design of an external aircraft component. Several conclusions can be made from the research in this literature review. Potential methods are

identified from this review and will be used to improve the design process relating to this thesis; also gaps in research are revealed.

Research in the area of design optimization and multi-disciplinary analysis is currently making large strides, and many new ideas on the design and optimization process will provide some guidance in the design stage of this thesis. Looking at existing designs and patents has also been invaluable. These designs provide a bench mark for initial sizing, streamlined shape, supporting structure, and highlight particular issues such as downwash effects that might have been overlooked.

Gaps in current research were seen to be in the area of detailed design. Many of the current computational tools continue to be improved, but there is still a significant disparity between its place in research and its role in everyday detailed design in the workplace. Multi-disciplinary design methods are a frequent topic of research, but are still rarely implemented in much of the industry. The industry still needs to be convinced of the value of tools such as finite element analysis for structural design, and therefore could benefit from more rigorous design case studies.

3. Preliminary Design

The preliminary design stage is the first step of the design process. A preliminary design will often employ simple analytical techniques in order to determine initial design parameters. These simplified techniques can be used to estimate stress and loading conditions, design geometry, and select material. Once a preliminary design has been completed, more advanced analysis methods such as CFD and FEA can be carried out for the purpose of verification, optimization, and identifying unexpected behavior.

This chapter will outline the steps that were taken to complete the preliminary design of the aircraft oil dispersant boom. Multiple designs will be considered at a conceptual level. A parametric study will identify all of the critical parameters required, and what factors influence the choice of each parameter. Following the parametric study, the initial design geometry will be chosen, along with material selection.

3.1. Conceptual Design

The first step of the preliminary design is to consider several possible solutions to the design problem. This level of design is often abstract, but serves the purpose of providing a foundation to the entire design process. There are usually multiple ways to solve a design problem, each with their own positive and negative points. A final concept choice must be rationalized. To do this, a simple ranking method is implemented to equally consider all options.

The initial concept of the oil dispersant boom for a fixed wing platform was derived from existing designs. As discussed in the literature review, several designs exist, using dispersant booms attached to the wing, the empennage, and deployable from an aft cargo bay door [18-21]. Through collaboration with the industry partner Provincial Aerospace the Dash 8 Q300 was selected as the design platform. The Dash 8 has become a popular aircraft for surveillance and search and rescue modifications, often fitted with a large number of sensors and radars. Due to the aircraft range, speed, cost, and availability, it is an ideal aircraft for retrofitting to fulfill the current research objectives. Several of these options can be applied to a Dash 8 Q300 aircraft.

The first concept considered is a simple fixed boom, with truss support, as seen in Figure 3-1. The boom would remain fixed during flight, and overall would be a simple design. However, the significant issue that arises for this concept is the safety considerations during take-off and landing. The Dash 8 Q300 aircraft is a significantly smaller aircraft, with a long fuselage, and there is a risk that the system may come in contact with the ground or affect the flight performance during this critical stage of flight. This significant concern led to the following more complicated designs.



Figure 3-1 - C-130 Spray Boom Truss Design [18]

In order to improve the safety of the oil dispersant system, it is preferred that it stow or retract, and then deployed when the aircraft reaches the oil slick. This complicates the design, but is deemed a vital design requirement, and therefore pursued.

Two options were considered for solving the safety issue: A system that can retract into the fuselage of the aircraft, and a system that would use a mechanism of linkages and an actuator to stow into the profile of the aircraft.

The internal retractable design concept would implement a design similar to an existing C-130 design seen in Figure 3-2.



Figure 3-2 - C-130 Side Retractable Boom [39]

This system would have a greatly reduced profile when retracted, solving the aerodynamic drag issue. It would require very few moving parts, meaning it would be robust and reliable. Figure 3-3 shows the retractable design applied to Dash 8 Q300 fuselage geometry.

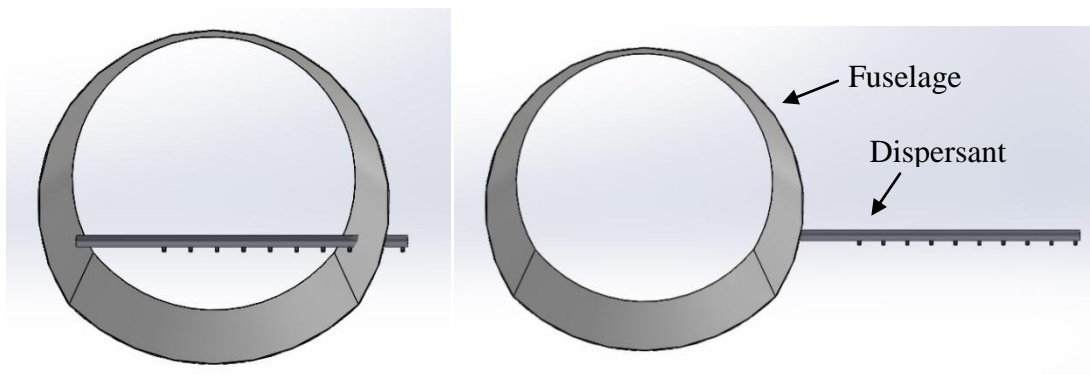


Figure 3-3 – Internal Retractable Boom

The length of the boom would be limited by the width of the fuselage. This limitation could be an issue, depending on the desired swath width. However, unlike the C-130, the

Dash 8 cabin is pressurized. This means that the retractable system could not retract into the pressurized area without major design considerations to abate the problem. Figure 3-4 from the structural repair manual shows the region in which the retractable system cannot be placed.

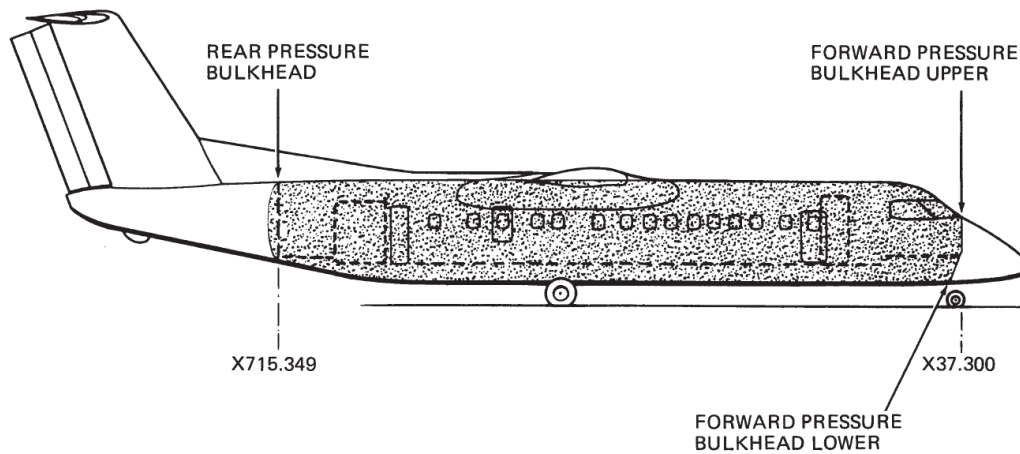


Figure 3-4 - Dash 8 - Pressurized Cabin [40]

Installing the system aft of the pressure bulkhead is an option, but the aircraft empennage has a greatly reduced diameter as compared with the fuselage. The reduced diameter means the retractable boom would be significantly shorter, and therefore less effective.

The last option considered is an external retractable system. The retractable system would consist of some mechanism to retract and deploy the boom during flight. It is proposed that a single support member also acts as a part of the actuating mechanism. See Figure 3-5 for a demonstration of this system. Having the boom in the aft side of the mechanism

provides support to the actuator from the aerodynamic loads as the system deploys. Further, it protects the mechanism from being exposed to the oil dispersant chemical.

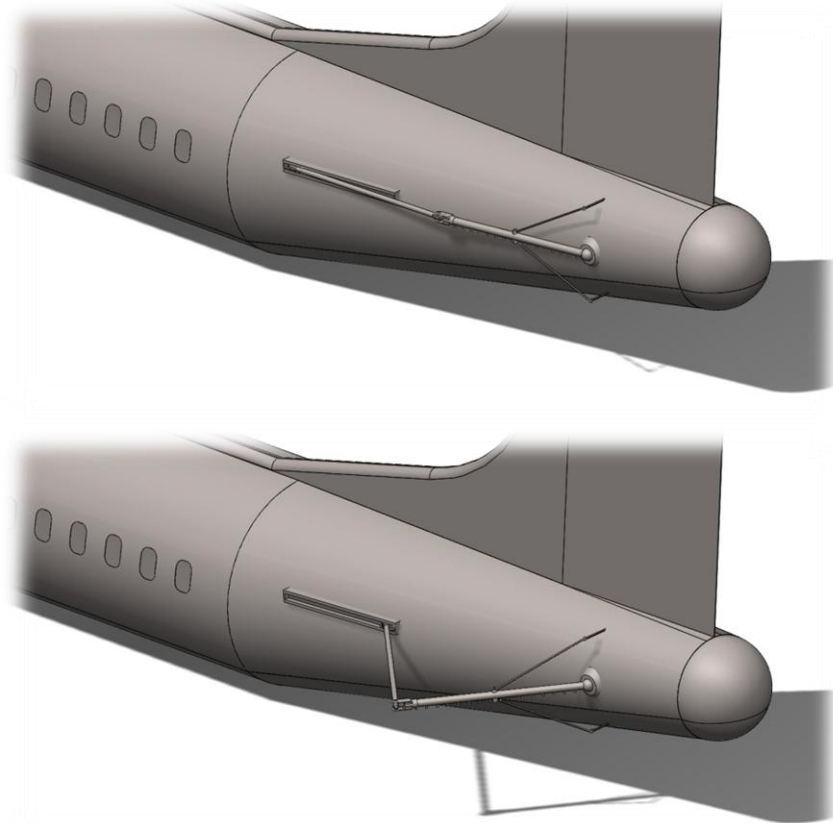


Figure 3-5 - Fully Stowed and Fully Deployed Oil Dispersant System

The mechanism in Figure 3-5 begins the flight fully stowed, as seen in the upper image. It sits closely to the aircraft fuselage, reducing drag. Once the aircraft reaches the site of the oil spill, a linear actuator seen as a track on the left applies force to the end of the system. This acts to deploy the system, pushing it outward. The linear actuator must simply reverse in order to retract the system.

Although this design is more complicated due to its actuating feature, it accomplishes all design requirements, and uniquely accommodates the Dash 8, and other similar aircraft of its class. Minor increases to the aerodynamic drag of the aircraft have a significant impact on range and efficiency. The ability to stow the system during transit to the offshore oil spill will increase the range, efficiency, system life, and enhance safety. This design was chosen as per the industrial partner's recommendation.

3.2. Parameter Identification

In any design, multiple parameters govern the overall outcome of the design. A parametric design method provides a standardized design process which can then be applied to multiple aircraft platforms. A parametric design is a design that is dependent on a set of parameters. When each parameter is modified, the overall design changes accordingly.

Once a general concept has been chosen, the geometry of the design must be defined. First, all parameters involved in governing the geometry of the design must be carefully defined. The system components consist of the dispersant boom, nozzles, actuating truss, actuator, vertical supports, rotating joints, and internal pump and reservoir. Figure 3-6 shows each of the system components, excluding the internal pump and reservoir.

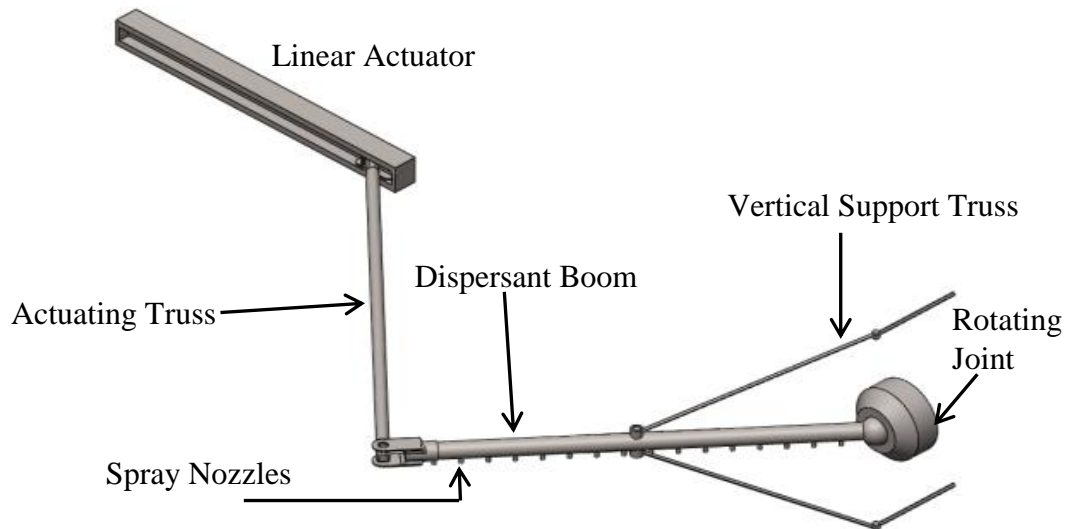


Figure 3-6 - Deployable Oil Dispersant System Components

These components can be grouped into two design categories, primary system components, and secondary system components. The primary system components consider the main structural components that define the system. These include the main boom, vertical support trusses, and actuating truss. The secondary system components are dependent on the primary system design, and will be considered at a later detailed design stage.

The nozzles and fluid dispersal equipment such as the pump and reservoir are dependent on the overall design. They have little to no effect on the geometry of the system, and can be more efficiently chosen once the final dimensions are defined. These will be considered as secondary system components and to satisfy flow rate requirements.

The actuator mechanism will be chosen once the wind loads and weight of the system have been determined from the primary system design, as it is dependent on the system geometry and material. Other detailed design issues such as the type of connections and hardware do not have a major impact on the overall design, and will also be considered as secondary system.

The primary design components will be the focus of the parametric design. As outlined previously, these components are the dispersant boom, actuating truss, and vertical truss supports. The parameters for each of these components will now be defined, and grouped into three categories, namely, performance, geometry, and strength categories, depending on their influencing factors.

The dispersant boom is a pipe that carries the oil dispersant to spray nozzles. It is defined by the pipe diameter, pipe thickness, length, and material properties. The actuator truss and supporting trusses will be solid rods, defined by their diameter, length, and material properties.

With the primary parameters identified, they can now be placed in an order that will subsequently help define the overall system. The influencing factors affecting each parameter define the order in which the design is defined.

The mission requirements provide a convenient place to start the parametric design. The goal of the oil dispersant system is to cover as much area as possible, using an adequate

spray rate. The flow within the pipe should remain laminar, for proper atomization of the fluid. This can be used to define the inner diameter of the pipe.

The chosen aircraft platform will come with its own inherent geometry restrictions. This can be used to define some overall dimensions of the system. The remaining parameters, such as pipe thickness, and material selection, will be dependent on minimizing the weight, and ensuring the stresses do not cause the structure to fail. The table below shows the list of parameters in this parametric design, and classes each parameter by their influencing factors.

Table 3-1 - Parameters and Influencing Factors

Parameters	Influencing Factors
D_i – Inner diameter of boom	} Fluid delivery requirements
L_1 – Boom length	
L_2 – Actuating truss length	} Geometry and limitations of aircraft
Θ - Angle of fully deployed boom	
E – Elastic modulus	
m_1 – Mass of boom	} Stress Requirements
m_2 – Mass of support	
t – Thickness of boom pipe	
L_c – Vertical support location	
D_T – Diameter of the support truss	

Figure 3-7 below shows the defined geometry, for visualization.

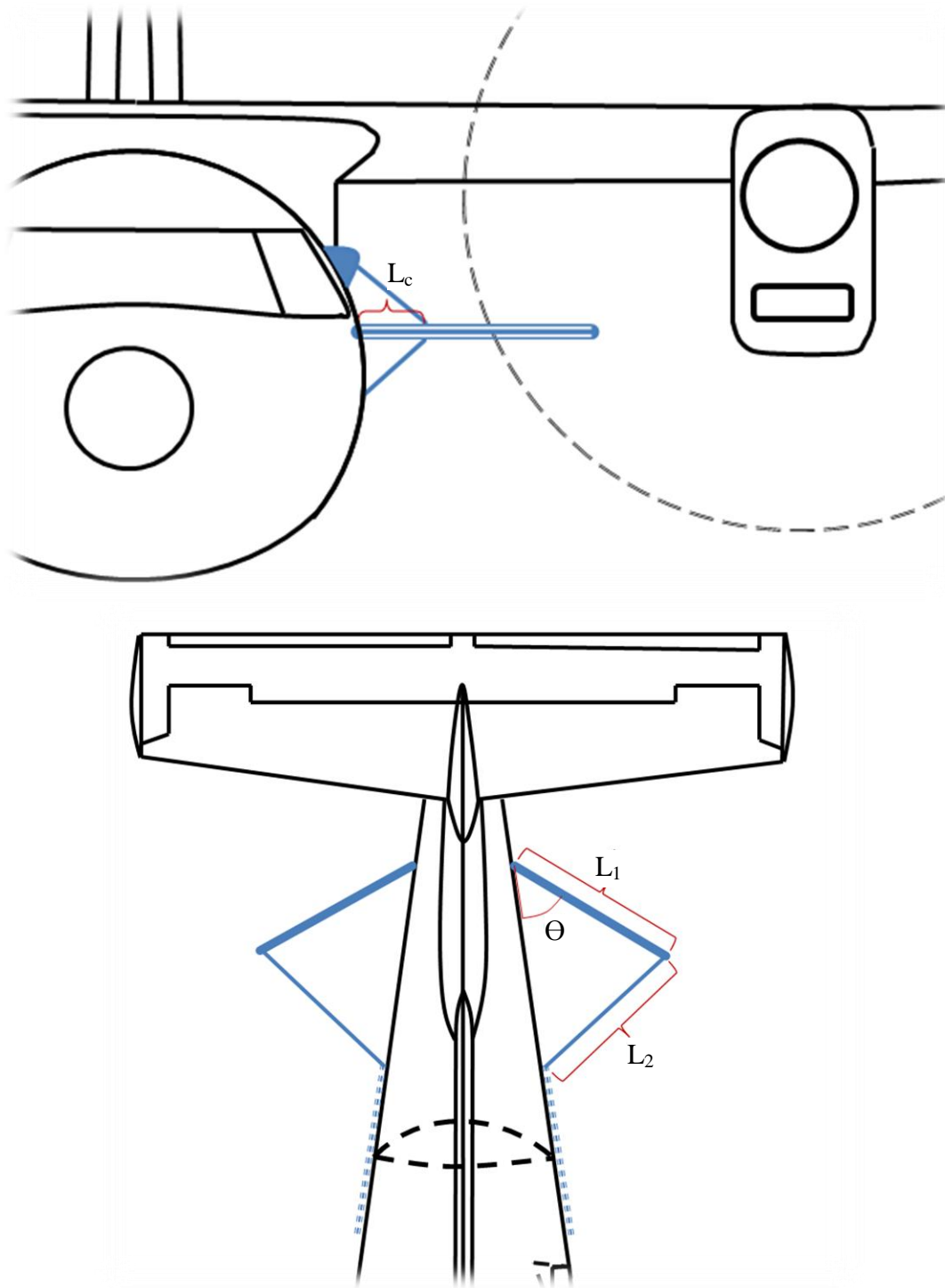


Figure 3-7 - Parameter Identification

3.3. Design Geometry

The parametric design is complicated by the large number of parameters. To narrow down the unknowns, it is beneficial to look at the geometry of the aircraft considered in this thesis, the Dash 8 Q300.

The inner diameter D_i is dependent on fluid delivery requirements. The flow within the pipe must remain laminar for ideal fluid atomizing through the nozzles. There also must be a high enough flow rate such that an oil slick is properly covered. The client has not specified application rate or diameter, but research into other aerial oil dispersant platforms provides a wide range of flow rates. The Alaska Department of Environmental Conservation lists that the maximum application rate for a C-130 aircraft using the Airborne Dispersant Delivery System (ADDS) system is 3020 L/min [41]. However, the Industry Technical Advisory Committee for oil spill response quotes an application rate of 1325 L/min, and suggests that lowering that rate to 870 L/min is allowable. This range can be used in determining the required inner diameter [42].

For a flow to remain laminar, it must stay under a Reynolds number of 2040 [43].

Reynolds number can be calculated as:

$$R_e = \frac{\rho U D}{\mu} \quad 3-1$$

Where ρ is fluid density, U is flow speed, d is the inner diameter of the fluid, and μ is dynamic viscosity. R_e is known, and U can be determined from flow rate Q . Fluid density and viscosity depend on the type of dispersant used. A common dispersant used today is

COREXIT 9500. This has a listed density of 968 kg/m^3 (0.968 g/mL), and a viscosity of 107 cP ($0.107 \text{ N} \cdot \text{s/m}^2$) [44]. To find the value of U , the volumetric flow rate equation is manipulated.

$$Q = \frac{\pi}{4} D^2 U \quad \rightarrow \quad U = \frac{4}{\pi} Q \frac{1}{D^2} \quad 3-2$$

Therefore,

$$R_e = 2040 = \frac{4Q\rho_a}{\pi\mu D} \quad 3-3$$

Rearranging for diameter,

$$D = \frac{Q\rho_a}{510\pi\mu} \quad 3-4$$

Using a range of 230 gal/min to 800 gal/min ($0.01451 \text{ m}^3/\text{s}$ to $0.05047 \text{ m}^3/\text{s}$), a range of acceptable diameters can be determined. This yields an inner diameter range from $D_i = 0.0819 \text{ m}$ to $D_i = 0.2850 \text{ m}$. This is a wide range of values, and any diameter within this range would be suitable. Pipe diameters in the upper range are not realistic, and would have to be very thick to prevent buckling and high stress. Choosing a diameter that is similar to existing systems, and is a commonly manufactured size provides the most realistic solution. The retractable system seen on the C-130 in Chapter 2 has a diameter in the range of 0.1016 m to 0.127 m (4 to 5 inches). Choosing a diameter 0.1016 m (4 inches) for the inner diameter was decided.

Further parameters can be determined based on the limitations placed by the layout of the internal structure of the aircraft. The attachment points must be located by the internal structural frames, as the aircraft skin is not designed to carry extra external loads. Also, attachments can pick up on existing rivet locations, reducing the number of extra holes needed to be drilled. Figure 3-8 shows the location of the frames in the aft of the fuselage and tail section of the Dash 8 Q300.

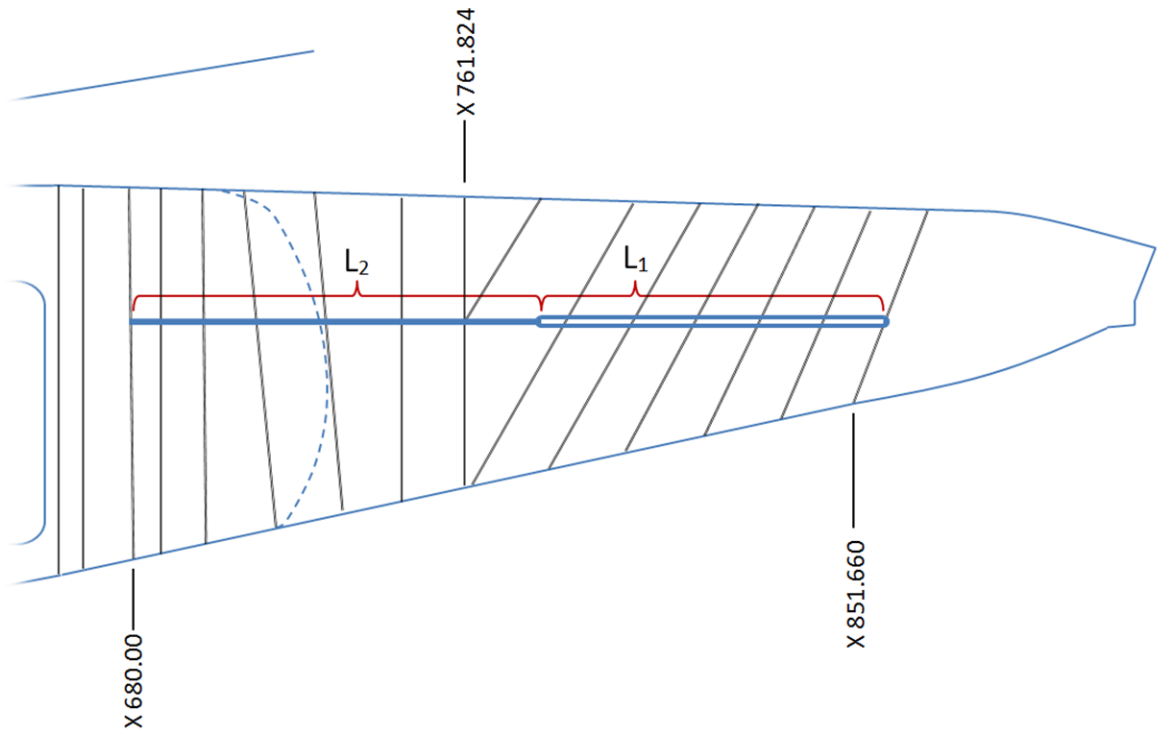


Figure 3-8 - Dash 8 Showing Frame Locations

It was decided that the ideal attachment points should be located on frame X 680.00 and X 851.660. When the system is fully stowed, it should have a total length of 4.59m.

The ratio of lengths between the main dispersant pipe L_1 and the supporting arm L_2 can now be chosen. When the system is fully deployed, and experiences the maximum amount of wind load, it would be ideal to have the actuating truss under purely axial loading. This means that the actuating truss must be at a right angle with the boom.

A larger angle θ is preferred, to maximize the width of the spray. To achieve this, L_2 must be longer than L_1 , but the total length $L_1 + L_2$ must remain 4.59 meters in length. A 2.134 m pipe (7 ft) results along with an 2.454 m support member (8 ft), giving a θ of 49.0° . Figure 3-9 demonstrates the fully axial force present in the actuating truss.

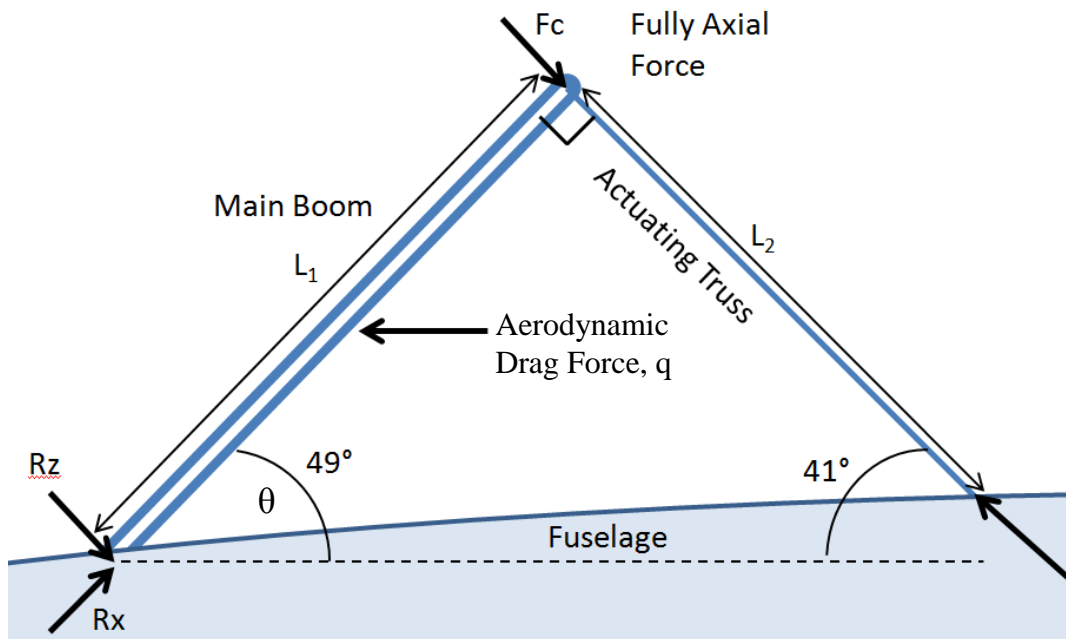


Figure 3-9 - Right Angle of Fully Deployed Boom

Stress requirements govern the remaining parameters. Using the dimensions determined above, the remaining parameters can be determined by minimizing stress and weight.

3.4. Stress Analysis

With the geometry determined, the stress can now be written as a function of material, and pipe thickness. A comparison of the minimum allowable pipe thickness will provide some guidance over what material should be chosen. The primary goal is to reduce the weight of the pipe, which is a function of the allowable stresses that occur due to bending and shear.

Although the system will be subject to dynamic loading as it deploys and stows, a maximum loading case of a fully deployed position will be considered. In this situation, it can be treated as a statics problem. The primary goal of this exercise is to become aware of what kinds of stresses exist in the boom, and to provide a preliminary design using simple engineering analysis.

The dispersant boom is under aerodynamic and inertia load. Aerodynamic loads are highest on this boom as it has the largest cross-sectional geometry in the dispersant system. The fluid flowing inside the boom will result in significant inertia loads on the boom in the case of any disturbance. Therefore, the dispersant boom will be the focus of the stress study.

The boom is subject to two primary loads: wind loads and inertia loads. The wind loads occur in the horizontal plane, and the inertia loads occur in the vertical plane. The two loads are fully out of plane with each other, and will be considered separately.

In the horizontal plane, the boom experiences a distributed wind load over the length of the boom. The wind load on the actuating truss will be ignored, since it will be much smaller than the boom wind load, and the solution is much simpler as a result. The wind load, q , is always going to act in the direction of the air flow. Because of this, there will be a normal and axial component of the wind load acting on the boom, as seen in Figure 3-10.

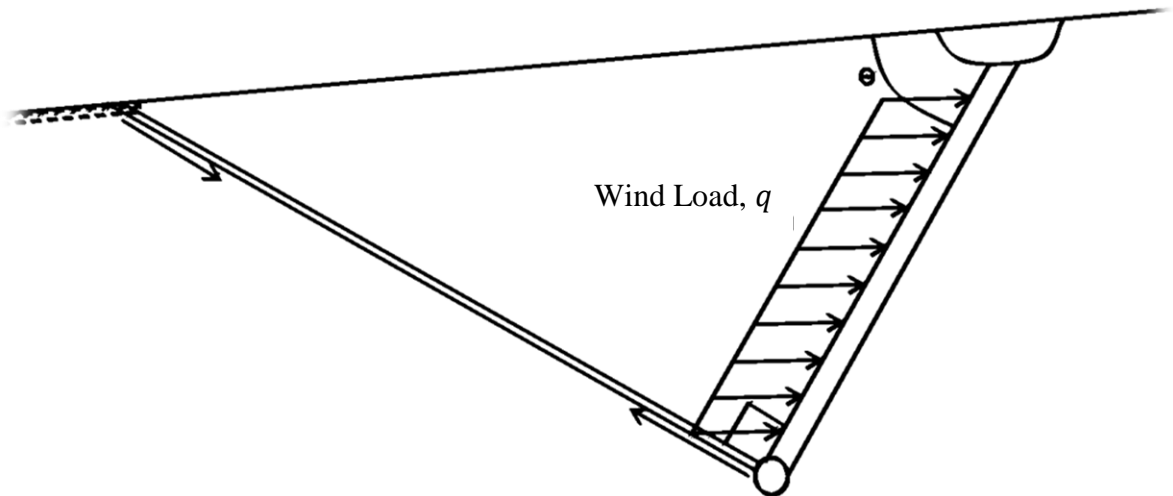


Figure 3-10 - Wind Load on Main Boom

The load was resolved normal and parallel to the boom. The boom will be considered a cylindrical pipe beam, with a pin connection at the base, and a roller connection at the

actuated truss connection. The roller connection will represent the normal loading effect on the actuated truss. The roller connection does not restrict movement or deflection in the axial direction. Figure 3-11 shows the simplified model for the horizontal loads with the corresponding shear and moment diagrams below it.

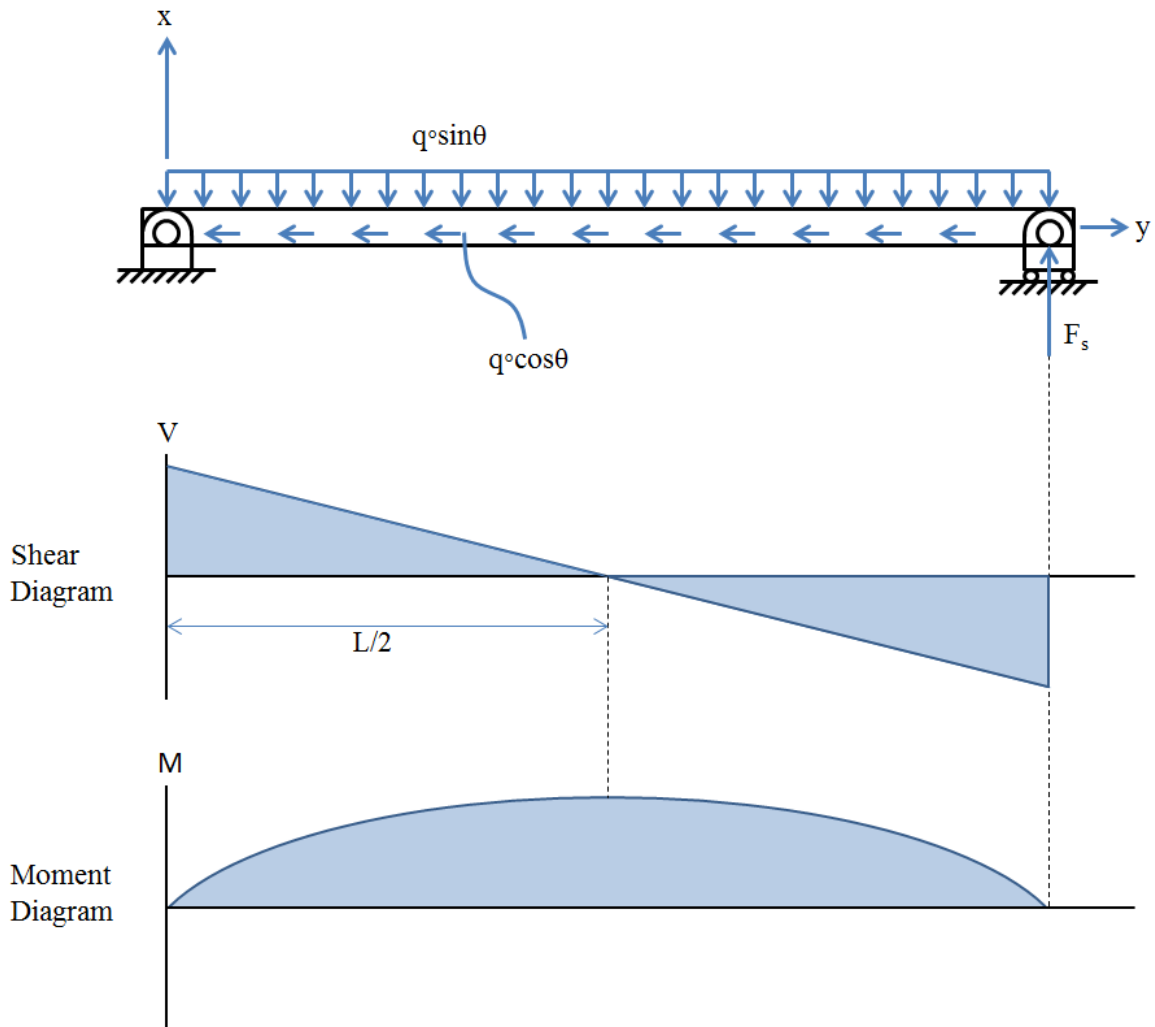


Figure 3-11 - Wind Load - Distributed Load

The shear and moment diagram show that the maximum stress as a result of the wind loads is located in the center of the boom.

To determine the stress in the boom, the reaction forces must first be defined. The sum of the moments around the origin is:

$$\sum M_o = 0 = -\frac{q \sin \theta L_1^2}{2} + F_s L_1 \quad 3-5$$

Rearranging this equation provides a solution for the actuating truss reaction force F_s :

$$\boxed{F_s = \frac{q \sin \theta L_1}{2}} \quad 3-6$$

Next, the sum of the forces in the y direction yield the reaction force R_y :

$$\sum F_y = 0 = R_y + F_s - q \sin \theta L_1 \quad 3-7$$

$$\boxed{R_y = q \sin \theta L_1 - F_s = \frac{q \sin \theta L_1}{2}} \quad 3-8$$

Finally, the sum of the forces in the x direction yield the axial reaction force R_x :

$$\sum F_x = 0 = R_x - q \cos \theta L_1 \quad 3-9$$

$$\boxed{R_x = q \cos \theta L_1} \quad 3-10$$

The x direction stress component for the horizontal has contributions from both the bending stress and the axial stress.

$$\sigma_{x_{horz}} = \frac{My}{I} + \frac{q \cos \theta x}{A L_1} \quad 3-11$$

The internal moment can be expressed as a function of x :

$$M(x) = R_y x - \frac{q \sin \theta x^2}{2} = \frac{q \sin \theta}{2} (L_1 x - x^2) \quad 3-12$$

The moment of inertia for a tube is:

$$I = \frac{\pi}{4} \left(\left(\frac{d_o}{2} \right)^4 - \left(\frac{d_i}{2} \right)^4 \right) \quad 3-13$$

Substituting the moment of inertia, area, and moment equations into the x stress component yields:

$$\sigma_{x_{horz}} = \frac{2q \sin \theta (L_1 x - x^2) y}{\pi \left(\left(\frac{d_o}{2} \right)^4 - \left(\frac{d_i}{2} \right)^4 \right)} + \frac{q \cos \theta}{\pi \left(\left(\frac{d_o}{2} \right)^2 - \left(\frac{d_i}{2} \right)^2 \right) L_1} x \quad 3-14$$

The maximum stress is located on the outer edge of the boom, where $y = r_o$. However, the maximum shear is located at the center. The shear from the wind load has no effect on the stress at point A. The shear from the inertia components does affect the principal stresses at point A, and will be seen later.

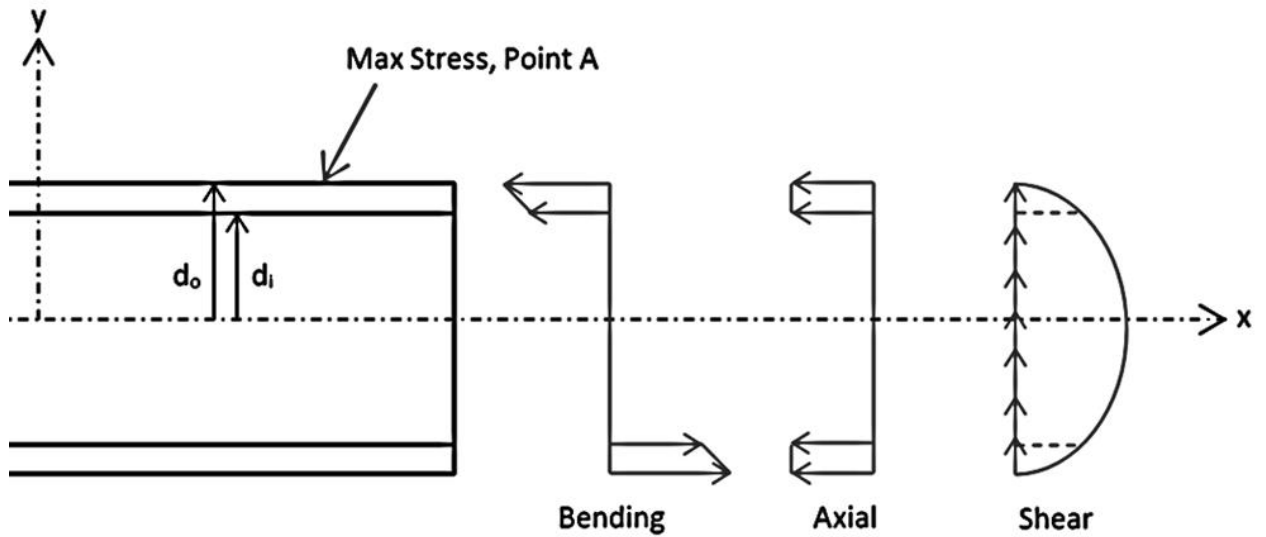


Figure 3-12 – Maximum Stress Conditions Resulting from Inertial Loads

The principal stresses at A can be expressed by:

$$\sigma_1, \sigma_2 = \frac{\sigma_x + \sigma_y}{2} \pm \sqrt{\left(\frac{\sigma_x - \sigma_y}{2}\right)^2 + \tau_{vert}^2} \quad 3-15$$

The maximum shear in the pipe is said to be:

$$\tau_{horz} = \frac{VQ}{It} = \frac{4V}{3\pi} \left(\frac{r_o^2 + r_o r_i + r_i^2}{r_o^4 - r_i^4} \right) = \frac{2qL_1 \sin \theta}{3\pi} \left(\frac{r_o^2 + r_o r_i + r_i^2}{r_o^4 - r_i^4} \right) \quad 3-16$$

Equation 3-16 can also be simplified by using the thin wall approximation equation.

$$\tau_{horz} = \frac{4V}{3A} \quad 3-17$$

Since the maximum stress from bending is located at the midpoint, the maximum stress in the x direction from the wind load is:

$$\sigma_{x_{horz}} = \frac{2q \sin \theta \left(\frac{L_1^2}{4}\right) \left(\frac{d_o}{2}\right)}{\pi \left(\left(\frac{d_o}{2}\right)^4 - \left(\frac{d_i}{2}\right)^4\right)} + \frac{q \cos \theta}{2\pi \left(\left(\frac{d_o}{2}\right)^2 - \left(\frac{d_i}{2}\right)^2\right)} \quad 3-18$$

The boom will be supported by two simple trusses in the vertical direction. One support will be located above the boom, and one below. The reason for this is that the high inertial loads can be experienced both upwards and downwards due to extreme turbulence. The standard flight envelope for an aircraft of this type has a survivable accelerations rating ranging from -3 to 6.5 times gravity. Beyond this point, structural failure occurs on critical aircraft components. However, as per discussions with the industry partner, a design load of 10 times gravity will be used to represent worst case scenario turbulence. It is noted that designing the oil dispersant system beyond the point of structural failure of the aircraft itself is not necessary. Standard design practices suggest that 2 to 3.8 times gravity would more than suffice for the design of a non-structural component on an aircraft as it represents the limit manoeuvring load factor experienced during flight [45]. However, industry often uses predicted crash loads as its design load, which can be as high as 10 times gravity, and will be used in this case as per discussions with industry partner. The weight of the actuating truss is approximated as

evenly distributed point mass between the boom and the connection to the actuator.

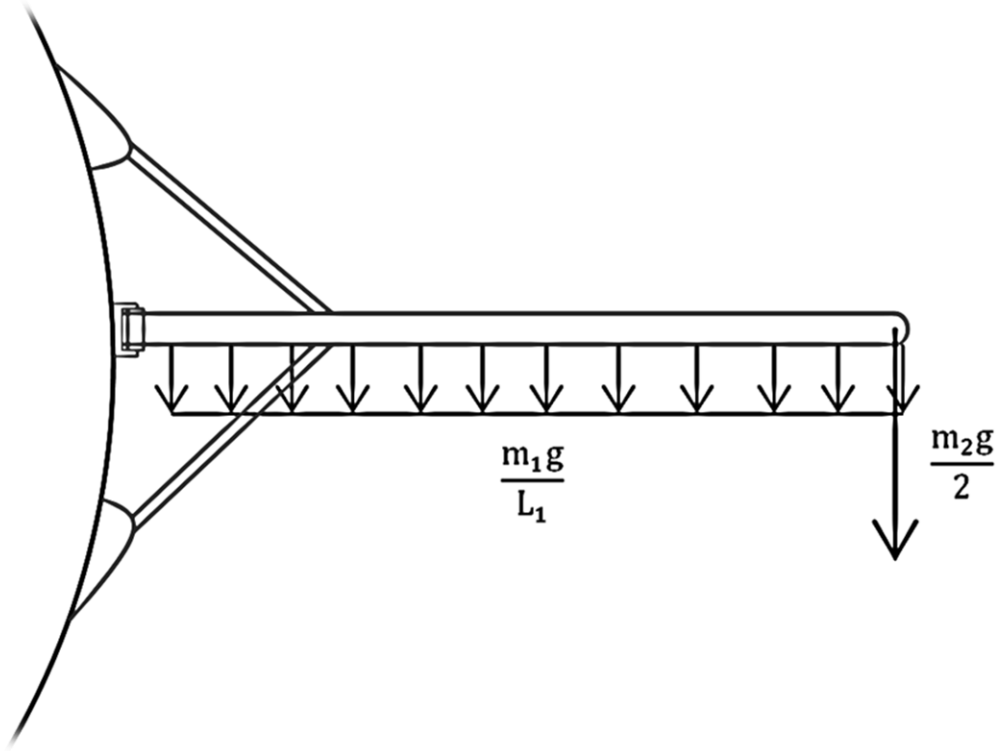


Figure 3-13 - Vertical Loading Scenario - Lumped Mass of Actuating Truss

The pinned joint at the base of the boom does not rotate in the vertical direction, and is considered as a fixed connection. The fixed connection prevents rotation and translation. Due to symmetry, the force in the trusses will be equal, with one in tension and one in compression. With the truss supports, this problem becomes an indeterminate beam to the first degree.

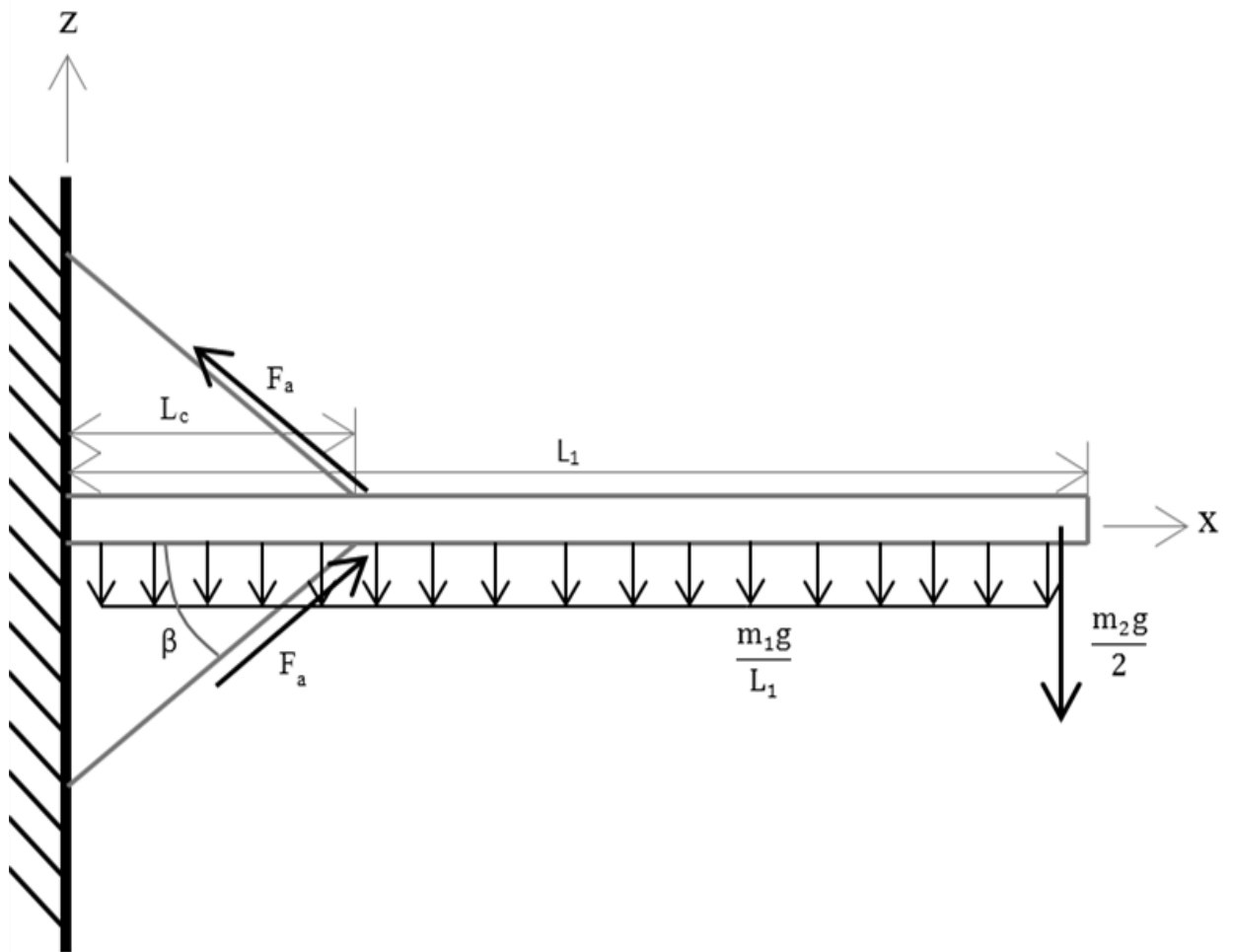


Figure 3-14 - Main Boom under Inertial Loading

There are several options to solve the reaction loads in an indeterminate beam. Since this is a parametric study, it is desirable to keep the solution relatively simple. The unit force method provides a convenient way to solve the indeterminacy.

The unit force method determines the redundant force by superposition of a beam without the redundant force, and a beam with unit force applied in place of the redundant force. Determining the deflection from a unit force essentially gives a value of deflection per

unit force. When that deflection per unit force is multiplied by the unknown redundant force, it will give the deflection as a result of that force. If the deflection at that calculated point is zero, or known, then superposition can be used to solve for the unknown force. The equation is given as:

$$\Delta + fP = 0 \quad 3-19$$

Where Δ is the deflection of the beam without the redundant force, f is the deflection per unit force, and P is the redundant force. Rearranging this equation gives a solution for the redundant force:

$$P = -\frac{\Delta}{f} \quad 3-20$$

The force in the truss support is chosen to be the redundant. The deflections at the redundant point will be used for the superposition equation. The deflection at point C will not be 0, but will be a function of the redundant force. The vertical component of the deflection of the truss supports will replace the zero deflection in the equation, yielding:

$$\Delta_c + f_c 2F_a = \frac{2F_a L_c}{A_a E_a} \sin \beta \quad 3-21$$

First, the deflection of the beam without a redundant force, denoted as Δ_x , is considered:

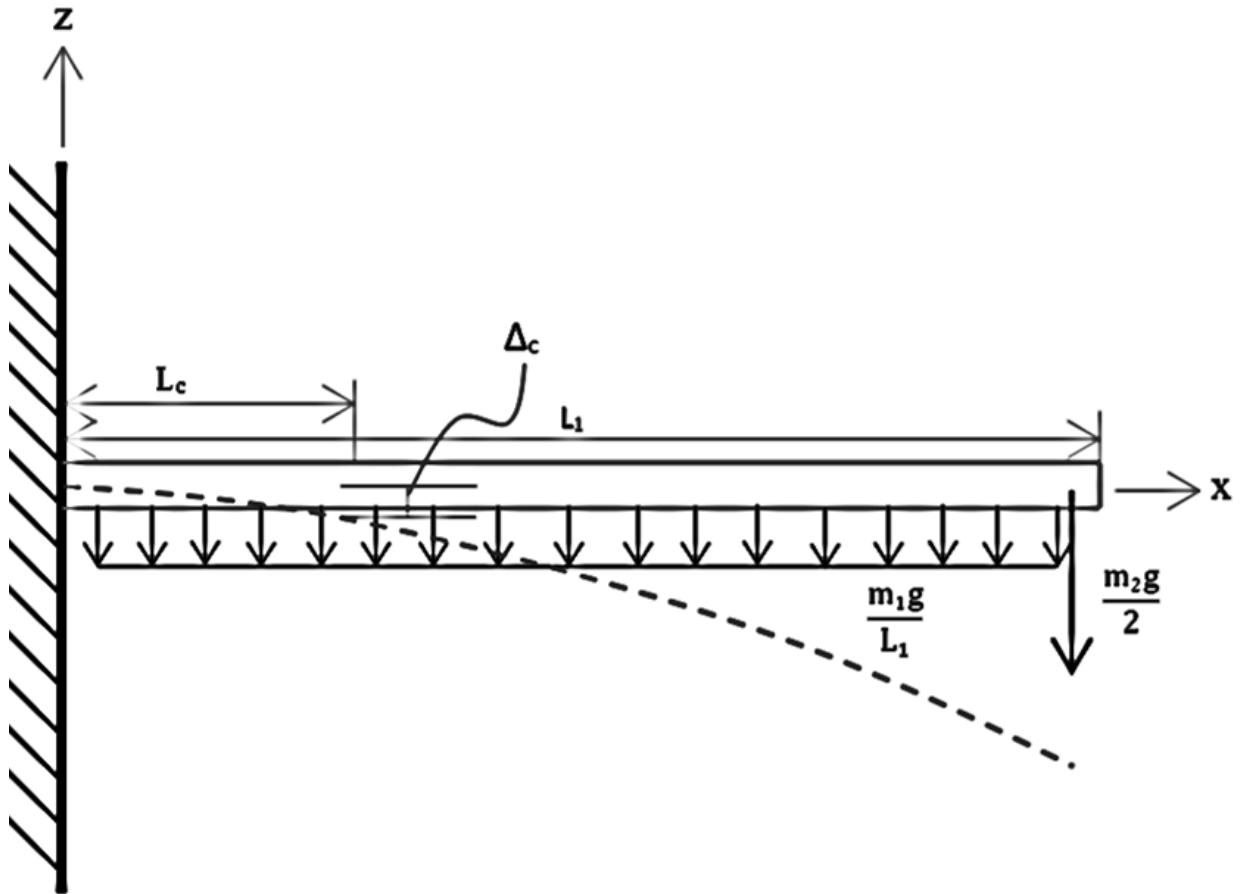


Figure 3-15 - Unit Force Method - Remove Redundant Force

This problem is determinate, and can be solved normally. The sum of the moments and forces can determine the reaction forces:

$$\sum M_o = 0 = M_a - \frac{m_1 g L_1}{2} - \frac{m_2 g L_1}{2} \quad 3-22$$

$$\boxed{M_a = \frac{m_1 g L_1}{2} + \frac{m_2 g L_1}{2}} \quad 3-23$$

$$\sum F_z = 0 = R_z - m_1 g - \frac{m_2 g}{2} \quad 3-24$$

$$\boxed{R_z = m_1 g + \frac{m_2 g}{2}} \quad 3-25$$

Next, using Macaulay method [46], the deflections can be calculated:

$$EI \frac{d^2 \Delta_x}{dx^2} = M(x) = -\frac{m_1 g L_1}{2} - \frac{m_2 g L_1}{2} + m_1 g x + \frac{m_2 g}{2} x - \frac{m_1 g}{L_1} x^2 \quad 3-26$$

Integrating this twice yields a solution for the deflection

$$EI \frac{d \Delta_x}{dx} = -\frac{m_1 g L_1}{2} x - \frac{m_2 g L_1}{2} x + \frac{m_1 g}{2} x^2 + \frac{m_2 g}{4} x^2 - \frac{m_1 g}{3 L_1} x^3 + C_1 \quad 3-27$$

$$EI \Delta_x = -\frac{m_1 g L_1}{4} x^2 - \frac{m_2 g L_1}{4} x^2 + \frac{m_1 g}{6} x^3 + \frac{m_2 g}{12} x^3 - \frac{m_1 g}{12 L_1} x^4 + C_1 x + C_2 \quad 3-28$$

Since it is a fixed beam, the following boundary conditions can be used to determine the constants of integration:

$$\Delta_x = 0 \text{ at } x = 0 \quad \frac{d \Delta_x}{dx} = 0 \text{ at } x = 0$$

Therefore, $C_1 = 0$, $C_2 = 0$

To summarize, the deflection in the beam at some point x is said to be:

$$\Delta_x = -\frac{m_1 g L_1}{4EI} x^2 - \frac{m_2 g L_1}{4EI} x^2 + \frac{m_1 g}{6EI} x^3 + \frac{m_2 g}{12EI} x^3 - \frac{m_1 g}{12 L_1 EI} x^4 \quad 3-29$$

The deflection at location L_c without the redundant force is:

$$\Delta_c = -\frac{m_1 g L_1 L_c^2}{4EI} - \frac{m_2 g L_1 L_c^2}{4EI} + \frac{m_1 g L_c^3}{6EI} + \frac{m_2 g L_c^3}{12EI} - \frac{m_1 g L_c^4}{12L_1 EI} \quad 3-30$$

Next, the deflection per unit force must be determined. A unit force is applied in the direction of the redundant force. All other forces are removed.

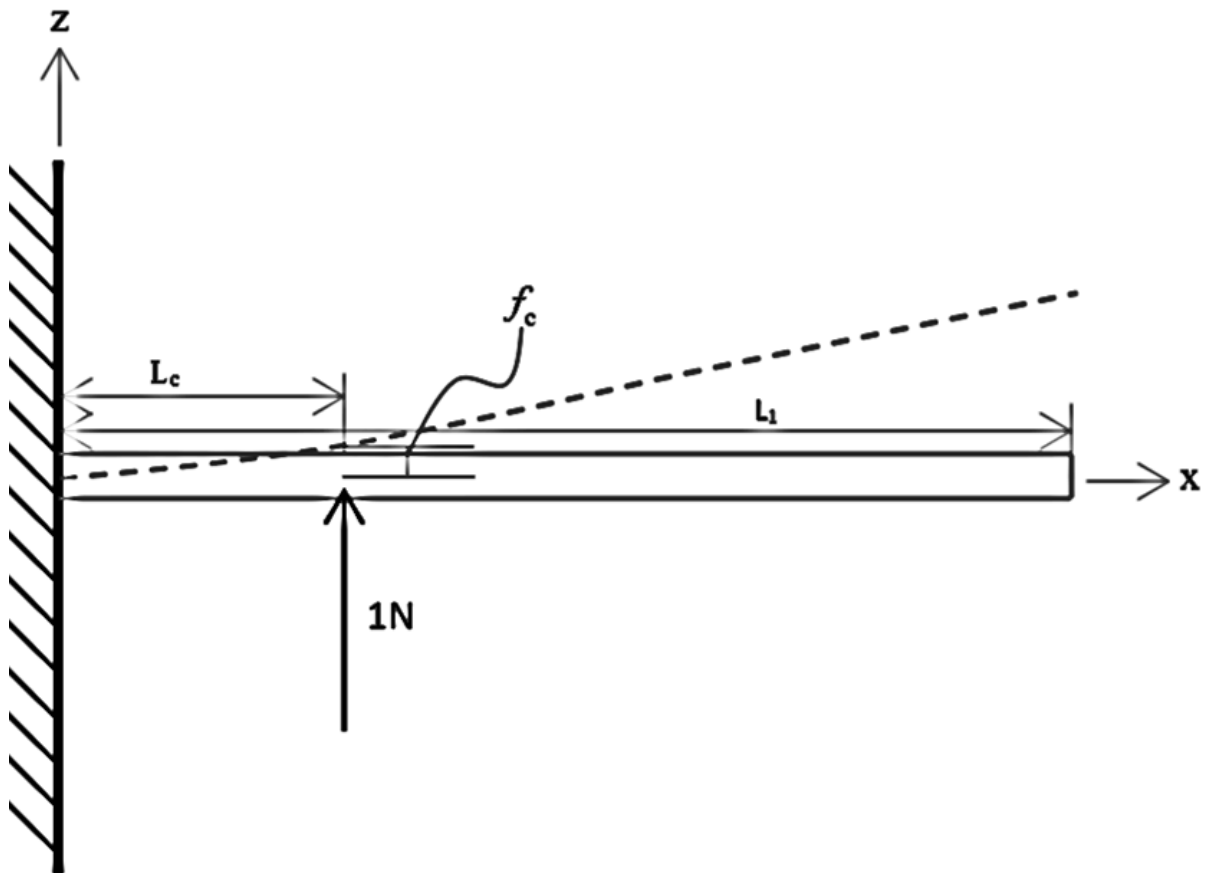


Figure 3-16 - Unit Force Method – Deflection due to Unit Force

The sum of the moments and forces give the reaction forces:

$$\sum M_o = 0 = -M_a + 1L_c \quad 3-31$$

$$\boxed{M_a = L_c} \quad 3-32$$

$$\sum F_z = 0 = 1 + R_z \quad 3-33$$

$$\boxed{R_z = -1} \quad 3-34$$

Again, the Macaulay method can be used to determine the deflection:

$$EI \frac{d^2 f_c}{dx^2} = M(x) = 1\langle x - L_c \rangle + x + L_c \quad 3-35$$

$$EI \frac{df_c}{dx} = \frac{1\langle x - L_c \rangle^2}{2} + \frac{x^2}{2} + L_c x + C_1 \quad 3-36$$

$$EI f_c = \frac{1\langle x - L_c \rangle^3}{6} + \frac{x^3}{6} + \frac{L_c x^2}{2} + C_1 x + C_2 \quad 3-37$$

Since it is a fixed beam, the following boundary conditions can be used to determine the constants of integration:

$$f_c = 0 \text{ at } x = 0 \quad \frac{df_c}{dx} = 0 \text{ at } x = 0$$

Therefore, $C_1 = 0$, $C_2 = 0$

This yields the deflection per unit force of:

$$f_c = \frac{1\langle x - L_c \rangle^3}{6EI} + \frac{x^3}{6EI} + \frac{L_c x^2}{2EI} \quad 3-38$$

At location L_c , this becomes:

$$f_c = \frac{L_c^3}{6EI} + \frac{L_c^3}{2EI} = \frac{2L_c^3}{3EI} \quad 3-39$$

Both deflection values have been determined as a function of truss position, pipe geometry, and material properties. Substituting the two results into the original equation gives:

$$\begin{aligned} \Delta_c + f_c 2F_a &= \frac{2F_a L_c}{A_a E_a} \sin \beta \\ -\frac{m_1 g L_1 L_c^2}{4EI} - \frac{m_2 g L_1 L_c^2}{4EI} + \frac{m_1 g L_c^3}{6EI} + \frac{m_2 g L_c^3}{12EI} - \frac{m_1 g L_c^4}{12L_1 EI} + \frac{2F_a L_c^3}{3EI} &= \frac{2F_a L_c}{A_a E_a} \sin \beta \\ -\frac{m_1 g L_1 L_c^2}{4EI} - \frac{m_2 g L_1 L_c^2}{4EI} + \frac{m_1 g L_c^3}{6EI} + \frac{m_2 g L_c^3}{12EI} - \frac{m_1 g L_c^4}{12L_1 EI} &= 2F_a \left(\frac{L_c}{A_a E_a} \sin \beta - \frac{L_c^3}{3EI} \right) \end{aligned} \quad 3-40$$

The moment of inertia of the pipe will be much smaller than the cross-sectional area of the trusses. Because of this, the elongation component that was included is negligible, and can be ignored, simplifying the original equation. The original equation can be written as:

$$\Delta_c + f_c 2F_a = 0 \quad 3-41$$

Rearranging this to solve for F_a yields:

$$F_a = \frac{\left(-\frac{m_1 g L_1 L_c^2}{4EI} - \frac{m_2 g L_1 L_c^2}{4EI} + \frac{m_1 g L_c^3}{6EI} + \frac{m_2 g L_c^3}{12EI} - \frac{m_1 g L_c^4}{12L_1 EI} \right)}{\left(-\frac{4L_c^3}{3EI} \right)} \quad 3-42$$

With all reaction forces defined, the stress due to inertial forces can now be determined.

The x component stress due to the inertial loads can be expressed by:

$$\sigma_{x_{vert}} = \frac{My}{I} + \frac{q \cos \theta x}{A} \quad 3-43$$

To determine the bending moment, the equilibrium equations are first required.

$$\sum M_o = 0 = M_a - \frac{m_1 g L_1}{2} - \frac{m_2 g L_1}{2} + 2F_a L_c \quad 3-44$$

$$\boxed{M_a = \frac{m_1 g L_1}{2} + \frac{m_2 g L_1}{2} - 2F_a L_c} \quad 3-45$$

$$\sum F_z = 0 = 2F_a + R_z - m_1 g - \frac{m_2 g}{2} \quad 3-46$$

$$\boxed{R_z = m_1 g + \frac{m_2 g}{2} - 2F_a} \quad 3-47$$

Using the Macaulay method provides the moment equation as a function of x:

$$M(x) = \left(-\frac{m_1 g L_1}{2} - \frac{m_2 g L_1}{2} + 2F_a L_c \right) + \left(m_1 g + \frac{m_2 g}{2} - 2F_a \right) x + 2F_a \langle x - L_c \rangle - \frac{m_1 g}{2L_1} x^2 \quad 3-48$$

Substituting this into the stress equation gives:

$$\sigma_{x_{vert}} = \frac{\left(\left(-\frac{m_1gL_1}{2} - \frac{m_2gL_1}{2} + 2F_aL_c\right) + \left(m_1g + \frac{m_2g}{2} - 2F_a\right)x + 2F_a(x-L_c) - \frac{m_1g}{2L_1}x^2\right)z}{\frac{\pi}{4}\left(\left(\frac{d_o}{2}\right)^4 - \left(\frac{d_i}{2}\right)^4\right)} + \frac{q \cos \theta L_1}{2\pi\left(\left(\frac{d_o}{2}\right)^2 - \left(\frac{d_i}{2}\right)^2\right)} \quad 3-49$$

Looking at the bending moment diagram can help determine the location of maximum stress as a result of the inertial loads.

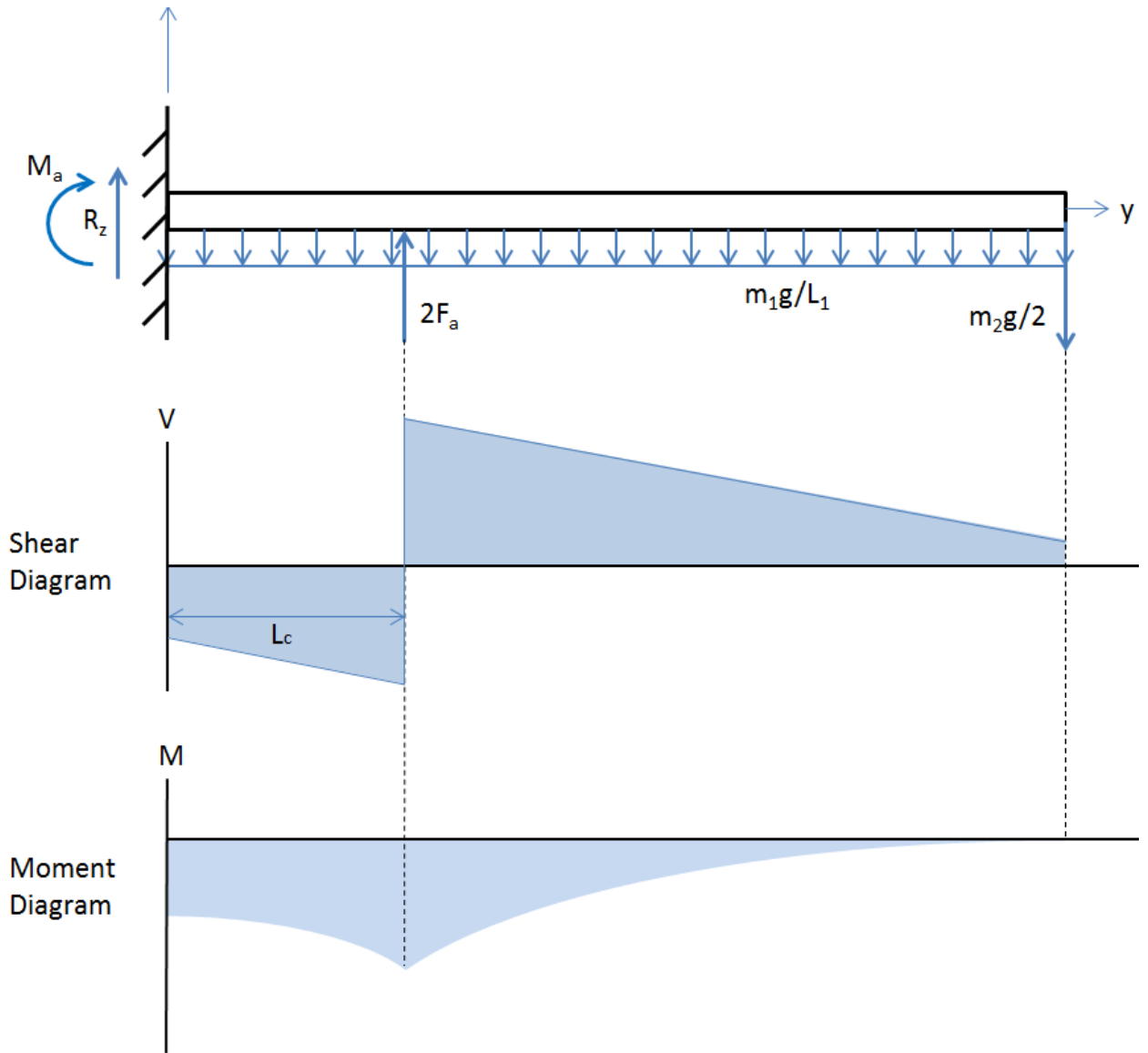


Figure 3-17 - Simplified Inertia Loading with Corresponding Shear and Moment
Diagrams

The bending moment diagram shows a maximum bending moment at the truss support connection, at $x = L_c$. The maximum bending stress is located on the outer edge of the pipe. The maximum stress at $x = 0$, and $z = (d_0/2)$ is given by:

$$\sigma_{x_{vert}} = \frac{\left(\frac{-m_1gL_1 - m_2gL_1 + 2F_aL_c}{2}\right)\left(\frac{d_o}{2}\right)}{\frac{\pi}{4}\left(\left(\frac{d_o}{2}\right)^4 - \left(\frac{d_i}{2}\right)^4\right)} + \frac{q \cos \theta}{2\pi\left(\left(\frac{d_o}{2}\right)^2 - \left(\frac{d_i}{2}\right)^2\right)} \quad 3-50$$

The shear stress due to the inertial loads is given by:

$$\tau_{vert} = \frac{VQ}{It} = \frac{4V}{3\pi} \left(\frac{r_o^2 + r_o r_i + r_i^2}{r_o^4 - r_i^4}\right) = \frac{4\left(\frac{3m_1g}{2} + 2m_2g + 2F_a\right)}{3\pi} \left(\frac{r_o^2 + r_o r_i + r_i^2}{r_o^4 - r_i^4}\right)$$

3-51

This shear stress is a maximum at the neutral axis. This will affect the stress at point A, and the shear from the wind loads will affect the stress at point B.

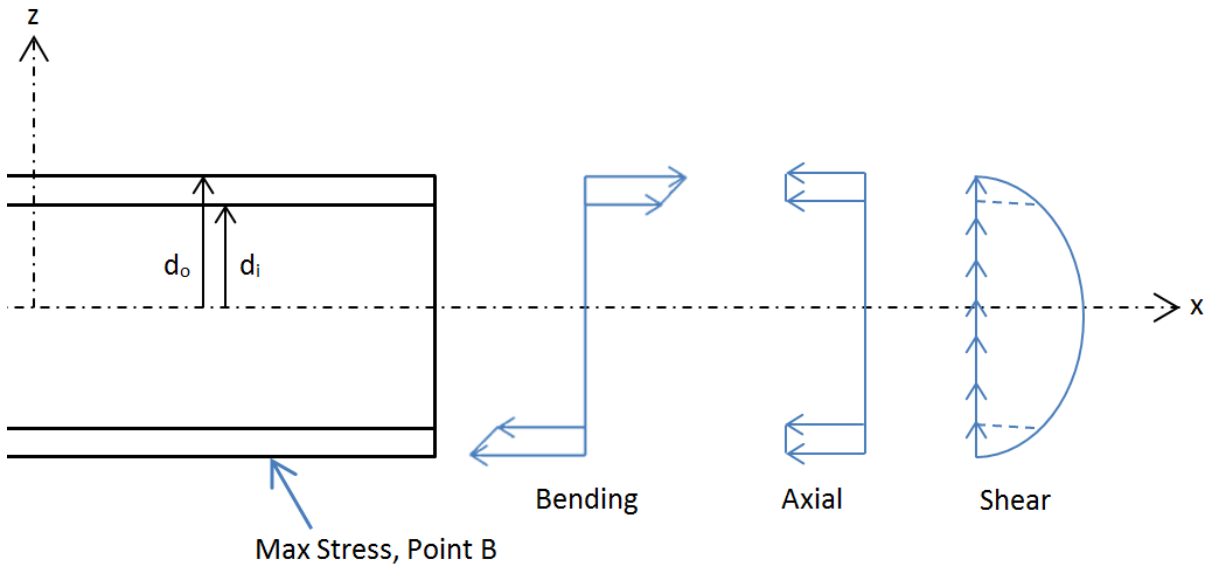


Figure 3-18 - Maximum Stress Conditions Resulting from Wind Load

The principal stress can be found using the following equation:

$$\sigma_1, \sigma_2 = \frac{\sigma_x + \sigma_z}{2} \pm \sqrt{\left(\frac{\sigma_x - \sigma_z}{2}\right)^2 + \tau_{horz}^2} \quad 3-52$$

The axial loads in the system must also be considered, as it can lead to buckling. The overall buckling of a pinned-roller supported beam will occur at a certain critical load, defined as:

$$P_{cr} = \frac{\pi^2 EI}{L_1^2} \quad 3-53$$

The axial load must not exceed the critical buckling load. It is likely that the axial load will be much smaller, but the value should be checked once the axial load is determined.

Three stress points will be considered when the stress calculations are carried out. Point A is located at the center of the boom, and represents the maximum stress point due to the wind load. Point B is located at the base of the boom, and point C is located at the vertical support truss connection point. Point B and C both consider the vertical inertial loads on the main boom. Figure 3-19 shows this representation.

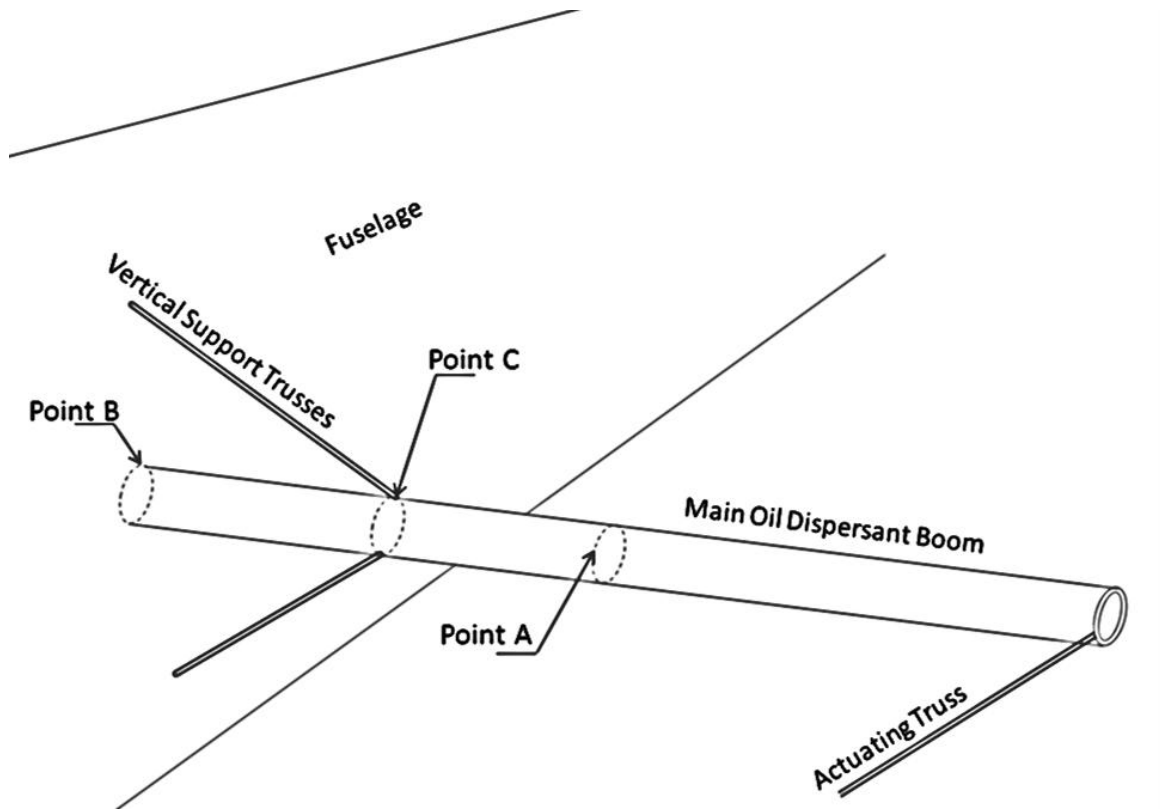


Figure 3-19 - Representation of Critical Stress Points

3.5. Wind Loads

As discussed in the literature review, there are two primary types of analytical methods used for this type of aerodynamics problem. Potential flow theory and empirical test data are commonly used to calculate lift, drag, and pressure distribution. However, potential flow theory fails as a result of D'Alembert's Paradox, where the results predict zero drag for a body in a constant velocity flow, when it is known that drag exists [47]. This primarily results from the neglected effects of viscosity in potential flow theory. Friction drag and boundary flow separation cannot be predicted using this method, and therefore

fails in the case of a cylinder in high Reynolds flow. Because of this, it was determined that focusing on empirical data will suffice for this application.

Empirical data has been compiled for many thousands of shapes by testing them in wind tunnels. The data provided is usually non-dimensional, and can be applied to any scale. The data is presented as a factor of Reynolds number, angle of attack, or comparing coefficients of drag, lift and pressure. In the case of a cylinder, the coefficient of drag is given as a function of the Reynolds number.

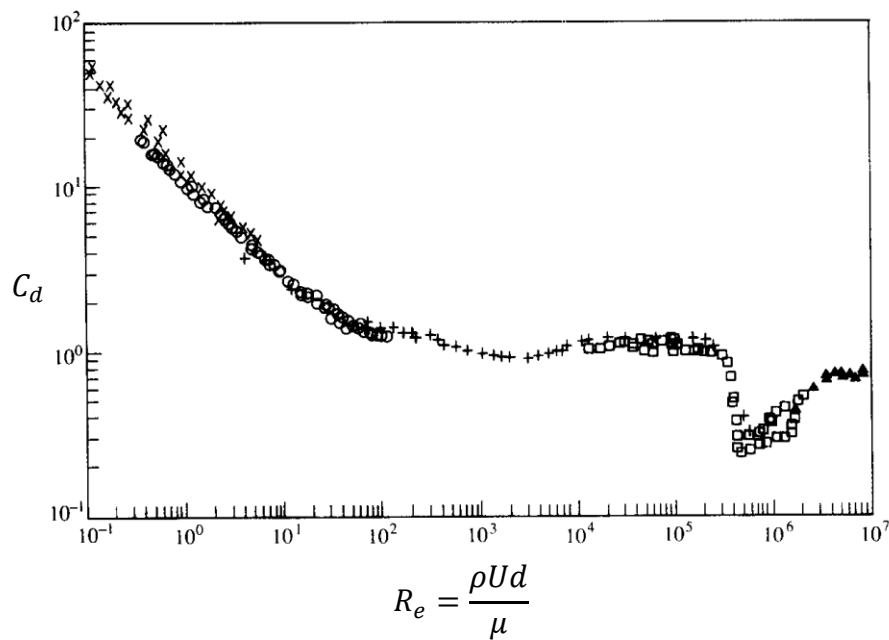


Figure 3-20 - Drag Coefficient of a Cylinder [48]

The results come from a series of wind tunnel testing. The coefficient of drag can be determined based on the flow properties. The Reynolds equation is the same as the internal pipe seen earlier, but some of the parameters are defined differently:

$$R_e = \frac{\rho U d}{\mu} \quad 3-54$$

Fluid density is ρ , U is external flow speed, d is the characteristic length travelled by the fluid (diameter for a cylinder, chord length for an airfoil), and μ is dynamic viscosity. This introduces several new parameters which can be determined based on the previously stated conditions. Standard fluid density and dynamic viscosity at a standard spray altitude for a Dash 8 Q300 was used. The maximum design speed of 146.67 m/s for a Dash 8 Q300 was used for the fluid velocity.

Once a drag coefficient is determined from empirical data, some simple equation manipulation can yield a drag force equation. The coefficient of drag is:

$$C_d = \frac{2F_d}{\rho v^2 A_f} \quad 3-55$$

Where ρ is the fluid density, v is the kinematic viscosity, A_f is the reference area (frontal area), and F_d is the drag force. Manipulating this equation gives the drag force equation:

$$F_d = \frac{C_d \rho_a v^2 A_f}{2} \quad 3-56$$

This simple formula can then be used to calculate the drag force on an object. The wind load is distributed over the length of the boom, and can be expressed as:

$$q = \frac{C_d \rho_a v^2 A_f}{2L_1} \quad 3-57$$

As the deployable boom extends, the cross-section parallel with the wind flow direction will change. The overall frontal area will also change, changing the drag value as the boom angle changes. However, for the sake of simplicity, the drag will be set as a function of the boom angle. As the boom stows, the drag forces should greatly decrease. The equation $q \sin \theta$ provides an approximate value for the changing drag force. As the angle θ reaches zero, the drag force reaches zero.

3.6. Material Selection

Material selection is a key step in the preliminary design process. In order to choose the remaining design parameters, material properties must be chosen. Each material will be ranked based on benefits and concerns around each material, and the impact each material has on the thickness of the pipe.

In order to keep the design versatile, the material properties which are most desirable must be defined. In this scenario, the system is located outside of the aircraft, and is exposed to extreme wind loads, icing conditions, and highly corrosive ocean air. The pipe must carry a particularly reactive chemical such as COREXIT. These factors suggest a need for corrosion resistance in the material. An aircraft platform application also suggests that the weight must be kept to a minimum, for performance considerations.

Material selection will be limited to common materials used in the aerospace industry. Using materials familiar to the industry allows for purchasing from existing vendors, and

will guarantee that normal manufacturing methods can be used. Further, these materials are proven to work specifically for the conditions experienced by aircraft.

The material selection for the main boom will first be considered. Aluminum alloys are the most commonly used materials used in the aircraft industry, such as Aluminum 2024-T3, Aluminum 6061-T6, and Aluminum 7075 [49]. Stainless steel is not often used in aircraft applications, other than moving hydraulic fluid, but will be considered here.

Table 3-2 - Material Properties

Material	Material Properties
Aluminum 2024-T3	<p>Poor corrosion resistance, good machinability, high strength, commonly used for aircraft fittings and internal structural applications [50].</p> <p>Density: 2780 kg/m³</p> <p>Elastic Modulus: 73 GPa</p> <p>Yield Strength: 345 MPa</p>
Aluminum 6061-T6	<p>Excellent corrosion resistance, good strength. Often used in aircraft, hydraulics, and marine applications [51].</p> <p>Density: 2700 kg/m³</p> <p>Elastic Modulus: 68.9 GPa</p> <p>Yield Strength: 276 MPa</p>
Aluminum 7075-T6	<p>Very high strength, expensive, corrosion resistance not a strong feature [51].</p> <p>Density: 2810 kg/m³</p> <p>Elastic Modulus: 71.7 GPa</p> <p>Yield Strength: 503 MPa</p>
Stainless Steel	<p>Very good corrosion resistance, low strength, possible metal compatibility issues due to galvanic corrosion, much heavier than aluminum options [51].</p> <p>Density: 8000 kg/m³</p> <p>Elastic Modulus: 200 GPa</p> <p>Yield Strength: 217 MPa</p>

With material properties defined, the boom pipe thickness can be determined using the stress equations defined earlier. A safety factor commonly used in the aircraft industry is 1.1, and will be used in this application. It is an approximation for the limit of proportionality. With this information, the unknown pipe thickness can be determined.

An Excel spreadsheet was used to calculate the minimum allowable pipe thickness using an iterative process. A series of stages of the calculations lead to a calculated maximum stress in the system. This stress is compared with the yield strength of the material. The pipe thickness is modified through an iterative process to reach the allowable stress. This iterative process provides a quick way of determining the minimum allowable thickness without complicated equation manipulation.

Figure 3-21 below shows the iterative process to find the minimum allowable thickness of the pipe.

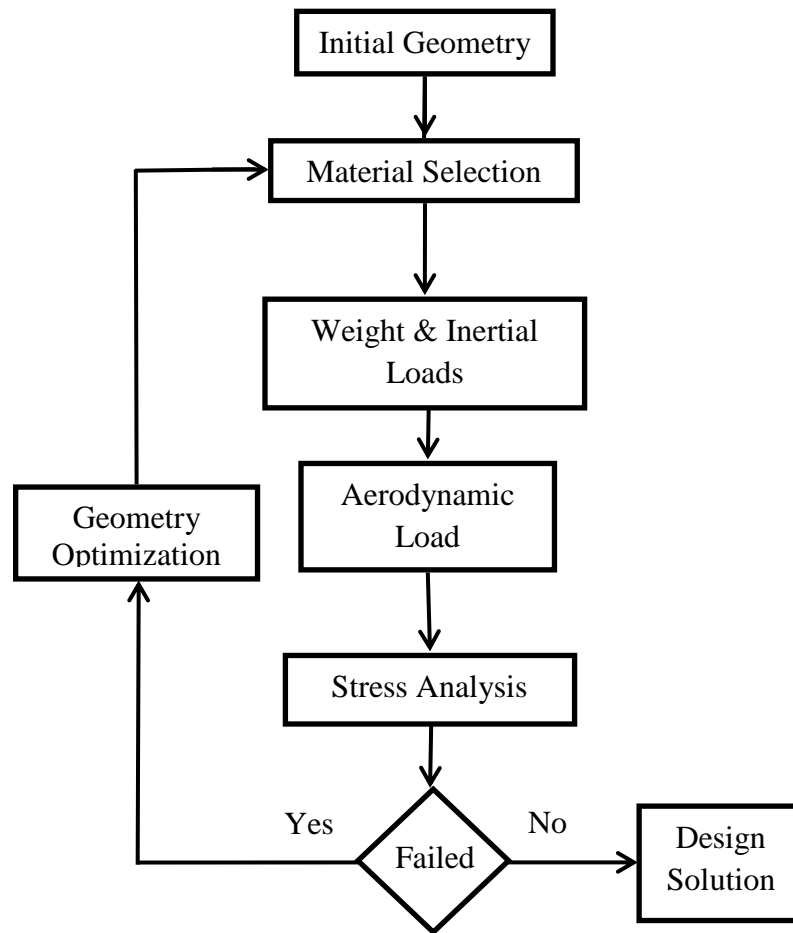
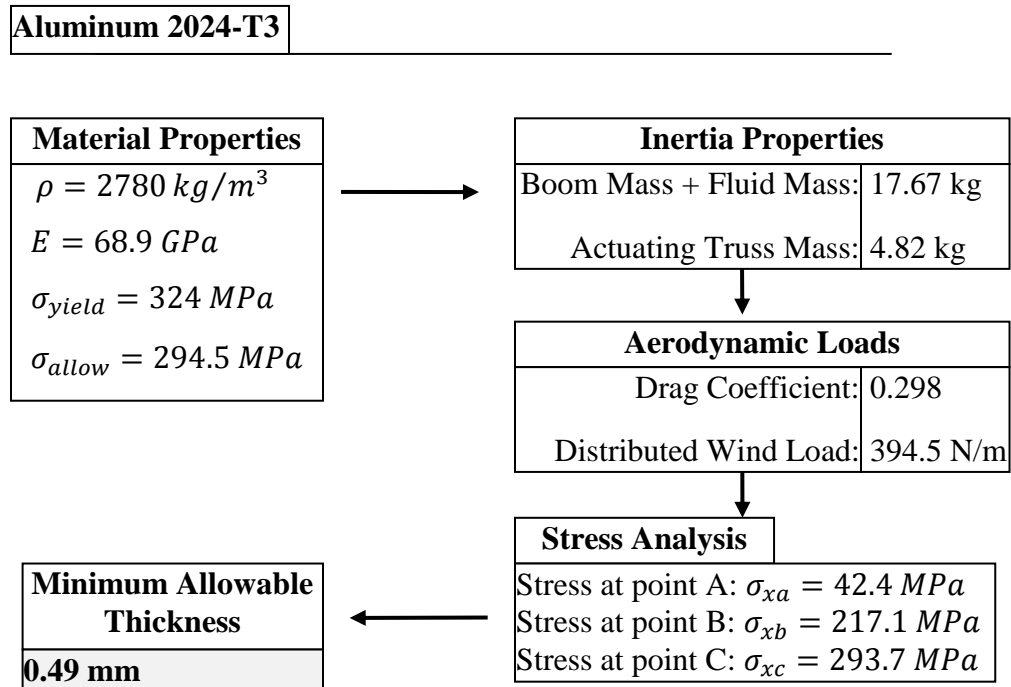


Figure 3-21 - Parametric Design Process

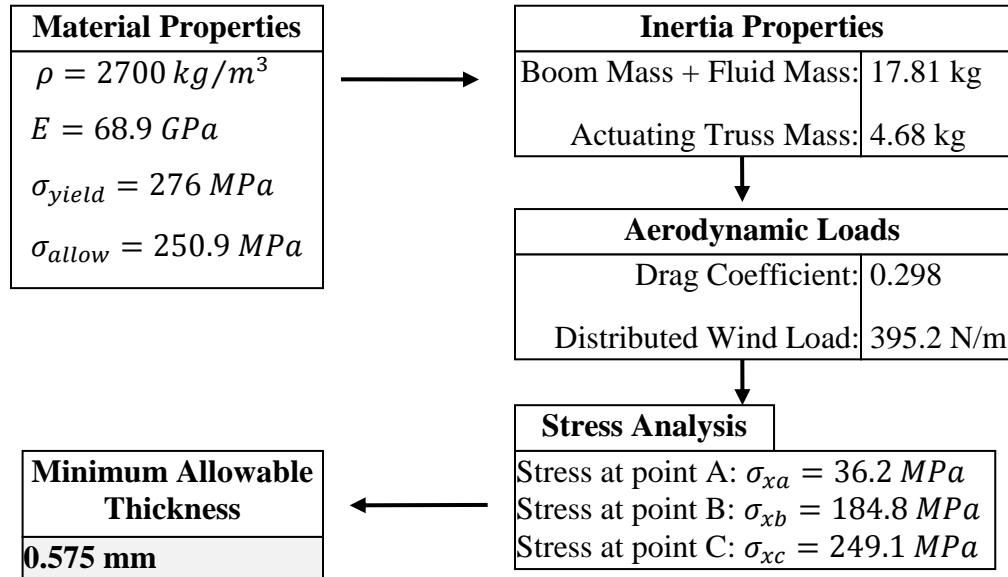
This process was carried out for each material choice listed in Table 3-3. For this stage, some truss property assumptions such as material and diameter were made, to continue with the calculations. Once a preliminary design is decided on, the details of the truss properties can be refined. The actuating truss was calculated using the same material as the boom, with a diameter of 4 cm. The two vertical supporting trusses have a diameter of 3 cm, and the location L_c of the connection with the boom is 0.6 meters. The axial force

required for buckling to occur in the vertical support trusses is approximately 140 kN, which is approximately over 85 times higher than the expected axial loading. The buckling load of the actuating truss has a much lower buckling load, also a much lower maximum applied load. It has a buckling load of approximately 4500N, which is roughly 10 times higher than the expected maximum wind load applied. With the truss values defined, the boom properties can be determined. Each material will be listed, along with the determined minimum allowable thickness, calculated stresses, and other loads.

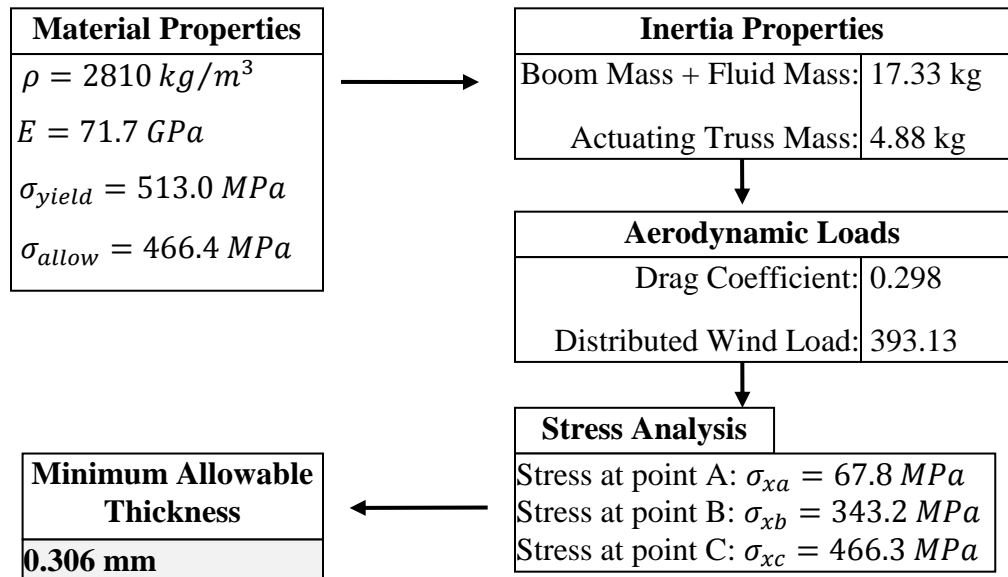
Table 3-3 - Analysis Results – Material Selection

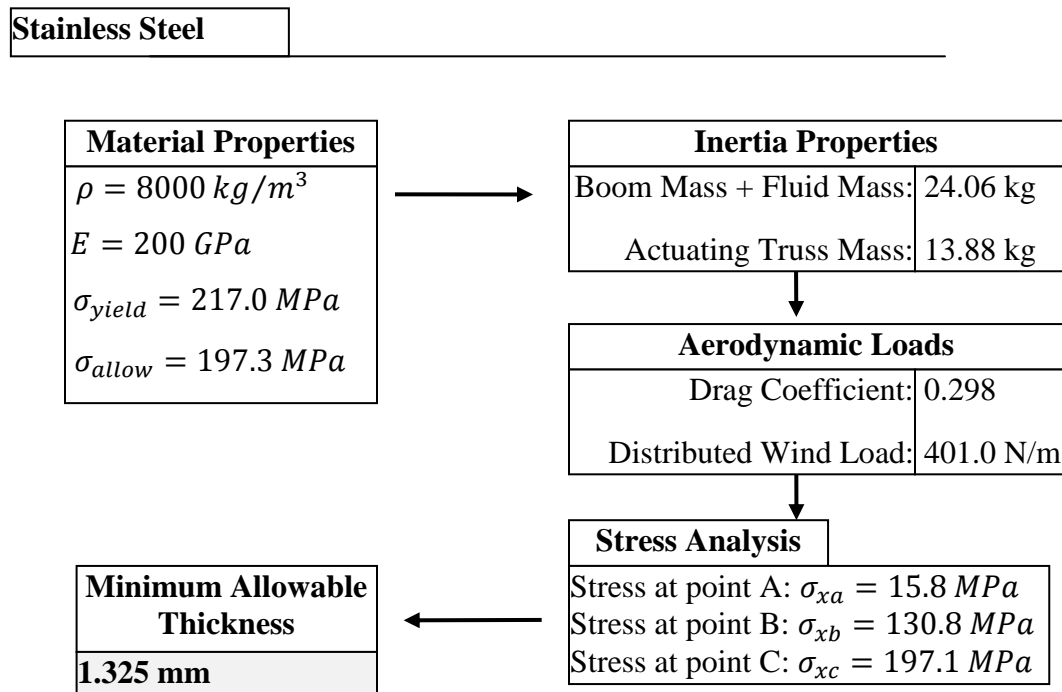


Aluminum 6061-T6



Aluminum 7075-T6



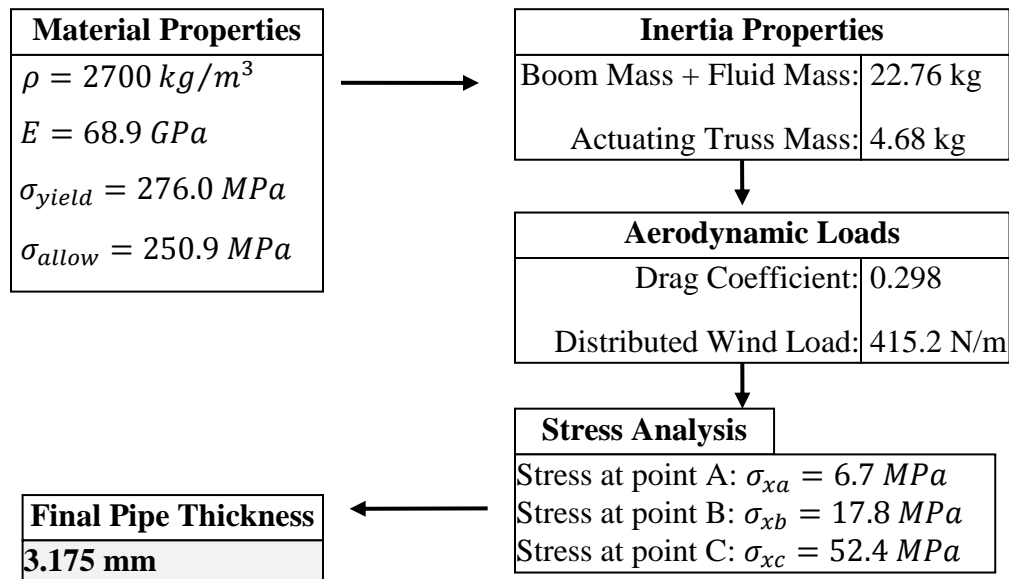


It was noted that the shear stress resulting from the aerodynamic load had a negligible effect on the critical principal stress at point C. Shear from the aerodynamic load increased the principal stress by 0.045% at point C. The principal stress at point B increased by 0.41% as a result of the aerodynamic load. Therefore, the stress at point C resulting from the bending stress was considered when determining the minimum allowable thickness. The results from the calculations above show that the minimum total weight and pipe thickness was achieved by the Aluminum 7075-T6. Comparing all four materials, the thicknesses are all much smaller than typical manufactured pipe thicknesses. Therefore, material choice can be based solely on preferred material properties such as corrosion resistance. The material chosen for this application is Aluminum 6061-T6. This material is commonly used in the aerospace industry for its

excellent corrosion resistance, and light weight. A standard pipe thickness of 3.175 mm (1/4") is chosen, giving a final safety factor of 4.8. The preliminary design parameters determined using the parametric study is outlined in Table 3-4.

Table 3-4 - Preliminary Design Summary

Preliminary Design Parameters



3.7. Conclusion

The parametric design has allowed for a preliminary design that can be quickly updated as design conditions and requirements change. A preliminary design based in analytical techniques provides a conservative solution to the expected design loads and internal stresses. The next step is analyze this preliminary design using computational methods to

seek realistic and accurate loads and hence stresses in the system. This will allow for an optimized design, lowering the weight, and identifying areas of stress concentration.

4. Detailed Static Analysis

The preliminary design has been defined using a series of standard analytical techniques guided by a parametric design method. This sets the stage for further analysis to understand the system under complex loading conditions. The detailed static analysis will be broken into two primary analysis sections. The first will consider the wind load conditions discussed in section 3.5, and will seek to verify and improve on those results using Computational Fluid Dynamics (CFD). The second section will consider the general loading scenario of the system as a whole, and observe the resulting stresses on a localized scale using Finite Element Analysis (FEA). FEA will be used to verify the results of the preliminary design chapter, as well as consider more in-depth design problems. The goal of these two detailed analysis sections is to optimize the preliminary design, provide more confidence in the previous analysis through verification of results, and to provide a more realistic view of the loading conditions.

4.1. Wind Loads

In section 3.5, the wind loads were determined using empirical values generated from wind tunnel testing. A simple cylinder in cross flow was considered. The results of this cylinder directly perpendicular to the flow are highly accurate and can be trusted. However, the empirical results only provide a resultant overall load. The pressure distribution is not provided by this method. This pressure distribution is important for the detailed structural analysis simulation carried out in FEA, and can be determined through CFD. Further, the accuracy of the approximated aerodynamic load can be verified using

CFD. Since the fully deployed oil dispersant system at an angle to the flow, the empirical results for the cylinder fully perpendicular to the cross flow were scaled by multiplying the wind load value by the sine of the angle of the boom. When the boom is fully stowed, the wind load value moves toward zero, as would be expected in reality. This approximation was deemed accurate enough for the application, but it is important to note that this approximation does lack accuracy. The goal of this section is to improve the accuracy of this result, and consider a more complex problem that would not be possible using empirical techniques.

To solve this complex problem, ABAQUS Computational Fluid Dynamics solver was used in this case, but there are many other programs for this application. As in any engineering problem, the ABAQUS results need a benchmark to ensure the correct settings and simulation set-up are being used. This was accomplished by modelling the simple cylinder perpendicular to the flow, under the same parameters used previously. The following parameters were used in defining the aerodynamics problem.

Table 4-1 - Computational Fluid Dynamics Properties

Property	Value
Air Density	1.2 kg/m ³
Dynamic Viscosity	1.488E-2 mPa.s
Fluid Velocity	146.667 m/s
Element Type	Wedge

A fluid domain was created using a block with dimensions of 1 m x 2.1336 m x 0.5 m. A cylinder of radius 0.0540 m was removed from the fluid domain, and will later be used to represent the outer surface of the main boom. Using the parameters given in Table 4-1, a mesh dividing the main boom into 16 surface elements was used. A structured hex element FC3D8 was used for the mesh generation in all cases. Figure 4-1 shows the pressure distribution shown from the side.

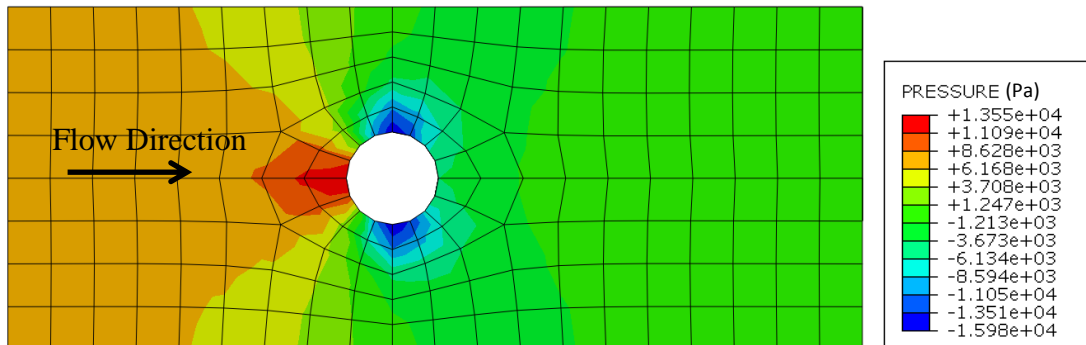


Figure 4-1 - CFD Simulation - 16 Elements

Looking at the pressure distribution in the 16 element model, it becomes clear that many of the pressure values on opposing sides of the cylinder cancel each other out. However, the pressure on the side of the cylinder facing the wind has a greatly increased pressure. It is roughly these pressures that provide the overall resultant force on the cylinder. The overall pressure map can be seen on the length of the cylinder in Figure 4-2.

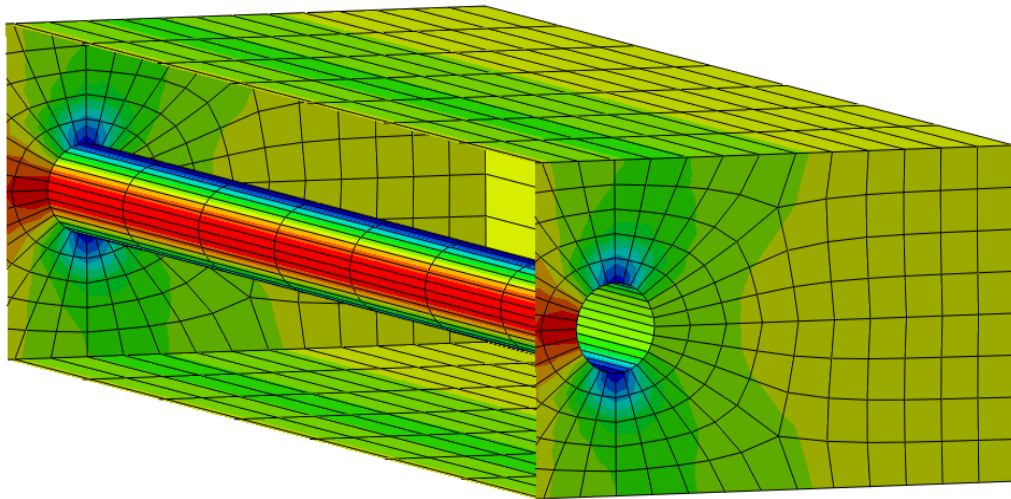


Figure 4-2 - Pressure Map Across Main Boom due to Wind Load

In order to estimate the resultant force and compare with the empirical values, this pressure map must be analyzed. The pressure at a particular node can be determined from the output file, and using a series of points, the force per unit length can be determined. In order to keep the verification simplified, the main points associated with the identified region of interest on the front of the pipe will be used. At each cross-section along the length of the pipe, the pressure values at the associated nodes are averaged to find an overall pressure being applied to the front of the pipe. The resultant pressure parallel to

the flow direction is then multiplied by the arc length between the nodes used. This pressure multiplied by the arc length gives a force per unit length, written as:

$$P_{avg}L_{arc} = q \quad 4-1$$

For the 16 element case, the arc length was determined based on how many nodes were used, and the length of arc between each node. Three nodes were used, covering two out of 16 segments around the circumference of the pipe.

$$L_{arc} = \frac{2}{16} 2\pi r = \frac{1}{4} \pi (0.053975 \text{ m}) = 0.0424 \text{ m} \quad 4-2$$

ABAQUS visualization tab allows for the output of specific nodal pressure values. Figure 4-3 shows the selection of the appropriate nodes.

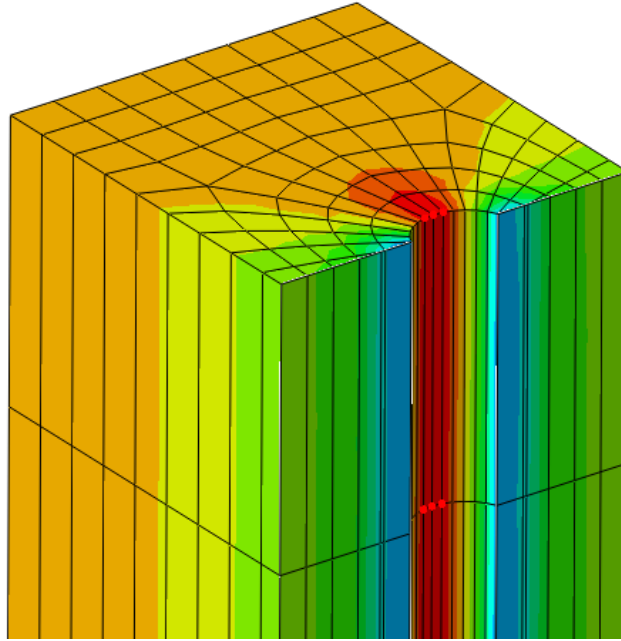


Figure 4-3 - Node Selection for Pressure Output Data

Three points at each cross-section were averaged, and multiplied by the arc length. All of these values were then averaged for an overall distributed force. A mesh density using 8 elements around the pipe to simulate the cylinder in a cross flow. The 8-element pressure map result can be seen in Figure 4-4.

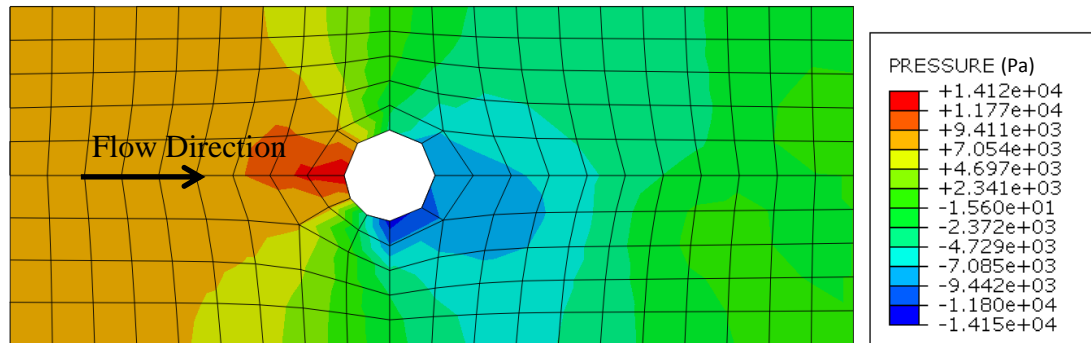
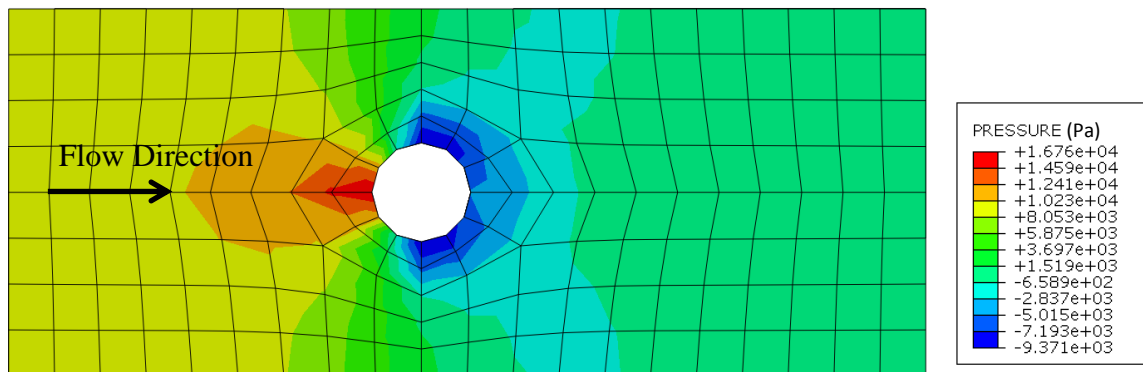


Figure 4-4 - CFD Simulation - 8 Elements

The 8-element mesh had a result of 812 N/m. This is a 95% difference from the 415 N/m empirical results. In an attempt to alleviate this disparity, a mesh convergence study was conducted. This was done by increasing the mesh density in increments.

A mesh density using 8 elements around the pipe to simulate the cylinder in a cross flow.

The 12-element pressure map result can be seen in



The 12-element mesh had a result of 750 N/m. This is a 81% difference from the 415 N/m empirical results.

For the 16 element case, the resulting distributed force was found to be 492 N/m, again beyond acceptable margins from the value of 415 N/m found using empirical data, a 19% relative error. A 24 element mesh produced improved results, resulting in a distributed force of 469 N/m, representing a relative error of 13%. Next, a 32-element mesh was tested to observe any improvements in the result. Figure 4-5 shows the 32-element pressure map result.

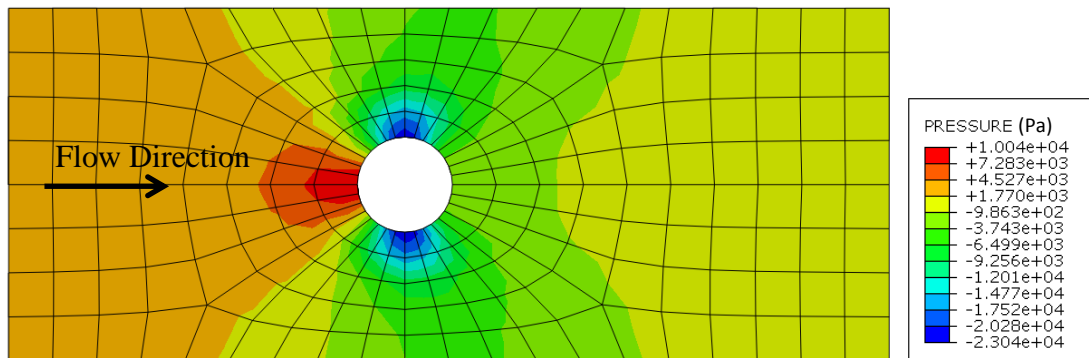


Figure 4-5 – CFD Simulation - 32-Elements

The 32-element mesh had a result of 434 N/m. This is a 5% difference, significantly reduced from the 95% difference seen previously. Finally, a 64-element mesh was tested, showing adequate results. Figure Figure 4-6 shows the pressure map results of the 64-element mesh.

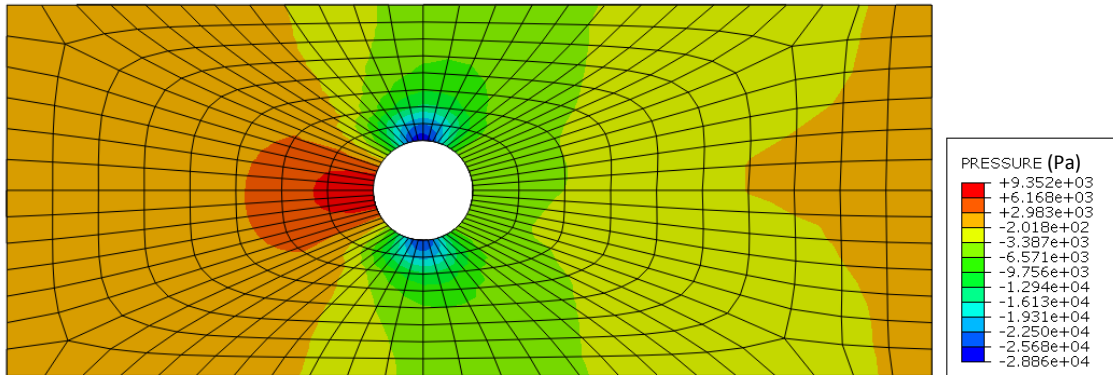


Figure 4-6 - CFD Simulation - 64 elements

Figure 4-7 shows the result of the mesh convergence study, showing good convergence toward the empirical solution for a greater mesh density.

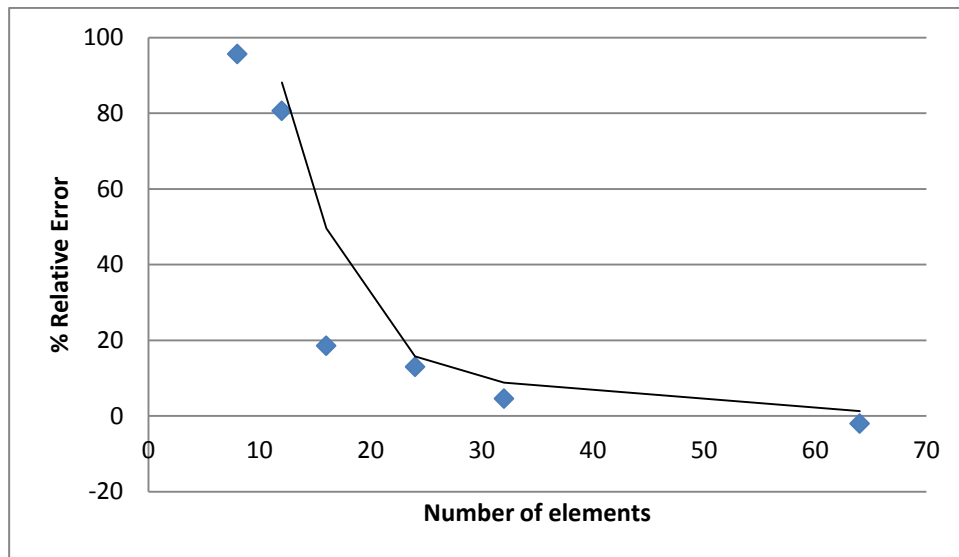


Figure 4-7 - Mesh Density Study

The results are within acceptable margins, and even higher mesh densities should yield the same result as the empirical data. A structured mesh can also be considered when

seeking higher accuracy. The next step is to consider the boom at an angle, and compare the results with the approximated solution. As mentioned previously, the fully deployed boom will never reach the fully perpendicular position used in the empirical calculations. It will reach an angle of 49° to the body of the plane. To simulate this using the existing empirical result, it was multiplied by the sine of that angle, scaling the result to approximate the actual solution. However, it is known that the shape of the cross-section seen by the air flow will not be a simple circle as before, but an ellipse. This can be simulated using CFD as before, except with a resultant wind speed of 146.67 m/s approaching the boom at an angle of 49° . The same simulation parameters were used as before. Figure 4-8 shows the pressure map of the angled input flow.

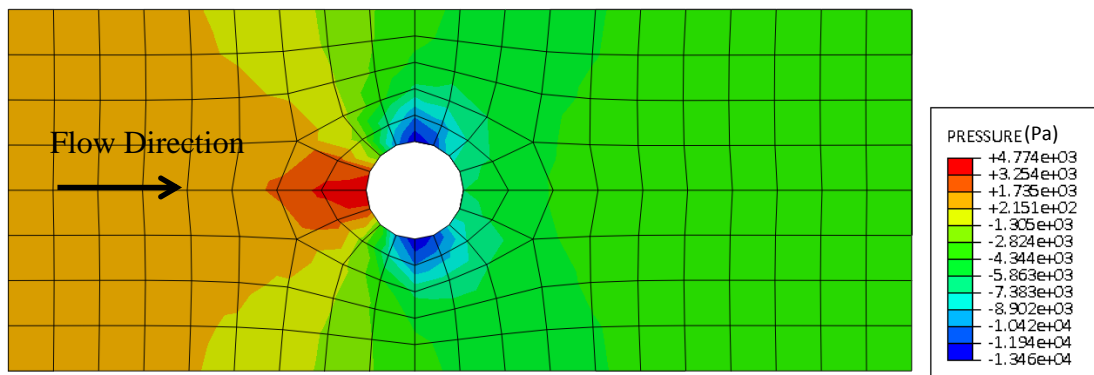


Figure 4-8 - CFD Simulation, Angled Flow - 16 Elements

The estimated result using the empirical result was $415 * \sin(49^\circ) = 314 \text{ N/m}$. The result from the CFD simulation was 206 N/m. This shows accuracy of results within 34%. The estimated result is highly conservative. To ensure accuracy of simulation results, a mesh density of 32 elements was used. This mesh density resulted in a much better

correlation with previous results. Figure 4-9 shows the pressure distribution map for the 32 element case.

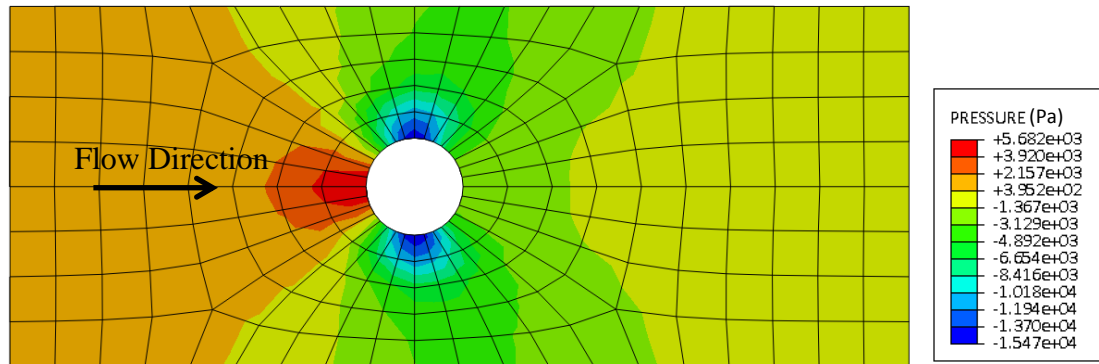


Figure 4-9 - CFD Simulation, Angled Flow - 32 Elements

The result from this simulation was found to be 214 N/m. This is 32% below the empirical result. Again, it shows the estimate was highly conservative. Even with the highly conservative estimate, the wind load had almost no effect on the critical stress. However, this result can be used to more accurately portray the actual response of the system to the aerodynamic load.

With a better understanding of the aerodynamic load on the main boom, more advanced static analysis can be carried out. This pressure distribution map can be applied to the Finite Element Analysis, providing a better understanding of the fluid structure interaction. Once the detailed design is complete, further CFD can be carried out to determine an overall drag created by the system.

4.2. Advanced Static Analysis

In section 3.6 in the Preliminary Design chapter, the majority of the stress analysis was carried out. In this analysis, the stress was found at three points along the oil dispersant boom. The loading scenario was for a worst case scenario, with a fully loaded and fully extended boom. As discussed previously, a realistic loading value of 3.5 to 6 times gravity is the realistic range for any aircraft component. However, as instructed by the industry partner, a loading of 10 times gravity was used. Aluminum 6061-T6 was chosen, yielding a minimum allowable pipe thickness of 0.575 mm. However, a nominal pipe thickness was chosen for availability, at 3.175 mm (1/8"). The stresses created for these specifications show a comfortable safety factor of approximately 4.8 for a maximum loading scenario. This analytical technique is the standard practice used in simple to moderate stress problems in the industry today, and is highly trusted. Accuracy is often sacrificed by reducing the complexity of the problem, in order to make it possible to solve the problem. Because of this, significant safety factors are often applied to ensure that reduced accuracy does not affect safety. However, it leads to a design that is not optimized. In recent years, advanced computational techniques have become very popular for solving such problems. FEA has grown rapidly in parallel with substantial improvements in computing power, and can solve very complex problems without a reduction in complexity. FEA can serve many purposes in the design process of the deployable oil dispersant system. The full system can be modelled, including the vertical truss supports, and actuating truss. Local effects of loading can be observed using 3D

models of the system, which can aid in the detailed design of the system. ABAQUS will be the FEA platform used in this application.

As with any Finite Element model, it is important to begin with a simple problem, and build the complexity once there is confidence in the results. A strong foundation provides confidence in the results as the model is developed beyond the simplified framework. A simple problem also provides an opportunity to ensure the basic finite element model properties are defined correctly. If an error in the simulation arises, it can be very difficult to identify the issue if the modeling began at an advanced stage. Properties such as material property definition, boundary conditions, load application, and element types must be fully understood in the context of the problem before it can be developed further.

The first step is to model the simplified solution seen in Chapter 3. The vertical load was considered to be the critical load as it was significantly higher than the wind load experienced at maximum flight speed. The vertical support trusses created a complicated indeterminate beam, and the unit force method was used to determine the stress. This meant the vertical support trusses were replaced by a force F_a to create an approximation of the beam deformation and stress. The FEA model will represent this case using a simple wireframe representation. The model will use a cantilever beam with force F_a applied at point C, and the same end load applied from the actuating truss. For the aluminum 6061-T6 pipe of 3.175 mm (1/8") thickness, the F_a force was determined to be 1507 N (two trusses having a combined loading of 3014 N). The end load due to the lumped mass fraction of the actuating truss was said to be 237 N. The total mass of the

boom including the oil dispersant chemical inside was said to be 23 kg, experiencing 10 times gravity. The analytical solution of the stress yielded 52.4 MPa at point C, and 40.3 MPa at point B. Figure 4-10 shows the wireframe model with loading and boundary conditions applied.

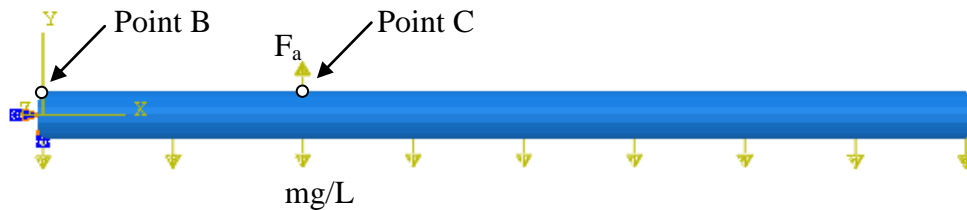


Figure 4-10 - Basic Wireframe Model with Force F_a

A mesh of 107 B32 quadratic elements was used, and the simulation was performed.

Figure 4-11 shows the stress contours present in the model.

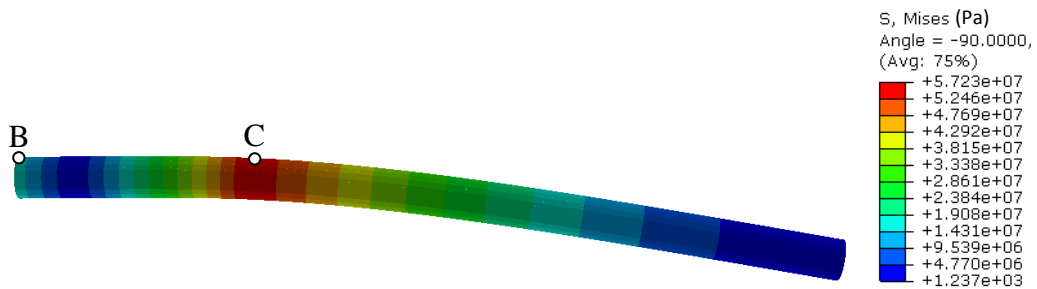


Figure 4-11 – Basic Wireframe Simulation Result – Stress Contour

The maximum stress is located at the point of applied load F_a . The stress at this point was found to be 52.7 MPa, closely matching the 52.4 MPa results from the analytical solution, with an error of 0.6%. The stress at the base of the boom, point B, was found to be 39.4

MPa, which also closely matched the 40.3 MPa result from the analytical solution, with an error of 2%. This cantilever model is a very simple problem for a finite element analysis simulation, and provides confidence in both the set-up of the model, and that the analytical solution for the stress under this loading scenario is correct. The next step is to validate the approximated load F_a . To achieve this, the model will now include the two vertical support trusses, with the stresses at point B and C used to compare. Figure 4-12 shows the model including the support trusses.

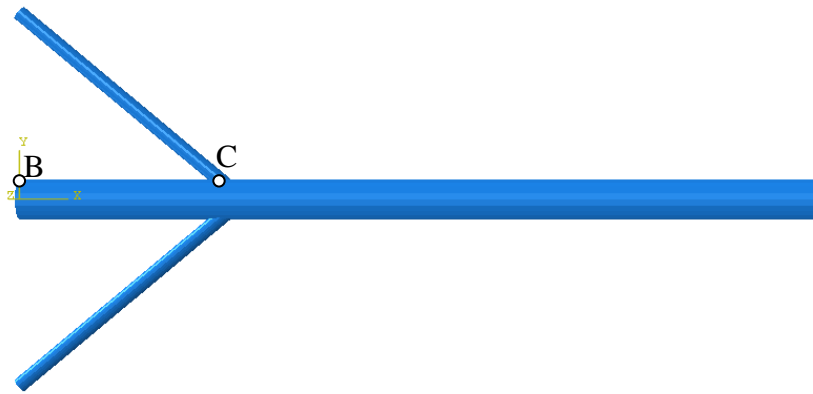


Figure 4-12 - Basic Wireframe Model Including Vertical Truss

The model was meshed using 185 B32 quadratic elements, similar to before. The base connection of each vertical support truss was also treated as fixed to any motion in the x, y, and z planes, and rotation restricted around the z-axis. Figure 4-13 shows the stress contour of the oil dispersant boom with vertical support trusses.

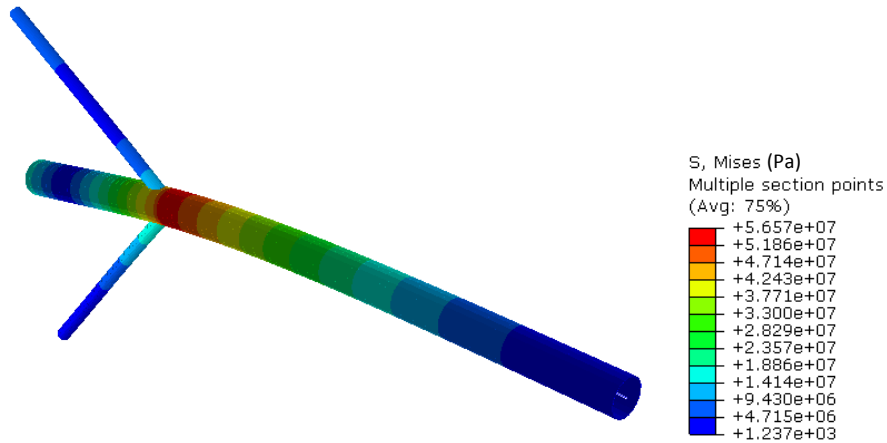


Figure 4-13 - Wireframe with Vertical Support - Stress Contour

The stress at point C, located at the point of contact with the vertical support trusses was found to have a stress of 54.3 MPa, very close to the results from the previous case and the analytical solution, with an error of 3.6%. However, the stress at the base of the boom at point B differed significantly. The stress at point B was found to be 17.8 MPa, more than half of the stress value seen in both previous cases. The goal now is to determine the correct value of F_a that will reproduce the exact results seen in the simulation results when the vertical truss supports were included. Testing several values for the approximated vertical support truss force F_a yielded a final result of 2000 N (4000 N total). This is approximately 33% higher than the estimated value. Although there is a significant difference, it turns out that the critical stress around the vertical support connection is virtually the same. It remains the critical stress point, and yields the same conclusion despite the highly improved accuracy of the solution. The greatly decreased stress located at the base of the boom will be significant for the design of the base

connection to the body of the aircraft, but it is important to note that the less accurate analytical solution was conservative in this instance.

To this point, the vertical and horizontal loading has been separated for the sake of simplicity. Since the inertial load and wind load are out of plane from each other, the only direct effects on the critical stress will be from shear stress. To accomplish this, a line load was used to represent the wind load. A total wind load of 314 N/m was used for the distributed load along the length of the boom. Figure 4-14 shows the resulting stress contour for the boom under a wind load.

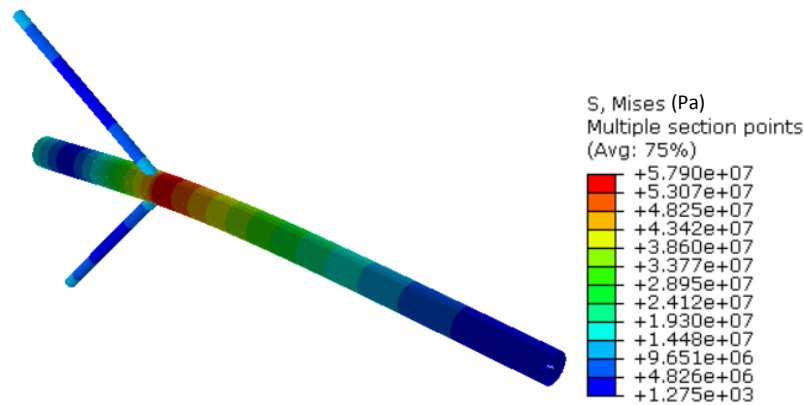


Figure 4-14 - Wireframe Model with Aerodynamic Load - Stress Contour

The stress at point A, where the vertical support trusses attach to the main boom, the stress was found to be 54.6 MPa. The stress at point B, located at the base of the boom, was found to be 17.9 MPa. This shows there is virtually no effect from the wind load on the critical stress.

The wireframe mesh used quadratic elements, with a total of 195 elements. Figure 4-16 shows the stress contour of the full wire frame model.

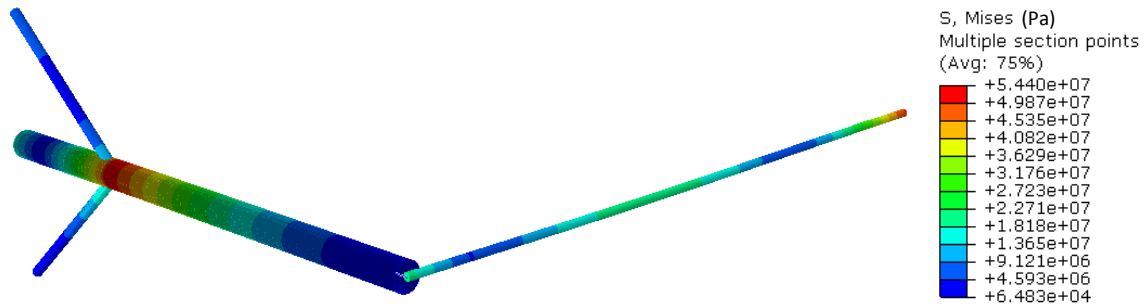


Figure 4-16 - Full Wireframe Model - Stress Contour

The stress at the vertical supports on the main boom was found to be 52.2 MPa. This represents a very small decrease in the stress of approximately 3.9%. The stress at the base of the boom was found to be 17.1 MPa, which is a small drop in the stress of approximately 4%. This suggests the lumped mass method was accurate. The maximum stress in the actuating truss was located at the end attached to the linear actuator, and was found to be 50.7 MPa. The yield strength of the material is 276 MPa, meaning the calculated maximum stress is within acceptable margins.

With a fully developed FEA model of the oil dispersant system, stress can easily be calculated for any point within the system. This fully developed model can be used during the detailed design stage, assisting the design of the connecting hardware, and other detailed design related components. The wireframe model is useful in determining the maximum stresses in the system, and understanding the interaction between components

of the system. However, the wireframe model lacks detail when it comes to the local effects of stress. To observe the local effects, a more advanced model must be developed. Also, the wireframe model lacks the ability to accurately represent the aerodynamic load as a distributed pressure across the face of the boom. There are two options available in FEA to further develop the model to this level of detail. The system can be modeled using shell elements, or solid elements. Shell elements are best suited for pipes, and objects that are thin. Solid elements can model complex detailed geometry, but are significantly less computationally efficient. For this case, a shell element was used to model the main boom. Figure 4-17 shows the main boom modelled using shell elements.

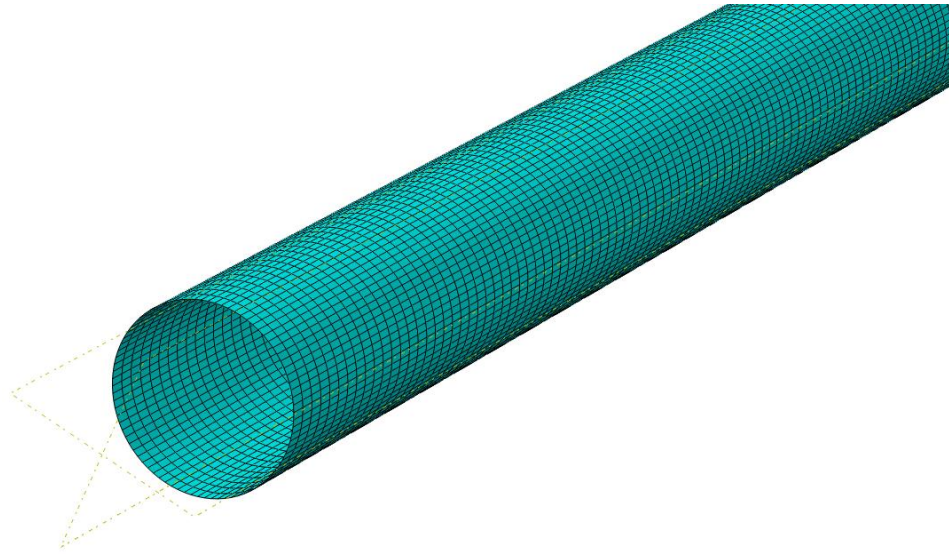


Figure 4-17 - Main Boom Shell Model Mesh

The boundary conditions at the base of the boom restricted translation in all directions, and rotation around the z-axis was free to rotate. The shell element S4R was used for this

application, with a total of 17,892 elements. The approximated truss force F_a was used in this simulation, as well as the approximated end load of the actuating truss. For demonstration purposes, the original minimum allowable pipe thickness was used. It was determined that the minimum allowable pipe thickness of 0.315 mm would provide a 1.1 safety factor from yield failure. Figure 4-18 shows the simulation result.

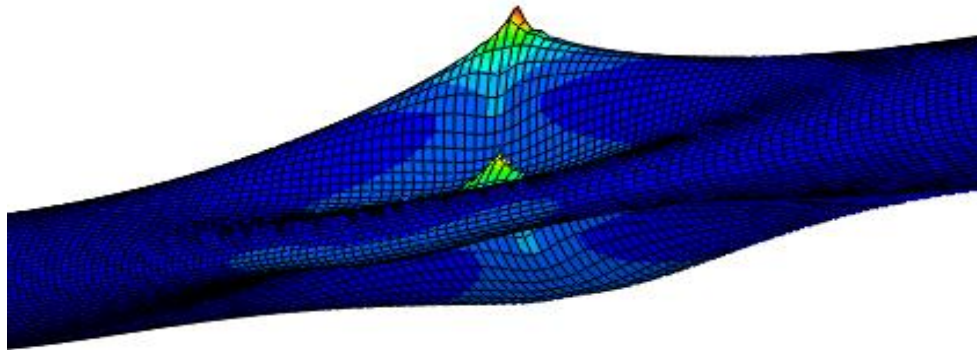


Figure 4-18 - Local Failure of the Main Boom at Vertical Support Truss - Unscaled

It is immediately obvious that significant deformations are occurring around both truss contact points. The boom is collapsing around the vertical support trusses catastrophically. This failure was not predicted by the analytical statics analysis. To understand this, it is important to understand local versus global stress analysis. The analytical and wireframe models viewed the system from a global analysis perspective,

where maximum stresses and overall loads were considered. The effect of a load on the entire model is observed, but localized effects such as buckling are not seen. A shell or solid element provide this unique insight into these localized effects, and show that sometimes the global view is not adequate. Although in this case, it would be obvious to most engineers that a pipe with thickness of 0.575 mm would be particularly susceptible to buckling and local failure, not all engineering applications may be as obvious. The decision to select a standard available pipe thickness of 3.175 mm (1/8") worked to prevent this localized buckling, but this highlights the importance of this tool. Figure 4-19 shows the main boom with the 3.175mm thickness under the same loading.



Figure 4-19 - Unscaled Deformation of Boom

Scaling the deformation by approximately 14 times provides a better picture of the shape of the deformation. Figure 4-20 shows the scaled deformation.

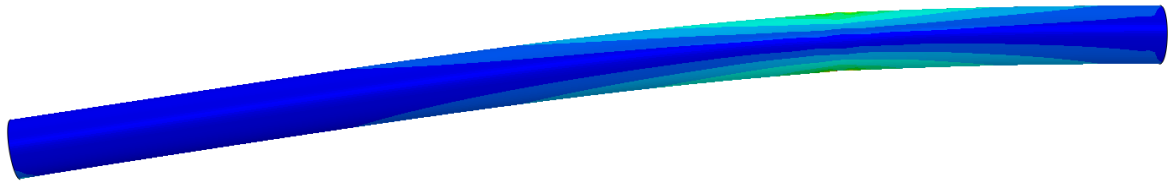


Figure 4-20 - Scaled to Show Deformation

It is immediately obvious that the increased thickness has eliminated the local buckling around the vertical support trusses. Though in this case the pipe thickness was increased due to manufacturing availability, this demonstrates how a design decision can be dictated by the use of advanced engineering techniques.

A closer look at the stress concentration at the support location provides a better view of the stress, where a very high stress value is seen. This value is not detected using the analytical method, but has more to do with how the support loading was applied than with inaccuracy in the wireframe model. A point load was used to apply the vertical support truss equivalent force. This point load is applied to an individual node, and therefore the force is applied to a very small area, creating a large stress. Figure 4-21 shows this significant increase in the stress as a result of modeling decisions, which reaches 151.2 MPa.

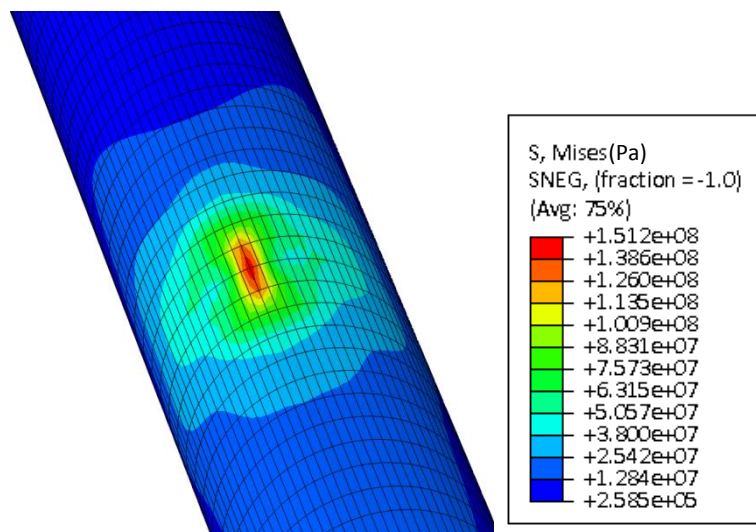


Figure 4-21 - Vertical Support Truss Force on Main Boom

The stress value that is taken away from this simulation must not be taken from this individual point. The actual truss supports will have connecting hardware that transfers the load, unlike the loading used here. If the stress is averaged out in the general region of the applied load, a stress of 50 – 60 MPa is found, similar to the results found in the wireframe model.

It is also desired to see the effects of the aerodynamic load on the shell model, applied as a pressure. The pressure results come from section 4.1 where computational fluid dynamics is used to solve for the distributed wind load on the main boom. It is possible to export the nodal values of force generated by the wind load, and apply it to the shell model. This is the fastest method once the initial complicated set up is complete. However, the fluid-structure interaction can be modelled quickly by applying an averaged pressure at several points. The pressure applied by the wind load was broken up into 6 thin strips, and applied to the front of the main boom. Figure 4-22 shows the forces applied to the boom using the pressures found in the CFD analysis.

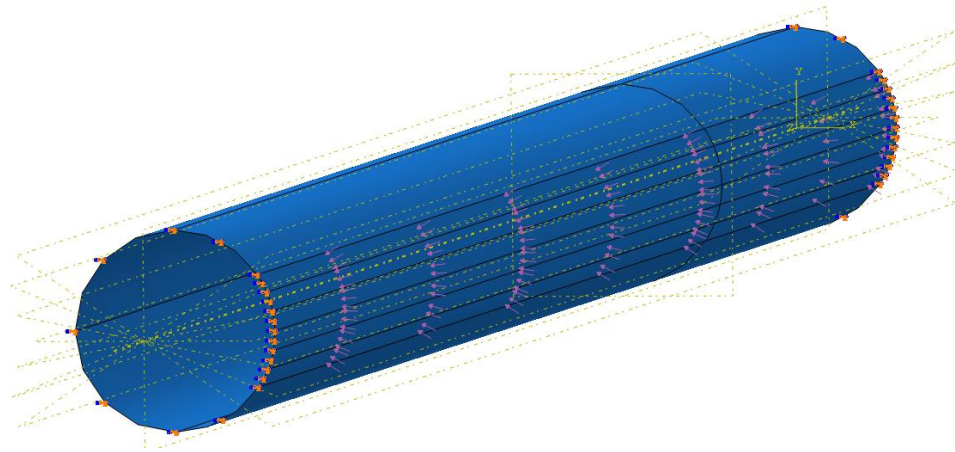


Figure 4-22 - Distributed Wind Load Applied to Shell Model

This distributed wind load was applied in absence of all other loading, as its effects on the overall stress are very small in comparison, and the effect would not be visualized. Figure 4-23 shows the stress contour of the main boom as a result of the wind load.

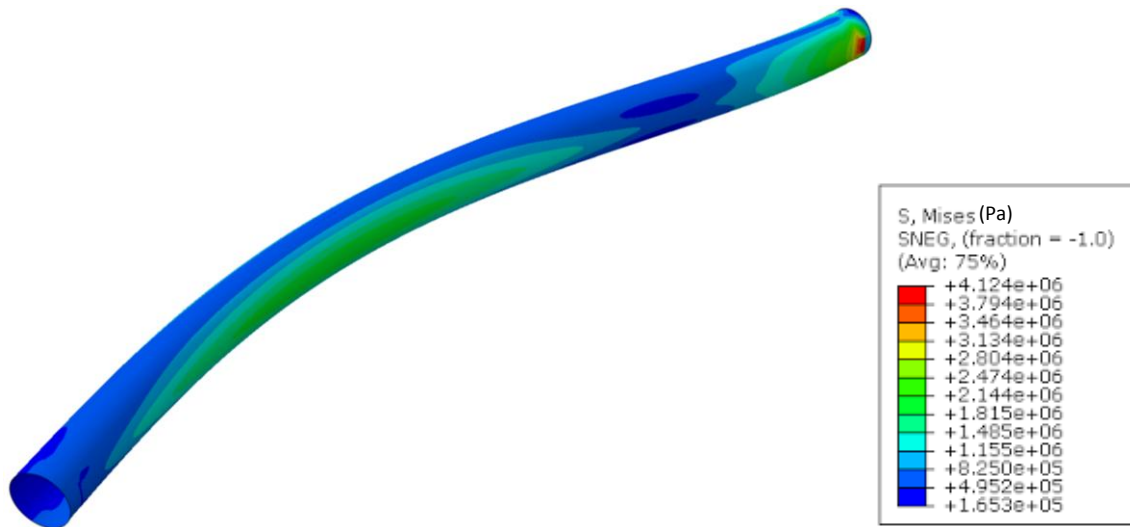


Figure 4-23 - Wind Load Applied to Main Boom, Stress Contour

An issue arose where the boundary conditions were set as a pinned-roller connection, as was seen in the static analysis. The boom should be free to rotate at both ends, with motion restricted. This would result in a maximum stress in the center of the boom. However, it is noted in Figure 4-23 that the maximum stress is located at the base of the shell. Though the proper boundary condition is applied, it counts every point around the perimeter of the boom as a pin connection, overall acting similar to an encastre connection. Figure 4-24 shows the same boom under the applied wind load, but with all the previous loading included. It is clear from the stress values that the wind load has a negligible effect on the critical stress in the system resulting from the inertial loads.

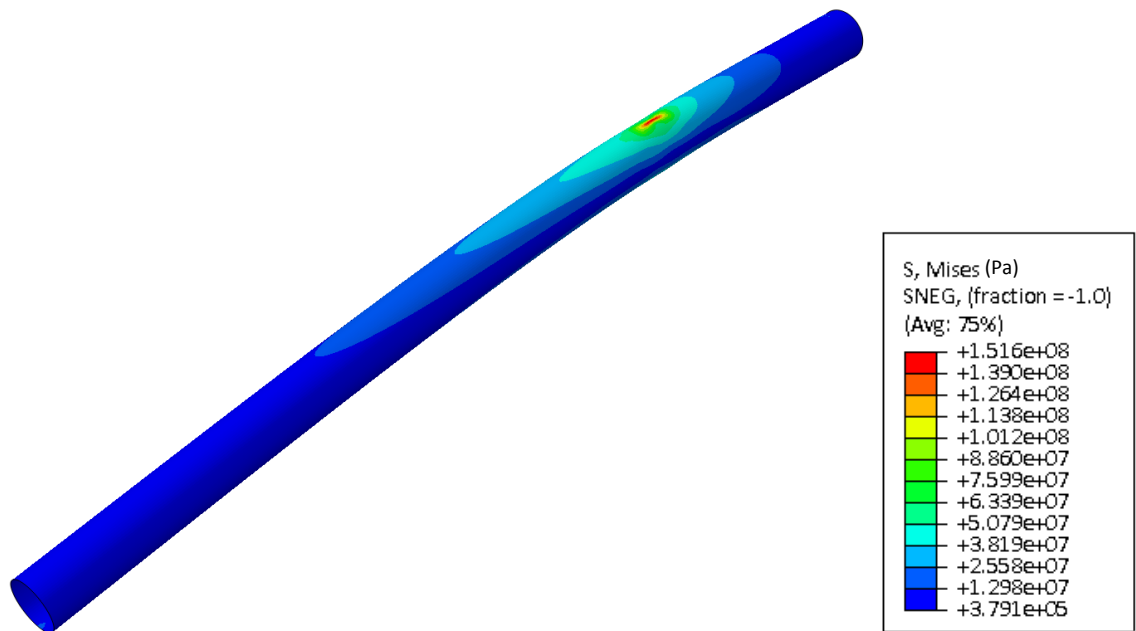


Figure 4-24 - Unscaled Deformation - Full Loading Scenario

Detailed design analysis can now be performed on the developed shell model. To demonstrate the capability of this model, the stress concentration resulting from the

nozzle holes will be observed. The nozzle hole sizes will be confirmed in the detailed design stage at a later date, but for demonstration purposes, a nozzle hole size of 0.00635 m (1/4") diameter will be used. 21 nozzle holes were cut into the main boom. Using the same loading conditions, the stress concentration around the nozzle holes was observed. The stress contour for the main boom with the spray nozzle holes is shown in Figure 4-25.

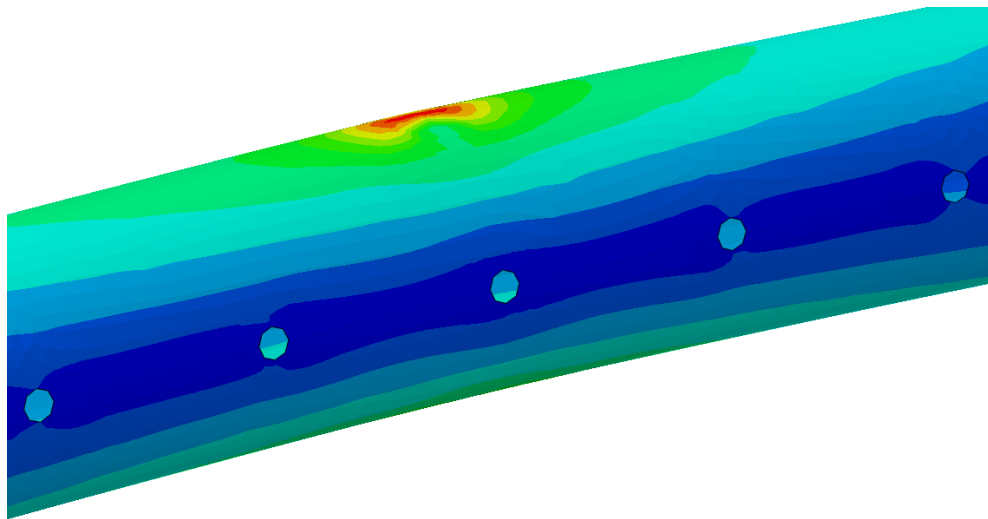


Figure 4-25 - Spray Nozzle Holes

The stress on the upper edge of the second from left nozzle seen in Figure 4-25 was found to be 11.2 MPa. The stress in the same region when the nozzles are not present is approximately 6.1 MPa showing there is an increase in stress as a result of the nozzles. Increasing the nozzle hole size results in a higher stress present at the nozzle edge. The nozzle hole size was doubled, and the result can be seen in Figure 4-26.

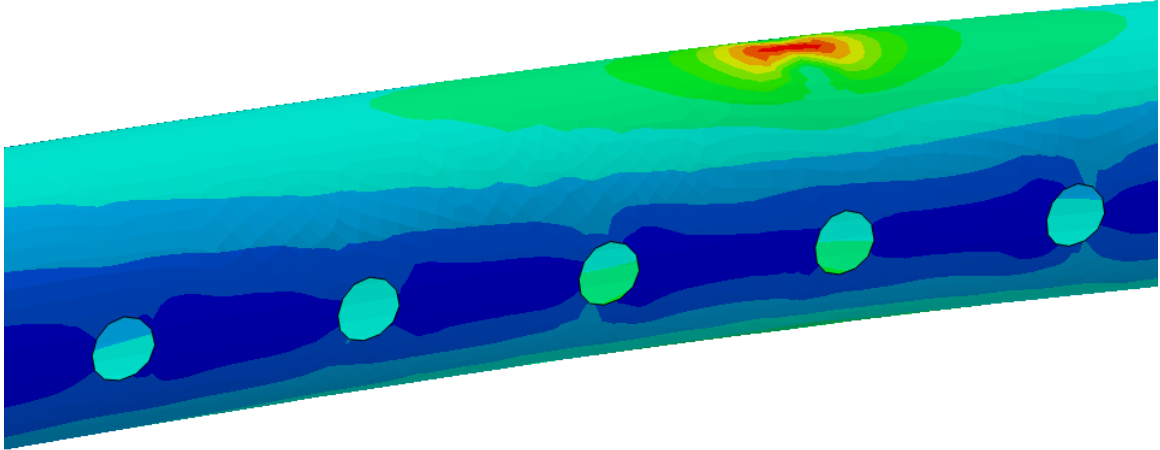


Figure 4-26 - Dispersant Boom with Large Nozzle Holes

The larger nozzle size resulted in greater stresses concentrated around the nozzle hole. The stress in the center nozzle hole has a stress of 20.0 MPa. Again, this is not a critical stress, but it does demonstrate the design value of the Finite Element Model.

Future iterations of the shell model can investigate several other aspects of the detailed design. Future iterations may consider including the truss members as actual shell or solid elements. This would require a developed detailed design to properly model how the trusses are attached, and how the load is distributed.

With a fully developed wireframe model, the loading and stress in the system can be determined at any point, including the supporting structure. This model was verified and developed beyond the analytical model, providing invaluable information for the design of the system. The shell model provided a unique look at the local response to the system

loading, and allowed for a fluid structure interaction simulation. This model is now prepared for the next step of developing the detailed design, allowing for a fast and accurate representation of the detailed system components.

4.3. Conclusion

In this chapter, a greater understanding of the complex loading on the deployable oil dispersant system was achieved. Using two advanced computational methods, a model was created that can be used to further the design and optimization of the oil dispersant system. Computational Fluid Dynamics provided good results that appeared to be in line with empirical data. This aerodynamic analysis provided a clearer picture of the wind load distribution across the main boom, which was then applied to the Finite Element Analysis model for greater accuracy. The Finite Element model began with simplified analysis as a benchmark, and was then developed into a full model. Both the wireframe model and the shell element model are now ready to be used as tools in the detailed design process, allowing for the optimization of the system design. This chapter demonstrated how advanced engineering techniques such as FEA and CFD can be used in conjunction with standard analytical techniques to further develop the design and provide confidence in the results.

5. Dynamics

This chapter considers the behavior of the system during the deployment and stowing operation. During this stage of operation, the system will experience dynamic forces that can potentially exceed the maximum forces calculated in the static analysis. Therefore, it is important to consider the forces during the operation of the mechanism and the manner in which they might affect the overall design of the system. The dynamic analysis covered in this chapter makes use of the dynamics simulation program 20-sim and the bond graph technique in order to simulate the operation of the deployable dispersant system. This analysis provides a unique insight into several important design requirements involved in the secondary system design.

In chapter 3, the preliminary design was determined using standard analytical techniques including static and aerodynamic analysis. This static analysis considered a fully deployed system locked in place, with stresses calculated from wind and weight loading on the system components. However, this analysis did not consider the loading experienced during the operation of the system. The loads experienced as the boom is deployed or stowed are affected by many factors, such as inertia and motor start up effects. This section considers the actual motion of the system and forces within, as it deploys or stows. It discusses the development of a realistic dynamics simulation model, and then carries out in-depth analysis of the loading and linear actuator operation during the deployment of the oil dispersant boom.

5.1. Dynamics System Description

The first step in creating the dynamics model is to define the system to be modelled. As mentioned, the geometry and loading of the oil dispersant boom preliminary design described in chapter 3 will be used for this dynamics model. Figure 5-1 and Figure 5-2 shows the system deploying from its initially stowed position.

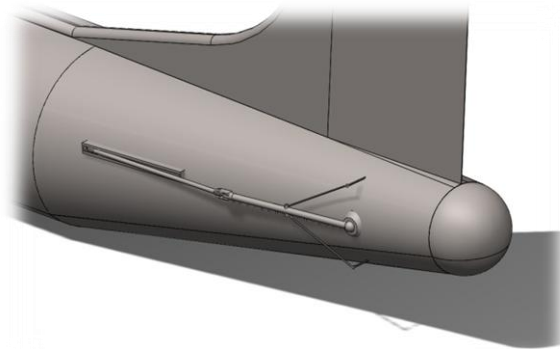


Figure 5-1 - Fully Stowed Position

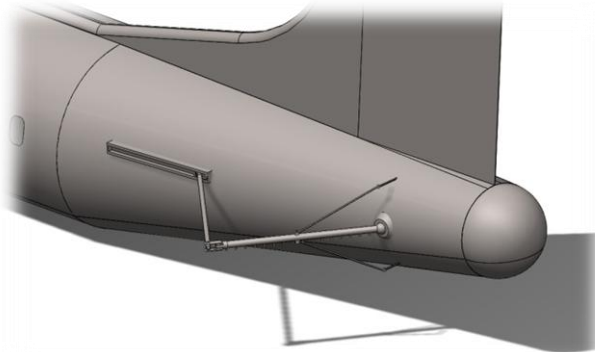


Figure 5-2 - Fully Deployed Position

There are two forces that dictate the motion of the system during operation. The actuator is driven by a motor which moves the actuating truss, and is the primary controlling force. The wind load is in the same plane as the actuator and direction of the boom deployment.

The wind load is the primary force that must be overcome in order for the system to operate. The inertial force due to weight is out of plane from the motion, and does not apply a force in the direction of motion. Figure 5-3 shows the described system definition.

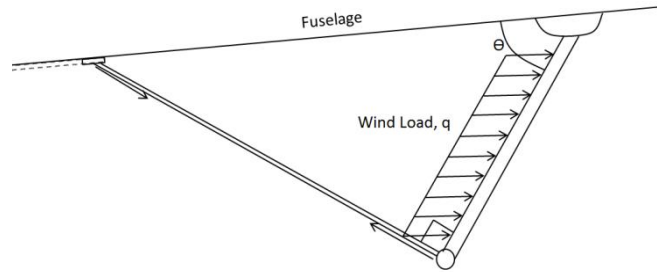


Figure 5-3 - System Loading Description

The system is oriented such that the wind load will act to extend the boom arm. When the system is fully stowed, there should be a very small amount of wind load. When the system is fully deployed, it should experience the wind load calculated in chapter 3. To simplify the simulation, the wind load is only applied to the main boom. Its larger cross-section equates to a more significant wind load as compared to all other system components. To further simplify the loading, the wind load is taken as a point load rather than distributed load as seen in previous calculations. An equivalent point load is applied to the center of the main boom. Only an x-component of the wind load is applied, as it is the direction of flow. The actuating force is applied at the far end of the actuating truss. This force is applied only in the direction of the actuator. For this simulation, the frictional resistance in the rotating joints is ignored. The wind load is assumed to be

constant, and decreases as the system slows. The system parameters outlined in chapter 3 will be used for the dynamics model.

5.2. 20-Sim

20-sim [52] is used as a tool to simulate the dynamic response of the system under loading. It is a versatile program that can model a dynamic system using Simulink-like block diagrams, 3D CAD models, bond graphs, and equations. It is particularly known for its support of bond graph simulation, and is the program of choice among many bond graph users. All of these methods can be used simultaneously, providing many unique tools and options for the realistic simulation of a system. 20-sim also has many tools for data analysis, and can be used for control system design. Figure 5-4 shows the graphical interface seen in the main 20-sim window.

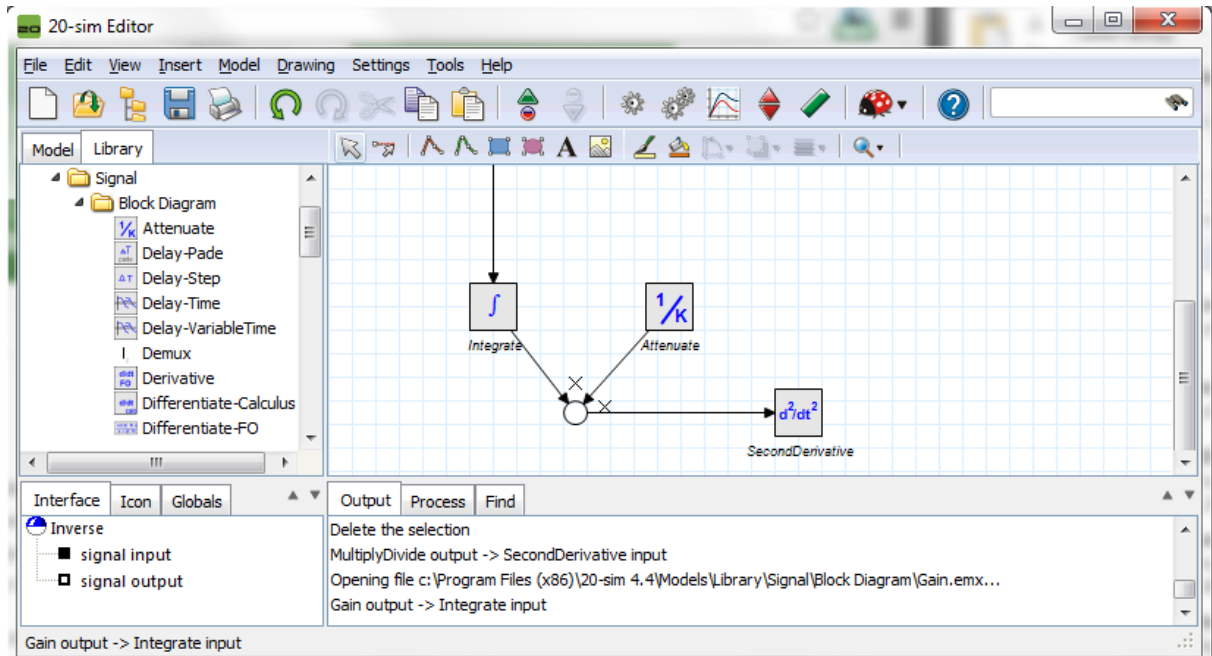


Figure 5-4 - 20-Sim Graphical Interface

A library containing a large number of different simulation and control tools provides the user with many options for creating a realistic simulation [52]. Many pre-made iconic diagrams were created to simulate standard engineering components such as pumps, actuators, and motors. Block diagrams representing a large range of functions, from integration to PID control can be joined together to create the dynamics simulation model. Bond graph components, which will be explained in more detail later, can also be used to create complex subsystems, which can interact with both block and iconic diagrams. A unique feature of 20-sim is the 3D Mechanics Toolbox. This feature allows for the creation of a 3D CAD model, which can then be imported into the 20-sim graphical interface, and interact with the bond graph, block diagrams, and iconic diagrams. The 3D model can interface with the other simulation components by controlling force inputs.

These inputs can be point forces, rotation joints, or translation joints. Sensors allow for data to be read from the 3D model, and are useful for using as an input for a control loop, or data analysis. Figure 5-5 shows the 3D Mechanics toolbox window.

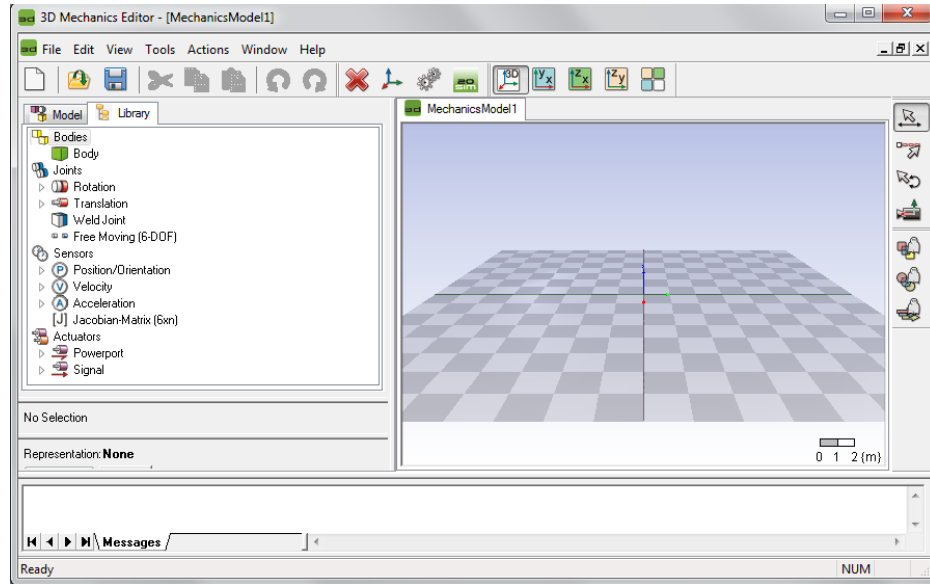


Figure 5-5 - 3D Mechanics Toolbox

The 3D Mechanics toolbox is used to create a 3D CAD representation of the system described in section 5. The dimensions chosen for the preliminary design were used for the CAD model dimensions. An actuated x-translation joint is used to represent the linear actuator. A power interaction port was activated for this linear actuator, which allows for the 20-sim graphical interface to control the actuator force applied. A point force was placed on the center of the main boom, and will be used to apply the wind load. Figure 5-6 shows the 3D CAD model created using the preliminary design specifications.

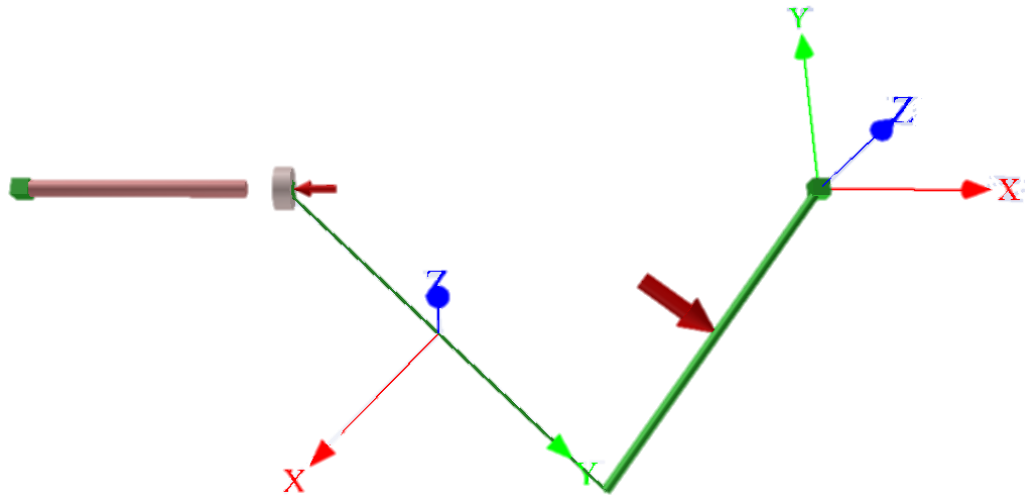


Figure 5-6 - 3D Mechanics CAD Model

Both force inputs described in the system description can be observed in Figure 5-6. The wind load point force can be seen as a large arrow on the larger link on the right, which represents the main dispersant boom. The actuator force input can be seen as a smaller arrow on the left end of the mechanism. These two force inputs will later be used as power port interactions with the main dynamics model in the 20-sim graphical interface. The moment of inertia and weight values are also input directly into the component properties at this stage.

5.3. Simplified Model

The simulation of this 3D CAD model will begin with a simplified model. A simple model will keep the focus on the interaction between the 3D CAD model and the 20-Sim graphical interface. Once adequate accuracy is achieved for the simplified model, it can be improved by adding in more subsystems and features to create a more realistic

simulation. With the 3D CAD model complete, it is desired to control the model using the 20-sim graphical interface. This was done by using the built in 3D mechanics toolbox for generating a 20-sim model. Figure 5-7 shows the generated block diagram on the right, with its identified ports on the left. ForceX1 represents the aerodynamic load input, and ForceX2 represents the actuator input.

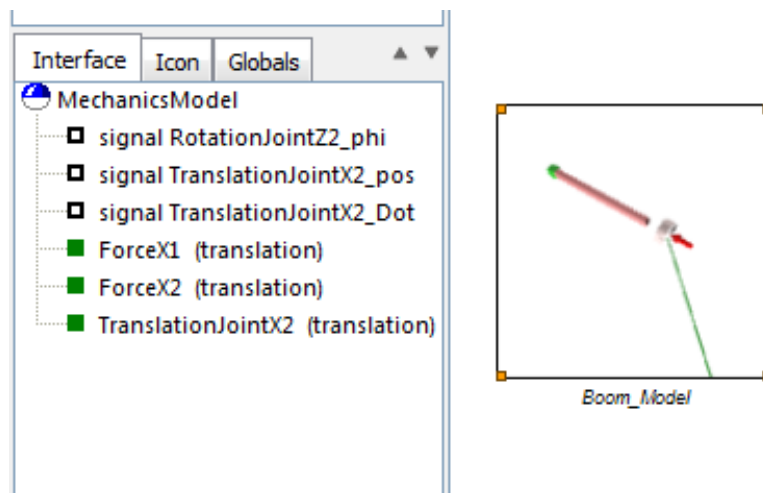


Figure 5-7 - 3D CAD Model in 20-Sim Graphical Interface

As observed in chapter 3, the aerodynamic loading is a complicated function. The wind load was calculated for a pipe that is directly perpendicular to the flow direction, where the load will be a maximum. However, as the boom retracts, this wind load will change. The overall frontal area affected by the wind load will decrease as the system stows. Also, the cross-section seen by the air flow will no longer be a circle, becoming an ellipse, thus changing the wind load. A simpler method of calculating the wind load as the system deploys and stows was desired. It was decided that the wind load be a function of the

angle of the main boom. As the boom stows, and becomes more and more parallel to the wind flow direction, the wind load will decrease. The sine of the angle the boom makes with the perpendicular position is multiplied by the wind load value calculated for the pipe perpendicular to the flow. The angle output from the 3D Mechanics model is the angle the boom makes with the positive x-axis, which is 180° minus the angle described before, which is demonstrated in Figure 5-8.

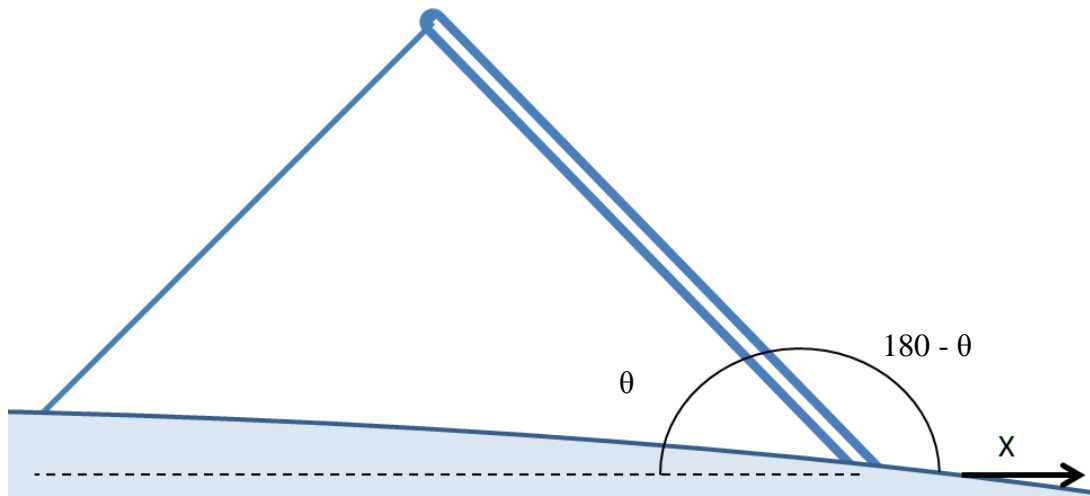


Figure 5-8 - Opposite Angles

It is noted that the sine of 180 minus the angle is equivalent to the cosine of that angle, thus the cosine of that angle was used. Figure 5-9 shows the angle being read from the 3D mechanics model, and then the cosine is taken of that value, and finally is multiplied by the aerodynamic value in the gain block. The gain is simply the force value determined earlier for the fully perpendicular flow. Finally, this is input as a force back into the 3D

mechanics model using the modulated effort source. A modulated effort source is simply a force input that can be controlled, rather than a constant input.

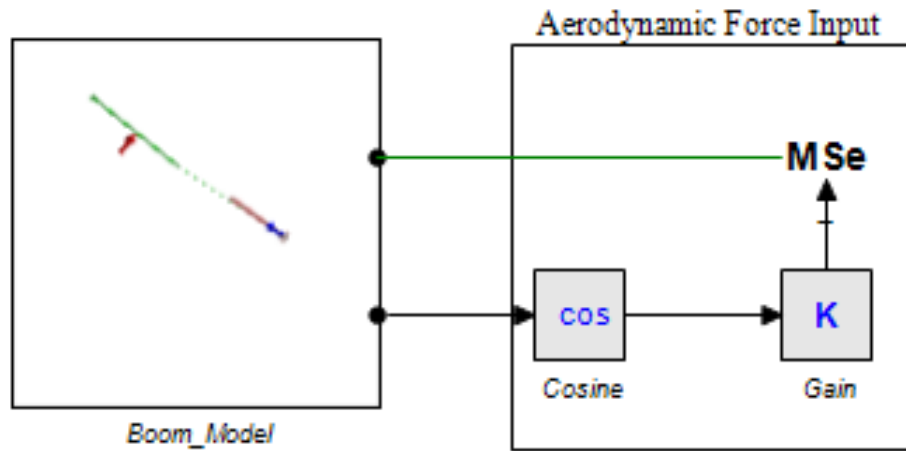


Figure 5-9 - Aerodynamic Force Input

The next step is to create the force input that will control the linear actuator. The linear actuator must overcome the aerodynamic load, and is the primary force for the system deployment. Since the aerodynamic force will change depending on the deployment angle, the linear actuator force must be able to react to that change. A simple control loop is implemented such that the velocity of the system can be controlled. Figure 5-10 shows the simplified control loop used to control the system.

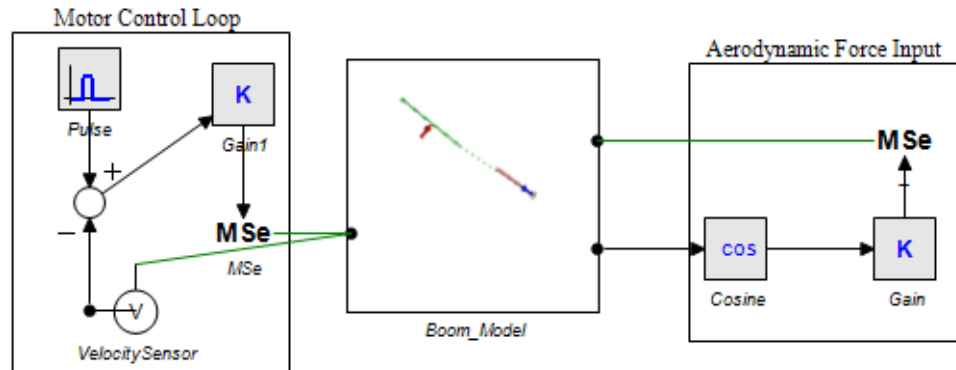


Figure 5-10 - Control Loop with Boom Model

This velocity control loop works by constantly regulating the force input such that the system travels at the desired velocity. The velocity resulting from the force is used to calculate the error between the target velocity and the current system velocity. This error is multiplied by some gain value such that the force applied is large enough to overcome the aerodynamic load. If the system velocity greatly exceeds the target velocity, a large negative force is created, acting to slow the system down. As the velocity slowly approaches the target velocity, the force applied reduces until the target velocity is reached. This self-regulating control loop concept will later be refined in a more realistic model.

With the dynamics model constructed, the simulation results can now be observed. 20-Sim uses a simple interface to allow the user to select from every parameter available. In this case, the forces are the major concern. Figure 5-11 shows the force required to overcome the aerodynamic force, and move the actuator at a fixed velocity.

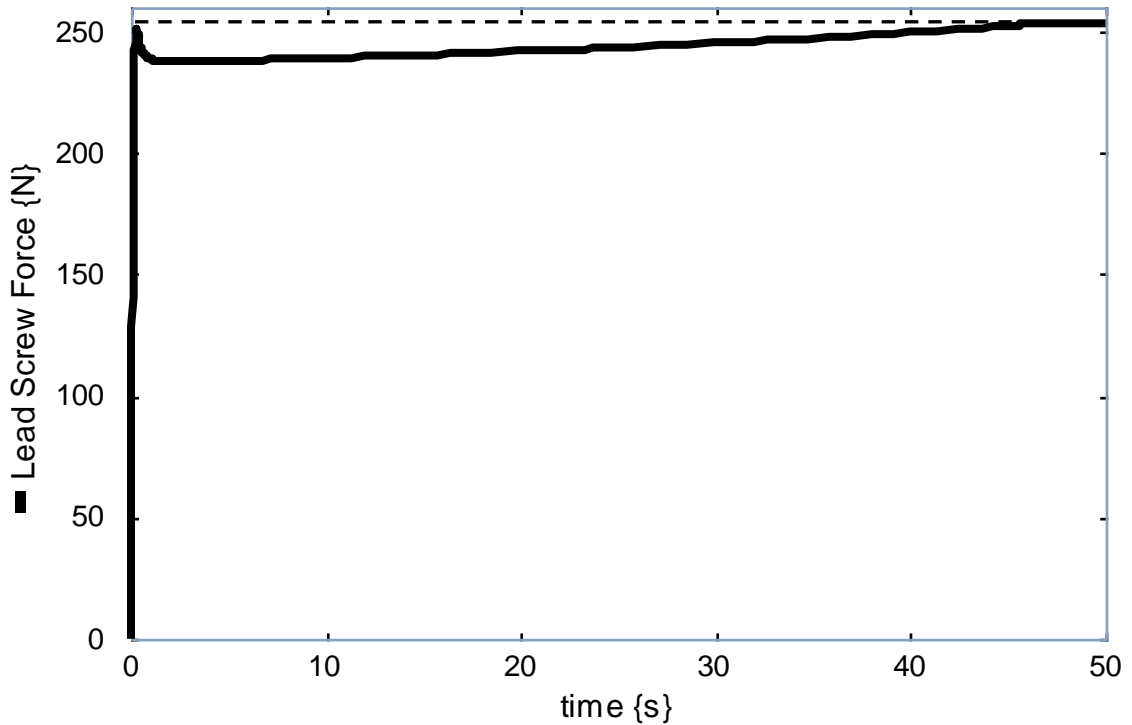


Figure 5-11 – Lead screw Benchmark Analysis

The deployment time of 65 seconds is shown. As the system transitions from a stowed position to a deployed position, the force required to extend the system increases. This is because the wind load increases as the system deploys. After approximately 65 seconds, the system sits in a fully deployed position, and a force of 252N is observed. Since the system is not moving at this point, it is expected that the static analysis result for the actuator force at this point should match the 20-Sim simulation value. To do this, the aerodynamic force was applied as seen in Figure 5-12, and the reaction forces were determined.

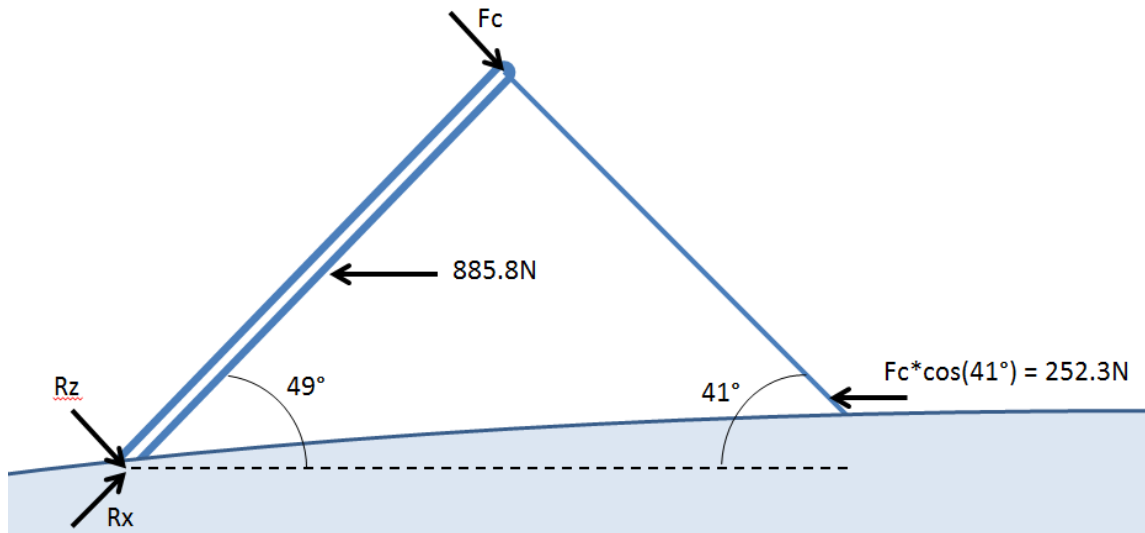


Figure 5-12 - Force on Actuator due to Aerodynamic Load

This simple static analysis yielded the result of 252.3N, just as the dynamics simulation predicted. With a high degree of confidence in the statics calculations, this correlation provides validation for the 3D Mechanics model. With a firm grasp of how to interact with the 3D Mechanics model, and confidence in the results, the next step can be taken to further refine the model.

5.4. Realistic Simulation

As discussed in section 5.3, the dynamics model to this point has been used to simulate the motion of the system, and calculate the changing forces. This was shown to coincide with expected values, thereby validating the simplified model. It is important to point out that all of the effort in creating a dynamics model to this point provided the same data as quick and simple static analysis. This brings forward the reasons behind this simulation

technique being used while much simpler and equally accurate methods already exist. The true value of this technique will become apparent once the complexity of the model is increased, and the validated existing model is built upon. Using this validated model provides confidence moving forward, as further subsystems are modelled, and the overall model is refined. 20-Sim and the bond graph technique provide a unique tool for modelling many more aspects of the overall system, and allow for a more realistic simulation of the system. To demonstrate this, the linear actuator subsystem will be modelled using bond graph, and the control loop will be refined.

5.4.1. Bond Graph

In this section, a brief introduction to bond graphs will be given, followed by the development of a bond graph model for the simulation of the lead screw system.

The bond graph technique seeks to model complex systems by considering each subsystem and how they interact with each other through power bonds. This graphical technique presents the complex system using a series of symbols that show the power flow between these subcomponents, and can combine several kinds of engineering systems. Using this technique, the power flow between electrical, rotational, mechanical, and hydraulic systems all appear identical in how they are modelled. Though the form of energy differs between them, all of their interactions can be modelled as a power interaction. The bond graph model allows for a significantly improved method of determining the standard dynamics state equations. Further, the simplicity of the overall model as compared to the standard dynamics analysis techniques provides an intuitive

view of the entire system, allowing for more efficient and relevant analysis of subsystem interactions, system optimization, and troubleshooting.

The first step in understanding the bond graph technique is to understand the idea of the power interaction between subsystems. Regardless of whether you are looking at a physical, electrical, or hydraulic system, power is effort multiplied with flow over time. Effort and flow have many different names, depending on the system you are considering. Table 5-1 shows the common engineering notation given for each type of system for defining effort and flow.

Table 5-1 - Bond Graph Power Variables

Domain	Effort	Flow
Mechanical Translation	Force	Velocity
Mechanical Rotation	Torque	Angular velocity
Hydraulic	Pressure	Volume flow rate
Electrical	Voltage	Current

The most efficient way to explain the method is to demonstrate it through an example. Before that can be done, the basic elements of a bond graph must be presented. Once these are presented, two examples will provide a much clearer view of the bond graph technique and how it works.

There are three primary elements, two types of sources, as well as a scaling type element (such as a lever or transformer), and a gyrator device relating effort and flow [53]. All of

these elements are connected using bonds represented by a stroke with a half-arrow, and effort and flow junctions.

The three primary elements are the resistance element, capacitance element, and inertia element. The resistance element, shown in Figure 5-13, can be imagined as a standard electrical resistor.



Figure 5-13 - Resistance Element

Resistors dissipate energy, and effort and flow are related in a static function. Equation 5-1 shows the familiar Ohm's law, and how it can be written in terms of effort and flow:

$$\begin{array}{l}
 \overline{\longrightarrow} \quad V = iR \quad \rightarrow \quad e = fR \\
 \longrightarrow \quad i = V/R \quad \rightarrow \quad f = e/R
 \end{array}
 \quad 5-1$$

It is important to note the causal stroke seen on the end of the power bond arrow. The causal stroke indicates the equation input-output structure. The element the causal stroke is adjacent to is considered as the input to the element, whereas the element on the opposite end will compute the effort output. Equation 5-1 shows how the causal stroke alters the input-output structure of the resistance element.

Voltage is equivalent to effort, and current is equivalent to flow. This resistance element exists in the mechanical, rotational, and hydraulic applications as well. These are all familiar items, such as slider or bearing resistance, and porous plugs in a water pipe.

The second primary element is the inertia element. Inertia in an electrical system is simply an inductor. In a mechanical, hydraulic and rotational sense, it is the mass or inertia in the subsystem. Figure 5-14 shows the inertia element.



Figure 5-14 - Inertia Element

The inertia element is more complex than the resistance element. Inertia is a function of the momentum, which is a function of the time integral of effort, or force. This can be written as:

$$P = \int_{-\infty}^t F dt = \int_{-\infty}^t e dt \quad 5-2$$

This gives the relationship between effort and flow using the standard momentum equation as follows:

$$P = mv \quad \rightarrow \quad v = \frac{1}{m} \int_{-\infty}^t e dt \quad 5-3$$

This equation shows the effort is the cause, and velocity results. Other causality is possible, but less desirable.

The final energetic element is capacitance. Capacitance is represented in an electrical system as a capacitor. Figure 5-15 shows the capacitance element.

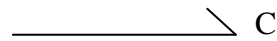


Figure 5-15 - Capacitance Element

Capacitance elements store and release energy, and can be thought of as a spring or a water tank. The equation for capacitance is based on a familiar equation, Hooke's law.

The Hooke's law equation for a spring is:

$$F = kx \quad \rightarrow \quad e = kx \quad \rightarrow \quad e = k \int_{-\infty}^t v \, dt \quad 5-4$$

This equation shows the change in flow, leads to a resulting effort.

There are two source elements. These are the effort source, and the flow source. These provide the input to the system, and can be modulated sources, allowing for non-linear inputs and other controlled inputs. An effort source can be thought of as applying a force, and observing the resulting velocity. A flow source works in the opposite way, where a velocity is applied, and the resulting force can be observed.



Figure 5-16 - Effort Source and Flow Source Elements

The transformer element acts as a scaling element. A good visualization for the transformer element is a lever. The ratio of the lever arm lengths on either side of the fulcrum dictate the scaling of the force. Figure 5-17 shows this relationship.

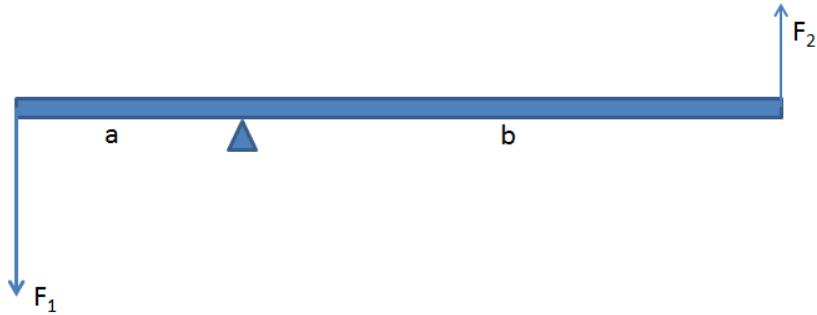


Figure 5-17 - Transformer Lever Analogy

This relationship can be written for both flow and effort. The equation for the transformer is as follows:

$$F_2 = (a/b)F_1$$

$$V_2 = (b/a)V_1$$

$$e_2 = r e_1$$

$$f_2 = (1/r)f_1$$

5-5

The transformer element can be seen in Figure 5-18.



Figure 5-18 - Transformer Element

The next element is the gyrator. The gyrator directly relates flow to effort, or effort to flow, and the symbol is seen in Figure 5-19.



Figure 5-19 - Gyrator Element

An example of a mechanical gyrator would be a gyroscope. A gyroscope has a spinning flywheel, which uses rotational momentum as a righting moment, keeping the system stable. A rack and pinion also acts as a gyrator, as an applied rotational torque of the pinion is translated into a linear velocity of the rack. A DC motor is an example of an electrical gyrator, as the output rotational velocity is converted to back emf, and current is converted to torque.

Finally, the junction elements will be explained. There are two types of junctions; the 1-junction and the 0-junction. These are the primary elements that connect the subsystems to each other. The 0-junction is called the flow junction, or the common effort junction. It is essentially Kirchhoff's current law, where the sum of all currents into a node is equal to 0. All of the efforts into the node are equal. This can be equated to a mechanical system, but it is more complex to consider. Consider a series of springs attached together. The

velocity at the end node will be the sum of the relative velocities of each spring, and the force applied will be equal on each spring, assuming they are massless.

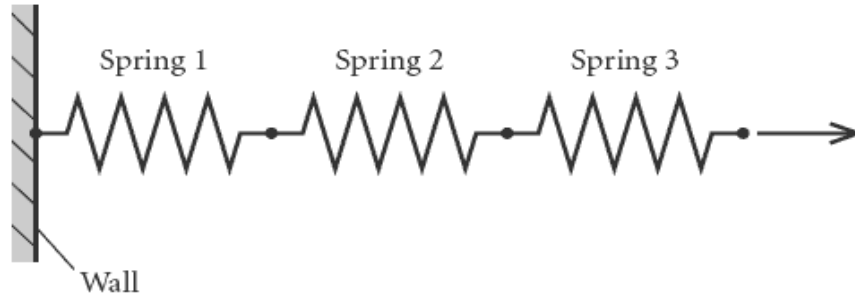


Figure 5-20 - Springs in Series [54]

The 1-junction is the effort junction, or the common flow junction. It is essentially the Kirchhoff's voltage law, where the sum of the voltages around the closed circuit loop is equal to zero, and the current is constant throughout. The mechanical equivalent is easier to understand as compared to the 0-junction, as it is the sum of forces equal to zero, seen in classical mechanics. It represents a single point of mass in the system. Consider springs in parallel, where the overall force applied is divided between each spring, and the velocity of each spring is equal.

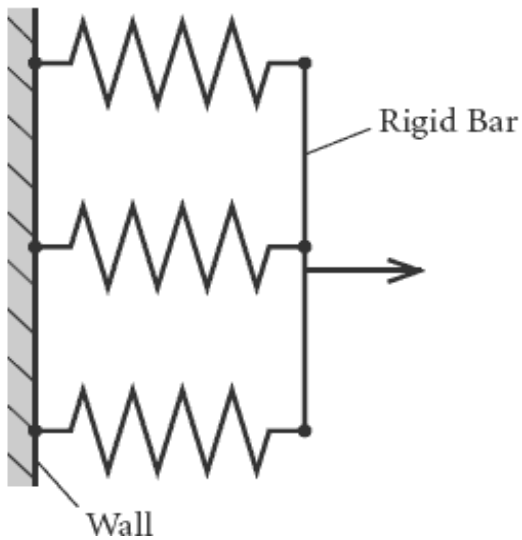


Figure 5-21 - Springs in Parallel [54]

These junctions are used along with the previous elements presented to create a bond graph. A simple example using an electrical system and a mechanical system will help clarify how exactly these elements are used to create a dynamics model.

Consider the electrical circuit seen in Figure 5-22 below. It is a very simple circuit, containing both elements in series, and parallel. It also contains one of each element.

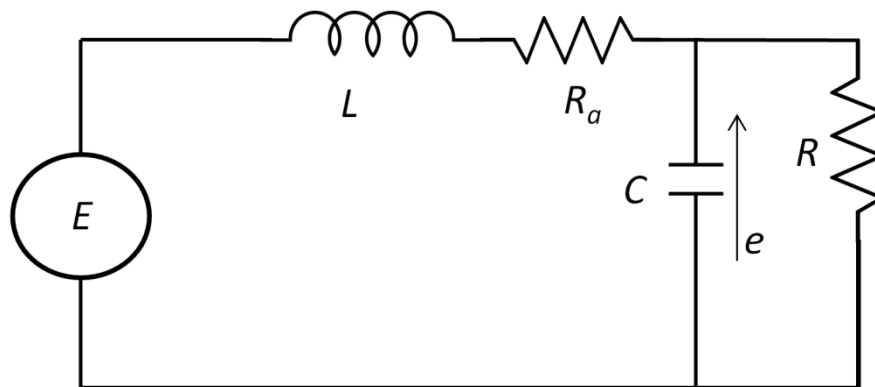


Figure 5-22 - Circuit Diagram [55]

To be creating a bond graph of this model, Kirchhoff's voltage law will be used around the left loop. This creates a 1-junction. The voltage source, inductor L , and resistor R_a all connect to this 1-junction, as seen in Figure 5-23.

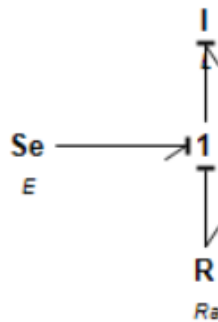


Figure 5-23 - Developing the Bond Graph

The next step is to use Kirchhoff's current law around the top node. The capacitor and remaining resistor, as well as the three other elements in series, are connected to this node. This yields the result seen in Figure 5-24.

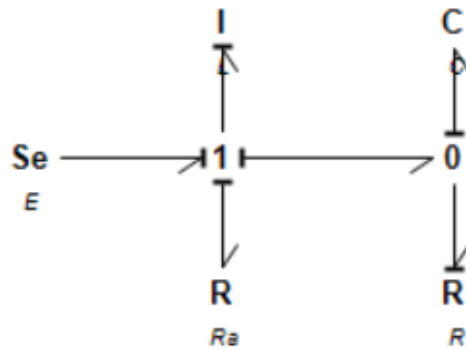


Figure 5-24 - Bond Graph Solution of Circuit Diagram

This completes the bond graph of the circuit shown above. From this, the state equations can be determined. The state equations allow for the calculating of the system response, where voltage and current can be determined at the 1-junction and 0-junction points. 20-Sim automatically generates these equations, as well as determines the causality, or direction of power flow.

The circuit example provides an overview of how to construct a basic bond graph, but only shows one type of system. To understand how multiple subsystems can be joined, consider the electromechanical system in Figure 5-25.



Figure 5-25 - DC Motor Example

This system consists of a basic DC motor with a voltage source applying torque to a shaft. This represents two different types of energy, electrical and mechanical energy. Voltage in the DC motor drives the shaft, and will therefore make use of a gyrator element. The circuit is kept simple for the DC motor, including the resistance and the coil impedance of the motor. The figure below shows the bond graph of the circuit thus far.

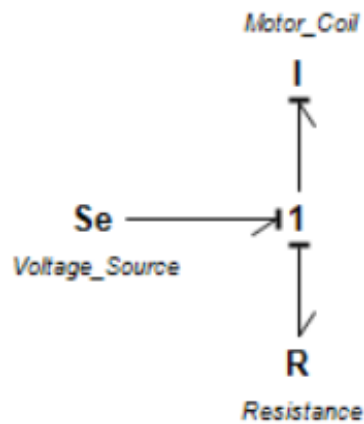


Figure 5-26 - Basic DC Motor Circuit

As described earlier, the gyrator element converts effort to flow, or in this case, voltage to rotational velocity. The gyrator element will connect the DC motor electrical component to the output torque. For this example, the rotational resistance from the bearings will be considered. Also, the rotational inertia will be included in the model. Both of these elements are associated with the same angular velocity, and require a single 1-junction to represent it, as seen in Figure 5-27.

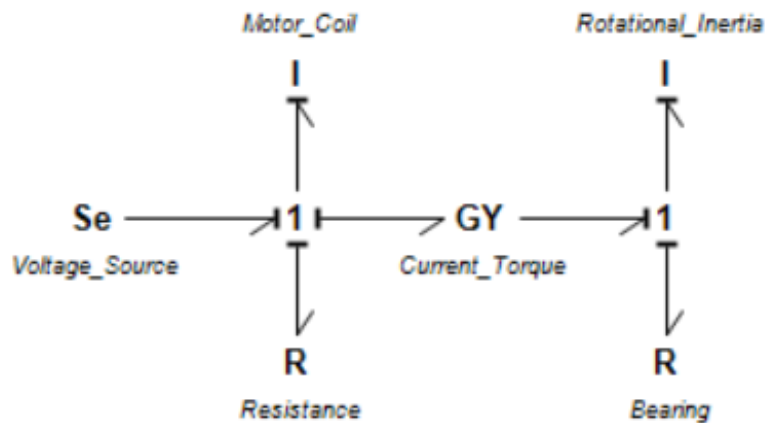


Figure 5-27 - DC Motor Spinning a Shaft

This example shows how the bond graph technique allows for a combination of many different kinds of subsystems, whether they are electrical, mechanical, or hydraulic.

With a brief overview of the bond graph technique, it is hopefully clear how a system can be modelled. The bond graph technique provides a unique way of combining multiple subsystems, spanning across multiple disciplines. It is with this knowledge that the 20-Sim model can be further refined to create a more realistic model.

The linear actuator is an ideal subject to consider creating a bond graph model for. A lead screw type system was chosen for its high torque and ability to resist slip. Figure 5-28 shows a lead screw system similar to what will be used.

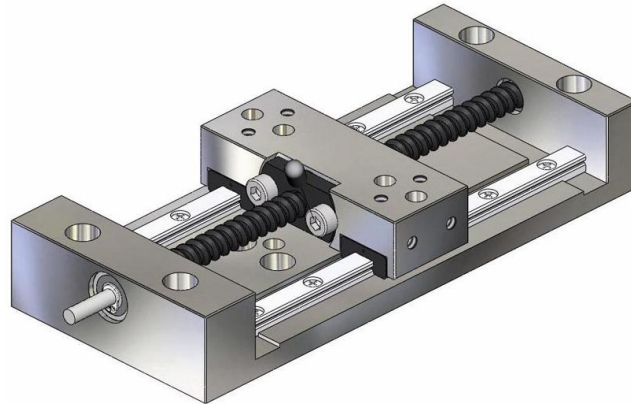


Figure 5-28 - A Typical Lead Screw [56]

A lead screw consists of 3 primary subsystems. The electrical and motor component, the rotating screw and bearings, and the sliding mount. The motor is powered, which turns the screw, providing a force to the threaded sliding mount. To begin, a literature review was carried out to find similar systems and examples to this application. A very thorough model of a CNC machine system is developed and presented by Tomar and Das at the 2007 SAE World Congress [57]. This application is technically very similar to the application in mind for this thesis. It uses heavier equipment, and involved in metalworking. However, fundamentally, it has a motor that applies torque to a threaded rod, which moves the main block, very similar to the lead screw. Figure 5-29 shows the schematic diagram of the CNC machine.

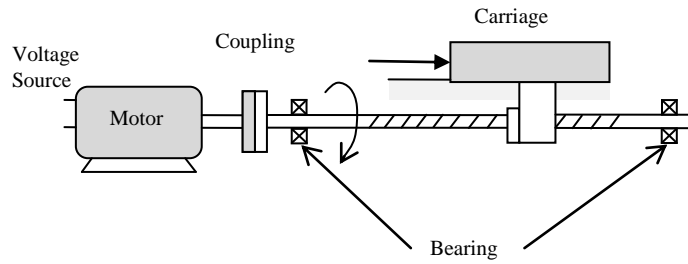


Figure 5-29 - CNC Machine Subcomponents [57]

The CNC machine consists of a motor spinning a threaded shaft, which moves a carriage holding the part being manufactured. The CNC machine also makes use of a coupling, and bearings. The bond graph model developed is shown in Figure 5-30.

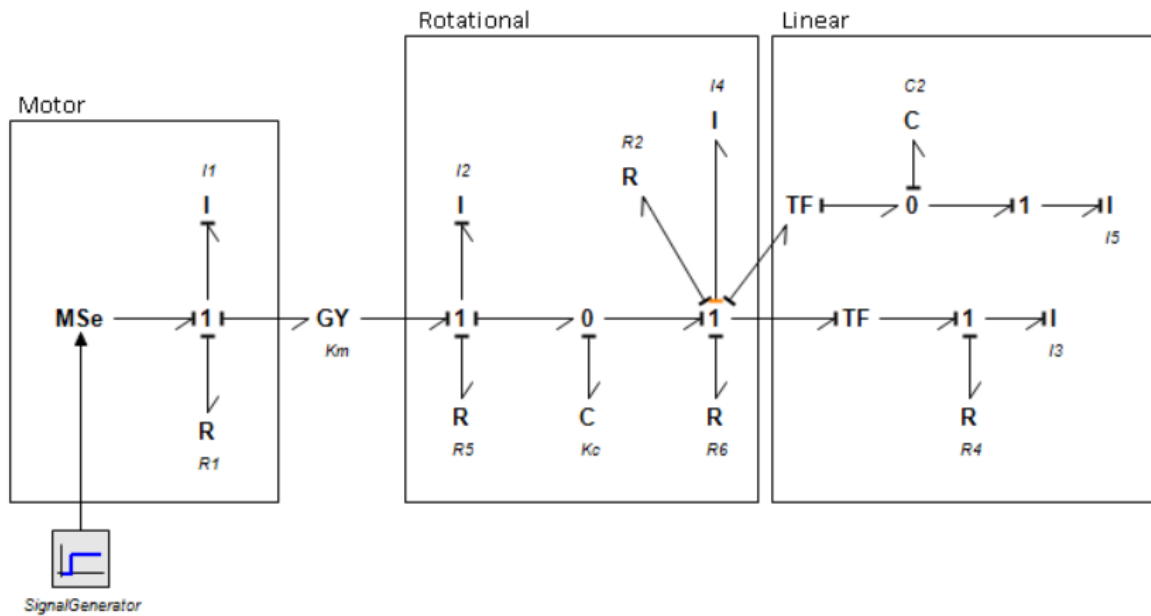


Figure 5-30 - CNC Machine Bond Graph Model

The overall concept is that the motor converts the input current into an output torque using the gyrator. The output torque turns a shaft, which experiences bearing resistance and rotational inertia. This rotation is converted into linear motion using the transformer. The top branch represents the lead screw stiffness and its equivalent mass with respect to linear motion. The bottom branch represents the actual linear motion of the carriage. Table 5-2 - CNC Machine Parameters gives a description of each parameter, and their value.

Table 5-2 - CNC Machine Parameters

Element	Description	Value
I1	Motor Impedance	0.0252 Henrys
I2	Rotational Inertia of Left Shaft	0.0022 Kg.m ²
I3	Inertia of Track	77 Kg
I4	Rotational Inertia of Right Shaft	0.0007791 Kg.m ²
I5	Shaft Equivalent Mass	5.45 Kg
R1	Electrical Resistance	1.09 Ω
R2	Lead Screw Bearing Resistance	0.03 N.m.s/rad
R4	Viscous Damping in Slideways	6.77 N
R5	Motor Bearing Resistance	0.00002 N.m.s/rad
R6	Lead Screw Bearing Resistance	0.03 N.m.s/rad
C1	Coupling Stiffness	2700 N/m
C2	Lead Screw Stiffness	159000000 N/m
GY	Motor Constant	20 V/(rad/s)
TF	Distance Travelled Per Rotation	0.001019108 cm/rotation

The CNC system model provides an excellent starting place for the development of the linear actuator model for the deployable oil dispersant system. The bond graph was developed in the 20-Sim dynamics software. As with the CNC machine example, the system will be powered by a basic voltage source. The DC motor will include the electrical resistance, and impedance of the motor coil. This voltage will drive the threaded shaft using a gyrator element. The rotating shaft has a rotational inertia, and has resistance in the bearings. This rotation is transformed into linear motion using a transformer. The CNC machine block in this case will be the base connection of the actuating truss, as well as the equivalent mass it will be required to push. There will also be resistance along the track of the linear motion. Figure 5-31 - Bond Graph Model of Lead Screw shows the developed bond graph model for the lead screw system used to drive the deployable oil dispersant system.

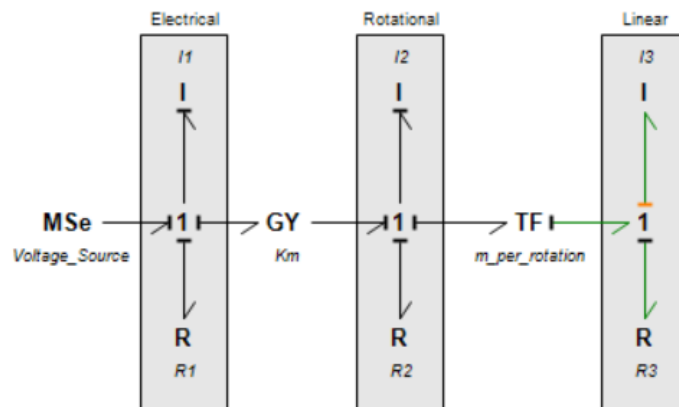


Figure 5-31 - Bond Graph Model of Lead Screw

With the model recreated in 20-Sim, the next step is to define the parameters of the system. The first parameters to consider are the DC motor values. The DC motor contains impedance coming from the motor coil, and an electrical resistance. The gyrator value is called the motor constant in this case. These values are all based on the motor that has been selected. A motor with the capability of pushing at least 252N was chosen, yielding the parameters presented in Table 5-3. The rotational inertia depends on the size of the shaft involved. It was decided that the shaft will likely be a similar size to the one used in the CNC machine example, and those values will be used in this case. Once the detailed analysis stage is reached, these values can be manipulated to update for the final design. Both the bearing and slider resistances were also used as per the CNC machine example. The inertia of the linear motion was difficult to determine, but an approximate value based on the weight of the overall system was used. Table 5-3 presents all of the values chosen for this lead screw bond graph model.

Table 5-3 - Bond Graph Parameters

Element	Description	Value
I1	Motor Impedance	0.0252
I2	Rotational Inertia of Shaft	0.00298
I3	Inertia of Track	15.0 kg
R1	Electrical Resistance	0.94 Ω
R2	Bearing Resistance	0.06
R3	Track Resistance	1.0
GY	Motor Constant	0.22248 τ^2/W
TF	Distance Travelled Per Rotation	0.02101 cm/rotation

5.4.2. 20-Sim Model

With the bond graph model of the lead screw system developed, it is now possible to integrate that system into the original model containing the 3D Mechanics model. The bond graph model has to input directly to a power port on the 3D model. The effort from the 1-junction of the linear motion portion of the bond graph is used as the primary input to the 3D model.

The bond graph leadscrew model equations generate a linear velocity as the output, and the 3D boom model requires a force input. This is described as a “causal conflict”, and can result in simulation errors and extreme run times. A “parasitic element” is used to mitigate this problem. The parasitic element is essentially a stiff spring element that is inserted between the leadscrew collar in the bond graph model and 3D boom submodel.

The leadscrew output motion deforms the stiff spring to a negligible amount, and the resulting spring force from the stiff spring is then used as the input force rather than the leadscrew collar velocity. This allows the generation of explicit ordinary differential equations which greatly reduce simulation time [58]. Figure 5-32 shows the parasitic element added in.

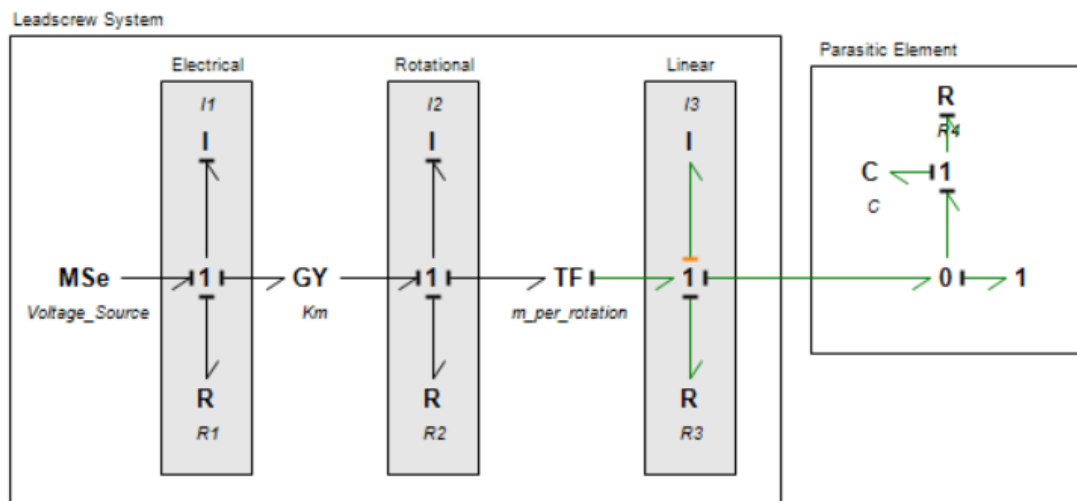


Figure 5-32 - Bond Graph Model with Parasitic Element

The control loop requires improvements before a final model is complete. Previously, a velocity sensor was used to determine the velocity created by the force input. However, in reality, determining the velocity of the system would be difficult due to sensor limitations. It is possible, but detecting the position of the linear actuator block would be simpler. It was decided that a position control loop would be most relevant to the design. A position sensor was attached to the 3D model, and used to calculate an error comparing to the target position, similar to the simplified model. The error is put through a

proportional integral controller, and finally a voltage limiter. Figure 5-33 shows the complete bond graph model integration into the deployable oil dispersant system dynamics model.

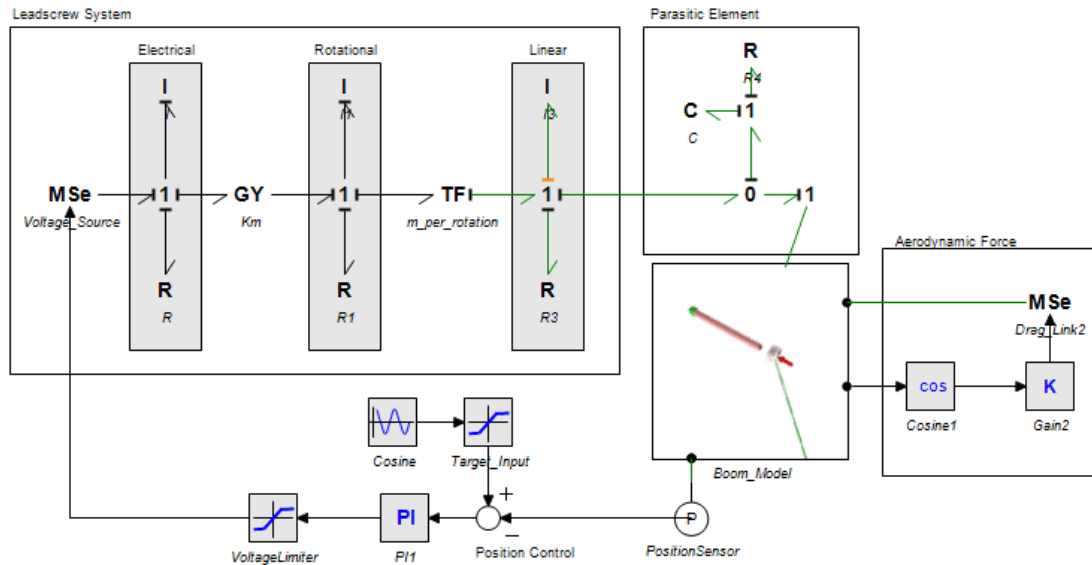


Figure 5-33 – Deployable Oil Dispersant Dynamics Model

5.4.3. System Analysis

This complete model can now be used to analyze the system response during operation. The bond graph model allows insight into many specific details within the lead screw system, and how it drives the operation of the deployable oil dispersant system. To begin, the output force is considered, and compared with the simplified model. The start-up force is greater in the advanced model, and can be attributed to the difference in the source input. Previously, only the 3D Model inertia was involved in the initial overshoot, but now the DC motor and shaft inertia are involved. The initial overshoot now reaches

approximately 268N as compared to the 248N overshoot seen in the simplified model.

Figure 5-34 shows this overshoot in the first 0.3 seconds of operation.

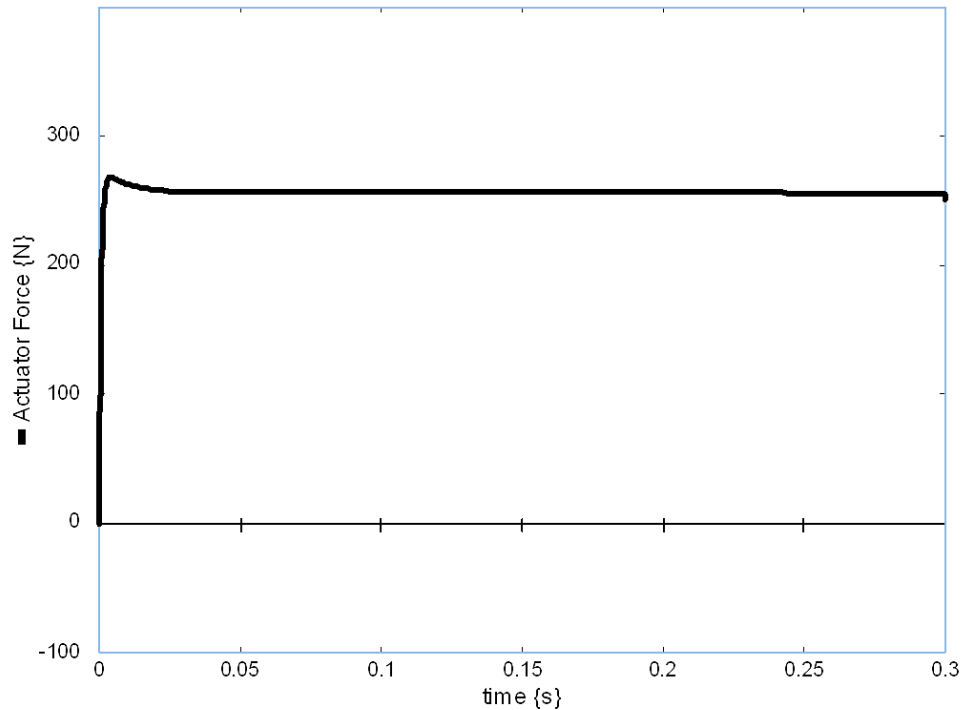


Figure 5-34 - Force Overshoot

Both motor start-up effects and inertia effects can be observed in this model. These values can be brought back to the preliminary design stage, and stresses can be recalculated.

Motor selection is often a difficult task in engineering, as many aspects must be considered. The power draw, physical size, and output force vary greatly, and it is often difficult to satisfy the preference of each discipline during this stage. There are many types of motors, and even if the ideal parameters were determined through calculations, it is unlikely that a motor of that exact specification will exist. This bond graph model

provides a unique advantage in this particular problem, as the bond graph values can be updated, and results can be obtained immediately. A series of motors can be trialed using this model in a short amount of time, providing accurate results. Two motors were compared to demonstrate the effects on a critical point in the system operation. Figure 5-35 shows the point when the oil dispersant system begins to retract, from the fully deployed position.

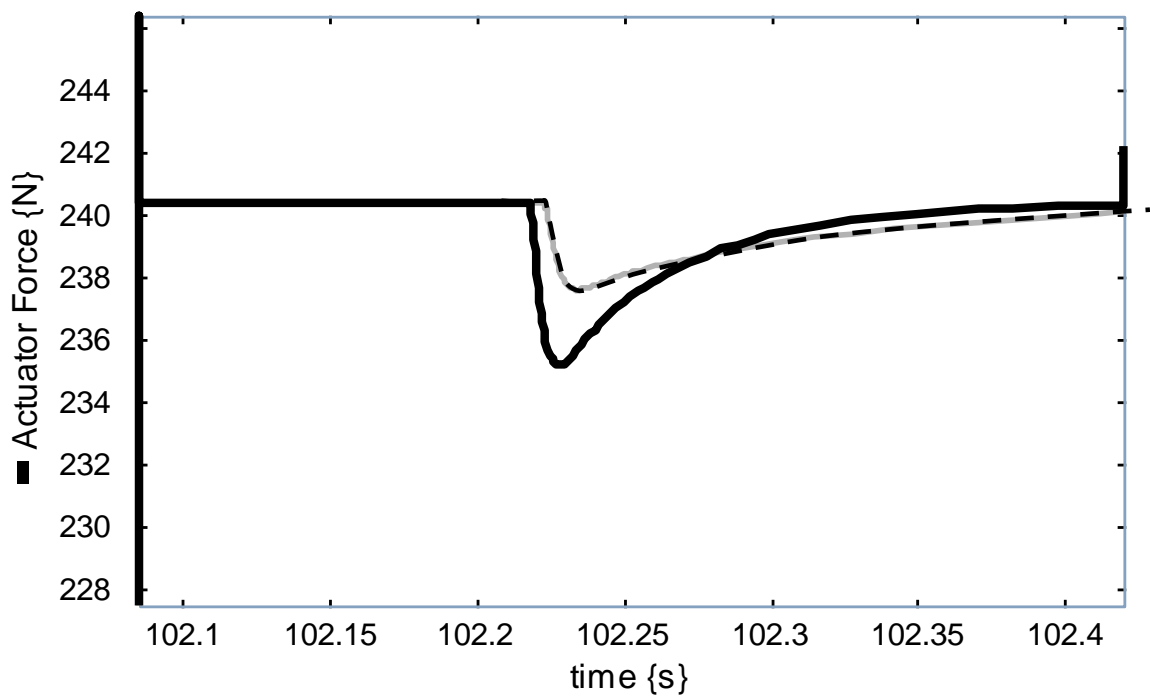


Figure 5-35 - Effects of Changing Motor Parameters

The operation of the system as it begins to stow sees a sudden drop in force as the motor begins to operate, and inertia is overcome. The motor input values were changed, and a clear difference between responses were observed. The solid line represents the motor described in the original advanced model, and the dotted line represents a physically

larger motor. The decrease in this spike shows a less rapid response of the system since it has to overcome a larger inertia.

The 20-Sim 3D Mechanics model can also output joint forces. These forces will be useful in the detailed design stage, as the maximum load on each joint can be determined. Figure 5-36 shows the forces in the main boom connection with the fuselage (joint 1), and the joint on the other end of the main boom, where it connects with the actuating truss (joint 2).

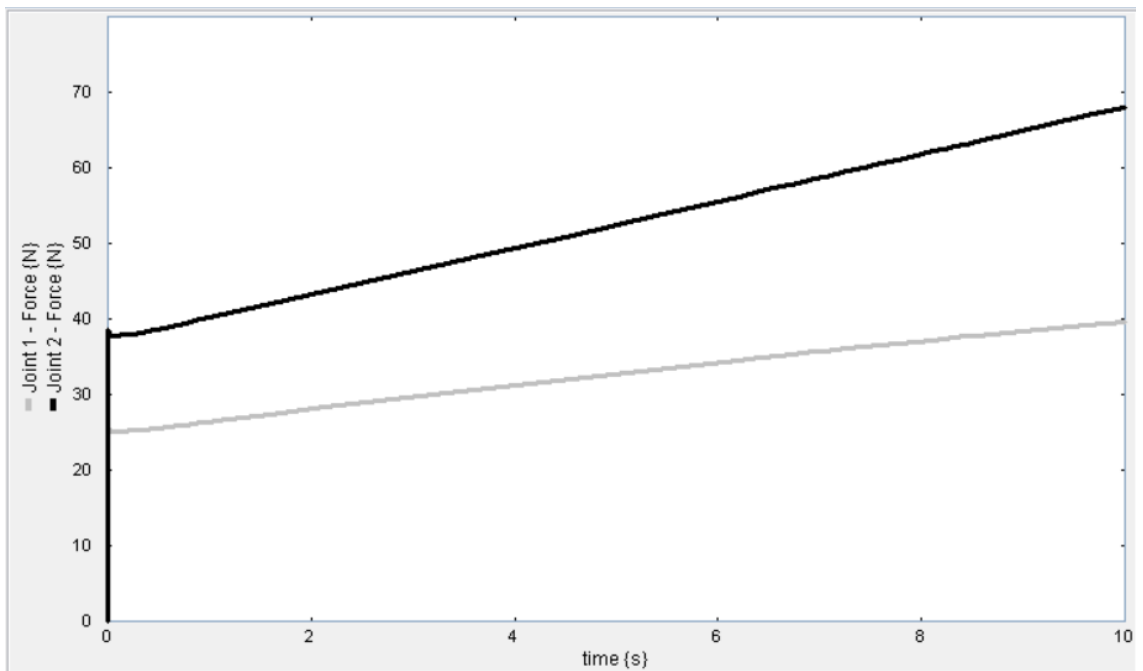


Figure 5-36 - Dynamic Joint Forces

The joint forces are seen to increase as the system begins to deploy. 20-Sim outputs forces in every plane for each joint. These joint forces can be found using standard static analysis techniques, but the dynamic analysis may reveal unexpected behaviour present

during the operation of the deployment mechanism. In this particular case, there was no evidence of any adverse effects from the motor start-up and inertia on the joint forces.

The avionics advantages of such a system are also significant. The bond graph allows for a realistic voltage input, as well as analysis of the system current and power draw. More complex circuitry can be included, but in this case, the model will only consider the DC motor. Figure 5-37 shows the voltage input to the system. The deployment of the system can be seen with a -120V output. Once the system reaches the fully deployed state, the voltage hovers close to zero. Finally, when the system begins to retract, the voltage rises to 120V.

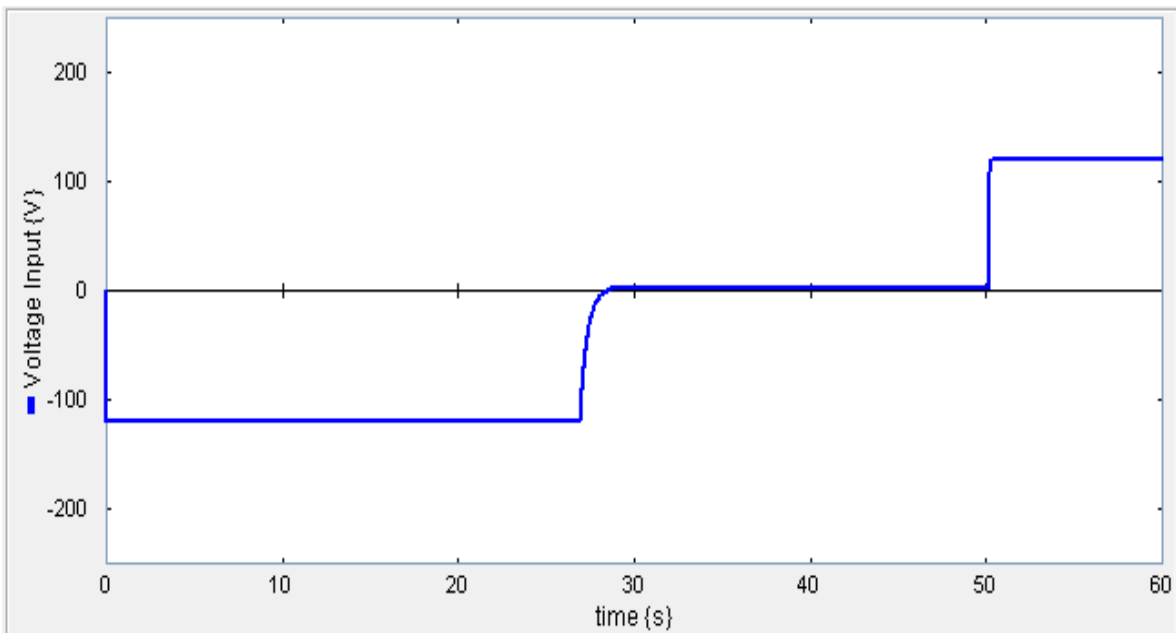


Figure 5-37 - System Voltage Input

The current necessary to apply the required force, and move at a certain velocity can be observed. Figure 5-38 shows this current draw at various stages of the deployment.

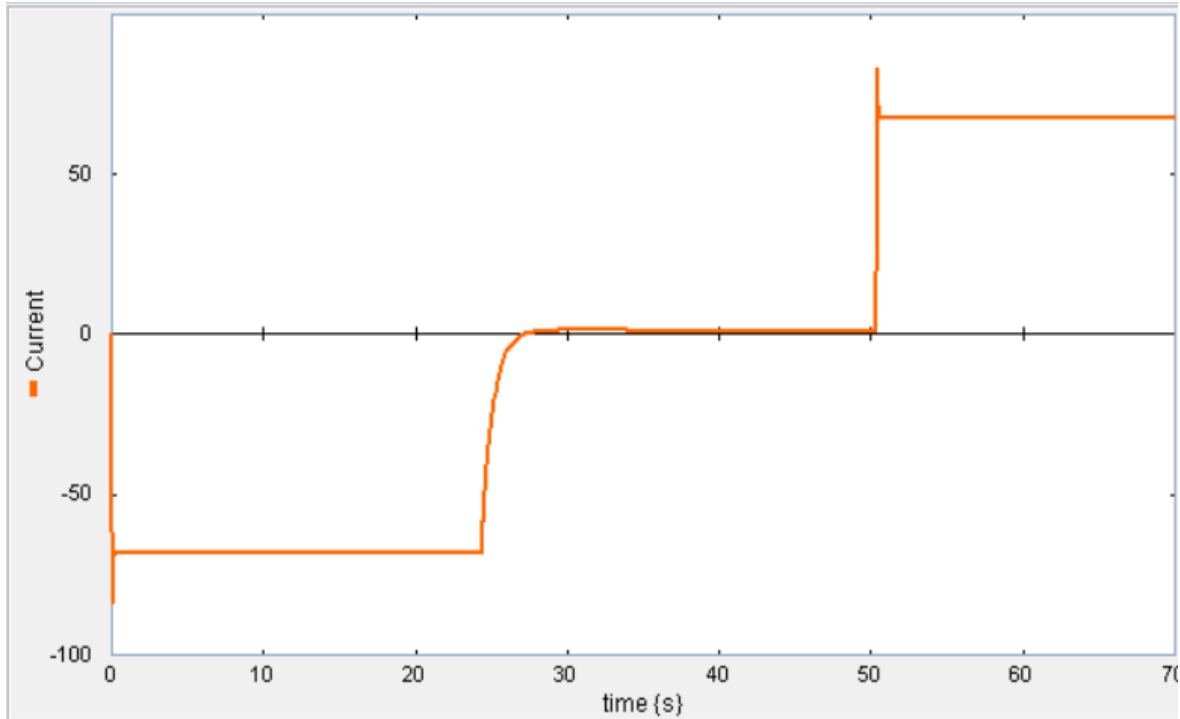


Figure 5-38 - System Current Draw

The current draw at the 30 second deployment speed is significant. Reaching a steady 68 amps, the system is drawing almost 8200W or 11 horsepower. The reason for the high value is the rapid deployment speed. Increasing the resistance in the motor reduces the deployment speed. This modification sees a marked reduction in the current, putting it at a more realistic value. The speed can also be reduced by changing the transformer value that represents the linear distance travelled per rotation of the shaft. Figure 5-39 shows

the improved system, drawing a more realistic 13 amps, with the results from Figure 5-38 shown as a dotted line.

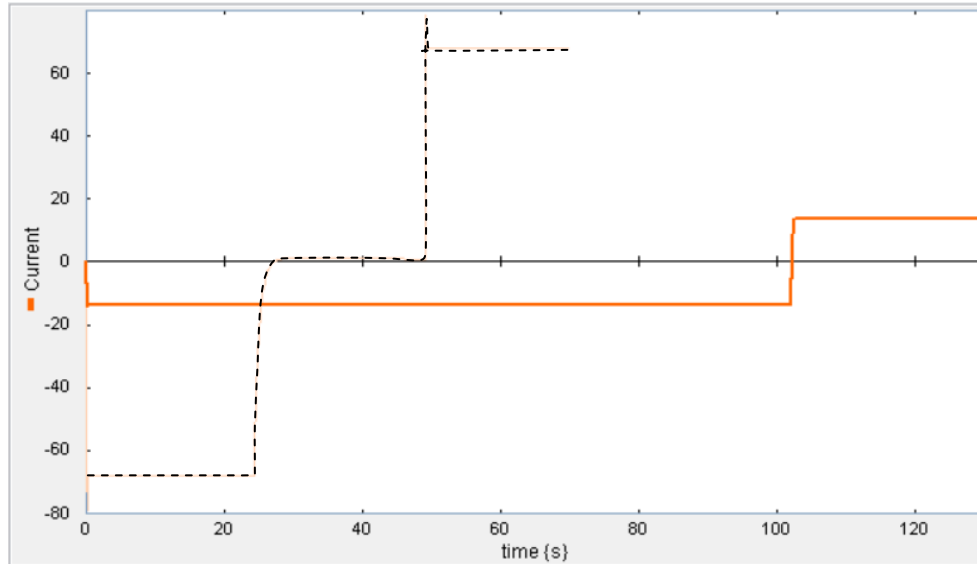


Figure 5-39 - Decreasing the Current Draw

The resulting deployment speed is 105 seconds, so there is a design trade off. If a faster deployment speed is desired, there will need to be a greater power capacity from the avionics side. If the power is simply not available for the system to operate at that speed, then the speed needs to be reduced, or other factors such as the motor selection and system design must be reconsidered.

This highlights the potential uses for a complex and realistic dynamics model. To further develop this model, it could be beneficial to improve the aerodynamics model used. The aerodynamics model is very basic and not detailed. Though the impact of this on the overall results is minor, it is still an area for improvement and refinement. Once the

detailed design stage begins, the avionics can be modelled in the bond graph model in greater detail. This may be beneficial in providing more accurate results on the current and voltage simulation. The oil dispersant reservoir, pump, and spray nozzles may also be modelled using this approach, and may be considered in future iterations.

Another potential use for this simulation model is using it in the real world control of the system. 20-Sim has data acquisition and control hardware available that can use analog input and output signals to control the actual lead screw system, and read position sensors. This provides a simplified control system that can easily integrate into the aircraft and workstation computing systems.

5.5. Conclusion

The model is relatively simple and quick to develop, and provides unique insight into multiple aspects of the system design. This tool can be used for co-operation between multiple disciplines during the design, manufacturing, and implementation of a complex dynamic system such as the deployable oil dispersant system. Further, it provides accurate results, and can quickly be updated for immediate results on design changes. This simulation model would ideally be used during the detailed design stage when the motor selection is occurring. It is also vital in understanding the critical loading scenario of the system which cannot be fully revealed with simple static analysis. Finally, the dynamics model provides unique insight into the load increases experienced during the operation of the system, resulting from motor start up effects and overcoming inertia, giving an accurate view of the critical system loading under dynamic effects.

6. Conclusions

The rapid development and growth of the offshore oil industry, and increasing oil tanker traffic around Newfoundland and across the globe demands a more efficient and rapid response to offshore oil spills. As discussed, one of the most effective ways to mitigate the impact of an oil spill is the use of oil dispersant chemicals. These chemicals can be applied using various methods, such as ships, helicopters, and fixed wing aircraft. The spraying of oil dispersants from fixed wing aircraft has been shown to be the most effective and rapid way of dealing with a surface oil slick resulting from an accident. Current systems designed for this application range from fixed external systems to deployable internal systems. This thesis investigated and designed a deployable oil dispersant system which can extend and retract during flight for greater aerodynamic, and therefore, range efficiency of the aircraft. A preliminary design is presented, which made use of several levels of complexity. This chapter summarizes the final results of this preliminary design, followed by a discussion of the design process itself, and what future work may be done in this area.

6.1. Preliminary Design Overview

The preliminary phase was initiated by inspecting existing designs and patents. These designs provided inspiration for aspects of the preliminary design. The components that define the preliminary design were placed into two categories, the primary structural components, and the secondary system components. This thesis focussed on defining the primary structural components using standard and advanced engineering techniques. A

parametric design method was developed to provide a standardized method of defining the critical system parameters relating to fluid delivery requirements, geometry limitations, and stress requirements. The initial sizing of the main boom was determined using limitations on the flow dispersal rate, and considered existing designs. Further, the limitations on the length and position of the system on the airframe dimensions provided general overall dimensions of the system. With the general dimensions determined, it was possible to determine the loading on the system as a function of the remaining parameters. Several materials were compared, and an initial preliminary design was produced using classical solid mechanics techniques and empirical data to describe aerodynamic loads. Figure 6-1 shows the initial preliminary design and its components.

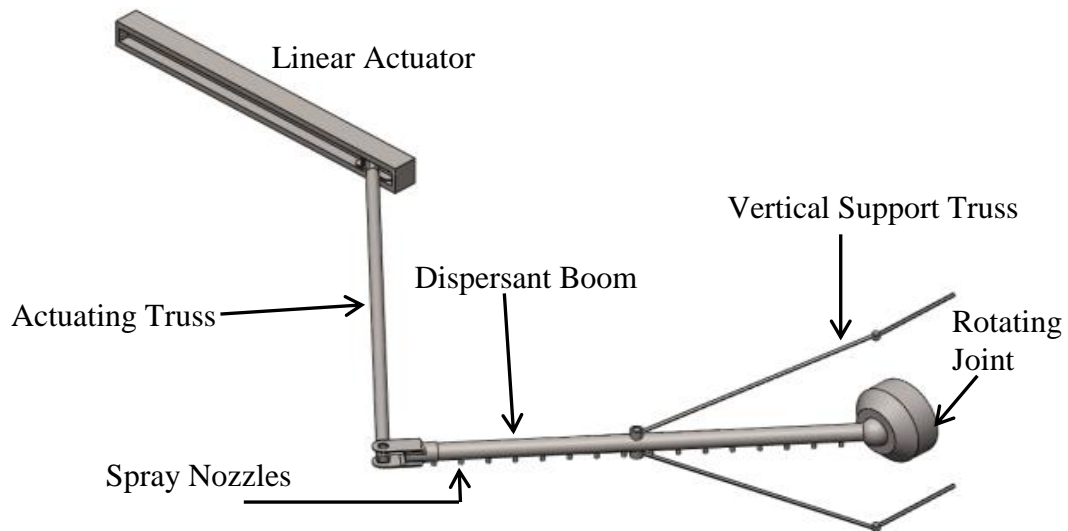


Figure 6-1 - Preliminary Design Summary

The preliminary dimensions were determined based on the dimensions of a Dash 8 Q300 aircraft. Identifying the design in terms of its parameters leads to an adaptable design

solution which can be applied to many different aircraft platforms. Table 6-1 outlines the parameter dimensions determined using the simplified analytical and empirical techniques.

Table 6-1 - Defined System Parameters

Parameters	Value
D_i – Inner diameter of boom	0.1016 m
L_1 – Boom length	2.1336 m
L_2 – Actuating truss length	2.4544 m
Θ - Angle of fully deployed boom	49.0°
Material	Aluminum 6061-T6
E – Elastic modulus	68.9 GPa
m_1 – Mass of boom	6.02 kg
m_2 – Mass of support	4.68 kg
t – Thickness of boom pipe	3.175 mm
L_c – Vertical support location	0.6 m
D_T – Diameter of the support truss	4 cm
D_a – Diameter of the actuating truss	3 cm

With the preliminary design determined using simplified techniques, the next step was to optimize the design, using various advanced engineering tools to solve more complex engineering problems.

6.2. Overview of Detailed Analysis

The detailed analysis carried on from the initial preliminary design. The preliminary design provided a basis for further design optimization, and prepared the way for the design of the secondary system components. Three types of advanced engineering analysis were implemented to further understand the complex loading and motion of the system. Numerical methods including Finite Element Analysis (FEA) and Computational Fluid Dynamics (CFD) were used to determine the static response and wind loads on the preliminary design. A dynamics model was used to understand the dynamic forces and actuator loads experienced during the operation of the deployable oil dispersant system.

The CFD analysis was compared with empirical aerodynamic data. Although there was some discrepancy, the results showed convergence to the empirical data. From these results, the pressure gradient could be determined, allowing for a more accurate representation of the wind loads using 3D FEA techniques.

The FEA began by modelling the exact conditions seen in the analytical model using a wireframe model, where there was good agreement between results. From this point, the wireframe model was developed to include all primary structural components. This allowed for a global view of the stresses and loads present in the system, including the vertical support trusses and actuating truss. To understand the effects of localized stress concentrations and buckling the model complexity was increased. To achieve this, the main boom was represented by a shell element. This model enabled the designers to

identify points of concentrated stress in specific areas, affecting the final design outcome, and optimizing the design definition.

Finally, a dynamics model was created to observe the behaviour of the system during the deployment and stowing operation. Using the dynamics simulation program 20-sim, and the bond graph technique, a complex dynamics model was generated for the simulation of the system. The model combines several disciplines of analysis into one combined model, considering electrical, mechanical, and aerodynamic effects governing the system design. This dynamic analysis led to several useful conclusions. The model can be used for equipment selection during the detailed analysis stage, as the model parameters can be updated with immediate results. Further, the model can output the forces experienced in the system due to inertial loads and motor start-up effects. Electrical data such as voltage and current can be observed, and can be used in the avionics engineering design aspect of the system. In this particular case, it was concluded that the spikes in loading due to inertia and motor effects do not affect the critical load experienced by the system, and therefore does not affect the preliminary design dimensions.

These three tools have provided a greater insight into the behaviour of the system exposed to complex loading and motion. As the design progresses in the future, these tools are well developed to assist in the detailed design and equipment selection stage.

6.3. Future Work

Future work will consider several aspects of the design. With the preliminary design complete, the next stage is to develop the secondary system components. The secondary system components are identified as the oil dispersant chemical reservoir, pump, spray nozzles, connecting hardware, rotating joints, and linear actuator. Many of these components can be designed or chosen once the aircraft platform is confirmed, and details about the airframe structure are known. Further research may be required before designing the internal fluid delivery system as well.

The FEA model can assist in the detailed design stage. Solid and shell elements can be used to model the connections between components, and the stress distribution on the fuselage of the aircraft itself. The CFD model can be further refined, including the vertical support trusses and actuating truss. The overall drag will be greater, which will be helpful for understanding the stress and fatigue life of the system and its attaching hardware. Further, any fairing to cover the stowed system will require extensive CFD simulation to optimize the shape and ensure it is properly designed. If a foil shaped fairing is used for the main boom, it must be simulated, along with the attaching spray nozzles to determine any aerodynamic lift loads present. It may also be beneficial to consider fatigue analysis of critical system components from cyclic aerodynamic loads.

The dynamics model has many areas that could be further developed. The aerodynamics model was kept very simple, and could be improved for better accuracy. More system components can be modelled in the system, increasing its accuracy. Further, the model

could be used to control an actual linear actuator through data acquisition and control hardware. This may provide a novel way of controlling the motion of the system, which can incorporate several sensor inputs and motor outputs.

Finally, it is important that aeroelastic analysis be considered for the final design. As the system is exposed to a high speed flow and its high inertia due to the internal fluid, it may be susceptible to failure due to dynamic instabilities such as flutter. Further research would be required, but it could be accomplished with a simplified solution to determine the critical speed at which flutter occurs. If flutter occurs below the operational speed, then cross-sectional optimization is required for torsional strength and other structural parameters. There exists developed aeroelastic models for 20-sim, which could potentially solve this problem, and can be integrated with the current model [59].

6.4. Concluding Remarks

In conclusion, the preliminary design presented in this thesis presents a novel detailed design method that incorporates the standard industry practice with advanced engineering analysis. The parametric design process and advanced analysis tools are effectively applied to any aircraft platform, as the preliminary design presented in this thesis moves into the detailed design stage. Further, this design presents a viable alternative to the industry standard, providing improved efficiency, and a new way of approaching the problem.

References

- [1] Government of the United States of America, *The Use of Surface and Subsea Dispersants During the BP Deepwater Horizon Oil Spill*. Washington, DC: National Commission on the BP Deepwater Horizon Oil Spill and Offshore Drilling, 2011.
- [2] Government of Newfoundland and Labrador, *Review of Offshore Oil-Spill Prevention and Remediation Requirements and Practices in Newfoundland And Labrador*. St.John's, NL: Department of Natural Resources, 2010.
- [3] Government of Canada, *Environmental Oil Spill Risk Assessment for the South Coast of Newfoundland*. Ottawa, ON: Transport Canada, 2007.
- [4] Earth Science Australia, "Oil Spills," *Earth Science Australia*, 2006. [Online]. Available: <http://www.earthsci.org/mineral/energy/gasexpl/spill.html>. [Accessed: Dec.7, 2014].
- [5] C. W. Schmidt, "Between the Devil and the Deep Blue Sea: Dispersants in the Gulf of Mexico," *Environ Health Perspect.*, vol. 118(8), pp. A338-A344, 2010.
- [6] A. Lewis and P. S. Daling, "Evaluation of Dispersant Spray Systems and Platforms for use on Spilled Oil in Seas with Ice Present (JIP project 4, act. 4.21)," SINTEF, Trondheim, Norway. 20 Feb. 2007.
- [7] "Dispersant Application Observer Job Aid," Courtesy of NOAA, 2007.
- [8] "FAA STC for Bell 212 Agricultural Spray System," *Helihub*, August 5, 2013. [Online], Available: <http://helihub.com/2013/08/05/faa-stc-for-bell-212-agricultural-spray-system/>. [Accessed: Nov. 20, 2014].
- [9] National Oceanic and Atmospheric Administration, *Special Monitoring of Applied Response Technologies*. Silver Spring, Maryland: Office of Response and Restoration, 2014. Available: <http://response.restoration.noaa.gov/SMART>. [Accessed: Nov. 20, 2014].
- [10] Oil Spill Response Joint Industry Project, *Current Status and Future Industry Needs for Aerial Dispersant Application*. IPIECA, and International Association of Oil & Gas Producers, 2012.
- [11] M. Price, S. Raghunathan and R. Curran, "An Integrated Systems Engineering Approach to Aircraft Design," *Progress in Aerospace Science*, vol. 42, iss. 4, Jun., pp. 331-376, 2006.

- [12] R. J. Odegaard, "Spray Boom," US 3933309, Jan. 14, 1975.
- [14] D. M. Ryle, "Aerial Dispersal System," US 4180224, Apr. 6, 1978.
- [15] J. C. Jefferies, "Spray Boom Apparatus for Applying Chemical Dispersants to Ocean Oil Spills," CA 1185581, Jan. 8, 1982.
- [16] B. R. Nolan, "Systems and Methods for Aerial Dispersion of Materials," US 7284727, Oct. 1, 2003.
- [17] C. R. Barlow, "Jettisonable Agricultural Sprayer," US 3936018, Aug. 8, 1974.
- [18] Marine Spill Response Corporation, "Dispersants," Available: <http://www.msrc.org/services/oil-spill-response/dispersants/>. [Accessed Sept. 19, 2014]
- [19] European Maritime Safety Agency, *Manual on the applicability of oil dispersants*, 2009.
- [20] Courtesy of Florida Air Transport. Available: <http://floridaairtransport.com/aircraft.php>. [Accessed Sept.22, 2014]
- [21] R. Wickens, "Reduction of Aerodynamic Drag of External Spray Booms and Nozzles used on DC-6 Aircraft," Canadian Aeronautics and Space Journal, vol. 26, quarter 1, May, pp. 46-51, 1980.
- [22] J. D. Anderson, *Fundamentals of Aerodynamics*. New York: McGraw Hill, 2001.
- [23] J. M. Gere and B. J. Goodno, *Mechanics of Materials*. Global Engineering, 2013.
- [24] R. Moore, A. Murphys, M. Price and J. Wang, "Analysis driven design and optimization methods for aircraft structures using finite element analysis," In Proc. AIAA/ASME/ASCE/AHS/ASC Structures, Structural Dynamics and Materials Conference, 2007.
- [25] L. Boni and D. Fanteria, "Development of Analytical Methods for Fuselage Design: Validation by Means of Finite Element Analyses," In Proc. of the Institution of Mechanical Engineers, Part G: Journal of Aerospace Engineering, 2004, vol. 218(5), pp. 315-327.
- [26] L. Boni and D. Fanteria, "Finite-Element-Based Assessment of Analytical Methods for the Design of Fuselage Frames," In Proc. of the Institution of Mechanical Engineers, Part G: Journal of Aerospace Engineering, 2006, vol. 220(5), pp. 387-398.

- [27] X. Guo and G. Cheng, "Recent Development in Structural Design and Optimization," *Acta Mechanica Sinica/Lixue Xuebao*, vol. 26(6), pp. 807-823, 2010.
- [28] B. Colson, M. Bruyneel, S. Grihon, C. Raick and A. Remouchamps, "Optimization Methods for Advanced Design of Aircraft Panels: A Comparison," *Optimization and Engineering*, vol. 11(4), pp. 583-596, 2010.
- [29] G. Park, "Technical Overview of the Equivalent Static Loads Method for Non-Linear Static Response Structural Optimization," *Structural and Multidisciplinary Optimization*, vol. 43(3), pp. 319-337, 2011.
- [30] R. M. Taylor, and T. A. Weisshaar, "Improved structural design using evolutionary finite element modeling," In Proc. RTO AVT Symposium on "Reduction of Military Vehicle Acquisition Time and Cost through Advanced Modelling and Virtual Simulation", 2003.
- [31] Z. J. Wang, K. Fidkowski, R. Abgrall, F. Bassi, D. Caraeni, A. Cary, H. Deconinck, R. Hartmann, K. Hillewaert, H. T. Huynh, N. Kroll, G. May, P. Persson, B. van Leer and M. Visbal, "High-order CFD methods: Current Status and Perspective," *International Journal for Numerical Methods in Fluids*, vol. 72(8), pp. 811-845, 2013.
- [32] J. S. Shang, "Computational Fluid Dynamics Application to Aerospace Science," *The Aeronautical Journal*, vol. 113(1148), pp. 619-632, 2009.
- [33] A. Nakayama, D. Okamoto and H. Takeda, "Large-Eddy Simulation of Flows Past Complex Truss Structures," *Journal of Wind Engineering and Industrial Aerodynamics*, vol. 98(3), pp. 133-144, 2010.
- [34] S. Keye, "Fluid-Structure Coupled Analysis of a Transport Aircraft and Flight-Test Validation," *Journal of Aircraft*, vol. 48(2), pp. 381-390, 2011.
- [35] C. R. Gumbert, G. J. Hou and P. A. Newman, "High-Fidelity Computational Optimization for 3-D Flexible Wings: Part I - Simultaneous Aero-Structural Design Optimization (SASDO)," *Optimization and Engineering*, vol. 6(1), pp. 117-138, 2005.
- [36] C. Wu, Y. Baik and S. Choi, "Integration of Configuration Design and Multidisciplinary Analysis of Aircraft," In Proc. World Aviation Conference, 2000.
- [37] J. Sobieszczanski-Sobieski and R. T. Haftka, "Multidisciplinary Aerospace Design Optimization: Survey of Recent Developments," *Structural Optimization*, vol. 14(1), pp. 1-23, 1997.

- [38] W. Yao, X. Chen, W. Luo, M. van Tooren and J. Guo, "Review of Uncertainty-Based Multidisciplinary Design Optimization Methods for Aerospace Vehicles," *Progress in Aerospace Sciences*, vol. 47(6), pp. 450-479, 2011.
- [39] S. Gomathinayagam, C. Vendhan and J. Shanmugasundaram, "Dynamic Effects of Wind Loads on Offshore Deck Structures - A Critical Evaluation of Provisions and Practices," *Journal of Wind Energy and Industrial Aerodynamics*, vol. 84(3), pp. 345-367, 2000.
- [40] DeHavilland Dash 8 Series 300 Structural Repair Manual, Chapter 53, 2011.
- [41] Courtesy of Air Force Reserve Command Aerial Spray Gallery. Available: <http://www.afrc.af.mil/photos/mediagallery.asp?galleryID=335>.
- [42] Alaska Department of Environment Conservation, *Spill tactics for alaska responders: Dispersant application*, 2006.
- [43] "ADDS Pack Application Rates," Industry Technical Advisory Committee, Tech. Report.
- [44] K. Avila, D. Moxey, A. De Lozar, M. Avila, D. Barkley and B. Hof, "The Onset of Turbulence in Pipe Flow," *Science Magazine*, vol. 333(6039), pp. 192-196, 2011.
- [45] *Canada Aviation Regulations*, Part V, Airworthiness Manual Chapter 525, Transport Category Airplanes, Subchapter C - Structures, section 335 - Design Air Speeds, 2001.
- [46] T. Nedwed, G. Canevari, R. Belore, J. Clark, T. Coolbaugh and A. Tidwell, "New Dispersant Gel Effective on Cold, Viscous Oils," In Proc. International Oil Spill Conference, 2011, pp.109.
- [47] R. C. Hibbeler, *Mechanics of Materials*. Prentice Hall, 2004.
- [48] G. Grimberg, W. Pauls and U. Frisch, "Genesis of D'alembert's Paradox and Analytical Elaboration of the Drag Problem," *Physica D*, vol. 237(14-17), pp. 1878-1886, 2008.
- [49] R. L. Panton, *Incompressible Flow*, 3rd Ed., Hoboken, NJ: John Wiley & Sons Ltd, 2005.
- [50] R. S. Shevell, *Fundamentals of Flight*, Pp.373-386. Prentice Hall, 1989.
- [51] Alcoa Metals. Available: www.alcoa.com. [Accessed Oct.28, 2014].

- [52] Aerospace Specification Metals Inc. Available: www.aerospacemetals.com. [Accessed Oct.28, 2014].
- [53] 20-Sim, *Reference Manual 20-Sim 4.3*, Control Lab Products B.V., 2013.
- [54] D. Karnopp, D. Margolis and R. Rosenberg, *System Dynamics: Modeling, Simulation, and Control of Mechatronic Systems*, Chichester, UK: John Wiley & Sons Ltd, 2012.
- [55] Commonly Tested Mechanical Devices. Available: http://00.edu-cdn.com/files/static/learningexpressllc/9781576856710/COMMONLY_TESTED_MECHANICAL_DEVICES_03.GIF. [Accessed July 15, 2014].
- [56] J. F. Broenink, "Introduction to Physical System Modeling Using Bond Graphs," University of Twente, 1999.
- [57] (6 May, 2008). "Leadscrew Actuator delivers accurate, repeatable results," *Thomasnet Industry News*, May 6, 2008. [Online], Available: <http://news.thomasnet.com/fullstory/leadscrew-actuator-delivers-accurate-repeatable-results-543941>. [Accessed July 17, 2014].
- [58] P. Tomar and S. Das, "Bond Graph Modeling and Simulation of a Closed-Loop Feed Drive System for a CNC Machine," *SAE Technical Papers*, paper 1637, 2007.
- [59] W. Borutzky, *Bond Graph Modelling of Engineering Systems: Theory, Applications and Software Support*, New York, NY: Springer Science & Business Media, 2011, Pp.98.
- [60] C. P. Pagwiwoko, "Limit Cycle Oscillation Analysis on the Design of Wind Power Harvester with Fluttering Aerofoil," In Proc. International Conference on Renewable Energies and Power Quality, 2013.

Appendix

Dynamic Analysis of a Deployable Oil Dispersant System for Fixed Wing Aircraft, presented at the International Aerospace Engineering Conference 2014, in Dubai, UAE.

Deployable Oil Dispersant System for Fixed Wing Aircraft, presented at the IEEE/MTS Oceans '14 Conference, in St.John's, Newfoundland.